

UPC - UNIVERSITAT POLITÈCNICA DE
CATALUNYA

DOCTORAL THESIS

Quantum Memory Protocols for Photonic Solid-State Devices

Author:

Kutlu KUTLUER

Supervisor:

Prof. Dr. Hugues DE
RIEDMATTEN

*A thesis submitted in fulfilment of the requirements
for the degree of Doctor of Philosophy*

in the

QPSA - Quantum Photonics with Solids and Atoms *group*,
ICFO - The Institute of Photonic Sciences

September 2017



UNIVERSITAT POLITÈCNICA
DE CATALUNYA
BARCELONATECH

ICFO^R
Institut
de Ciències
Fotòniques

To the pale blue dot...

“No matter what you look at, if you look at it closely enough, you are involved in the entire universe.”

Michael Faraday

Abstract

A photonic quantum memory (QM) is a device that has the capability of storing a quantum state of light and retrieving back after a controlled time. It is an important element in quantum information science and is, among other applications, a crucial device for quantum repeater architectures which have been proposed to overcome the loss and the decoherence issues in long distance transmission of photons. Rare earth ion doped solid state systems are promising candidates for QMs which combine the advantages of solid state systems, such as scalability and reduced experimental complexity, with the long coherence time typically found in atomic systems. In this thesis, I investigated three different QM protocols in a $\text{Pr}^{3+}:\text{Y}_2\text{SiO}_5$ crystal.

The first part describes here the first demonstration of the spectral hole memory (SHoMe) protocol which was proposed theoretically in 2009. This protocol relies on slowing down the light in a long-lived spectral hole and transferring the excitations to the spin state. We first prepare a spectral hole, then send an input pulse whose bandwidth is comparable with the hole and stop the compressed light in the crystal by transferring the off-resonant coherence to the spin state with an optical π pulse. Later a second π pulse transfers the coherence back and leads to the emission of the stored light. We reached a storage and retrieval efficiency of around 40% in the classical regime, and of 31% in the single photon level, with a signal-to-noise ratio of 33 ± 4 for a mean input photon number of 1. These results demonstrate the most efficient and noiseless spin-wave solid-state optical memory at the single photon level to date.

The second part of the thesis describes new experiments using the well-known atomic frequency comb (AFC) protocol. It is based on tailoring the inhomogeneously broadened absorption profile of the crystal with periodic absorptive peaks, which induce the re-emission of the absorbed light field after a certain time determined by the separation between the peaks. In

this chapter I describe several AFC experiments. First I present the storage of frequency converted telecom photons into our crystal where we obtained a total efficiency of 1.9 ± 0.2 % for a storage time of $1.6 \mu\text{s}$ and signal-to-noise ratio of more than 200 for a mean input photon number of 1. Then I discuss the results of improved excited state storage efficiency values for long storage times where we achieved 30% at short storage times and up to 17% at $10 \mu\text{s}$ storage time. And finally I present a spin-wave AFC experiment where we obtained a signal-to-noise ratio value of 28 ± 8 for a mean input photon number of 1, the highest value achieved so far for this kind of experiment.

Finally, in the last part, I describe the first demonstration of a solid-state photon pair source with embedded multimode quantum memory. The aim of the protocol is to combine a single photon source and a QM in one ensemble as in the well-known Duan-Lukin-Zoller-Cirac (DLCZ) scheme however this time not in a cold atomic ensemble but in a solid-state crystal. The protocol takes advantage of the AFC protocol for rephasing the ions and obtaining efficient read-out. The use of AFC also makes the protocol temporally multi-mode. In the experiment, after the AFC preparation we send an on-resonant write pulse and detect the decayed Stokes photons which herald single spin excitations. At a later time a read pulse transfers the spin excitation back to the excited state and we detect the anti-Stokes photons. We show strong non-classical second order cross-correlations between the Stokes and anti-Stokes photons and demonstrate storage of 11 temporal modes.

The results presented in this thesis represent a significant contribution to the field of solid-state quantum memories and an important steps towards the realization of scalable quantum network architectures with solid state systems.

Resum

Una memòria quàntica (MQ) és un dispositiu que té la capacitat d'emmagatzemar l'estat quàntic de la llum i retornar-lo després d'un temps controlat. És un element important en la ciència de la informació quàntica i és un dispositiu crucial per a arquitectures de repetidors quàntics, els quals han estat proposats per tal de solucionar els problemes de decoherència i pèrdues en la transmissió de fotons de llarga distància. Els sistemes d'estat sòlid basats en ions de terres rares són candidats prometedors per implementar MQs, ja que combinen els avantatges dels sistemes sòlids (escalabilitat i poca complexitat experimental) amb els llargs temps de coherència dels sistemes atòmics. En aquesta tesi he investigat tres protocols diferents de MQ en un cristall de $\text{Pr}^{3+}:\text{Y}_2\text{SiO}_5$.

La primera part descriu la primera demostració del protocol de memòria basat en forats espectrals (MFE), que va ser proposat teòricament el 2009. Aquest protocol es basa en disminuir la velocitat de la llum en un forat espectral de vida llarga i transferir les excitacions a un estat d'espín. Comencem preparant un forat espectral, després enviem un pols de llum amb una amplada espectral comparable a la del forat i aturem la llum comprimida en el cristall transferint la coherència fora de ressonància a l'estat d'espín amb un pols òptic. Seguidament un segon pols retorna la coherència i porta a l'emissió de la llum emmagatzemada. Aconseguint una eficiència d'emmagatzematge i recuperació de 40% en el règim clàssic i de 31% al nivell de fotons individuals, amb una relació senyal-soroll de 33 ± 4 per un nombre mitjà de fotons incidents igual a 1. Aquests resultats demostren la memòria òptica operant al nivell de fotons individuals amb més eficiència i més lliure de soroll.

La segona part de la tesi descriu nous experiments que utilitzen el protocol de pintes de freqüència atòmiques (PFA). Aquest està basat en modificar el perfil d'absorció eixamplat inhomogèniament dels ions de terres rares, creant pics d'absorció periòdics que indueixen la reemissió del camp de

llum absorbit, després d'un cert temps que ve determinat per la separació dels pics. En aquest capítol descriu varis experiments de PFA. Primer presento l'emmagatzematge en el nostre cristall de fotons amb freqüència convertida des de telecom, obtenint una eficiència total de $1.9 \pm 0.2\%$ per un temps d'emmagatzematge de $1.6 \mu\text{s}$ i una relació senyal-soroll de més de 200 per un nombre mitjà de fotons incidents igual a 1. Seguidament discuteixo els resultats obtinguts amb una millorada eficiència d'emmagatzematge en l'estat excitat per temps d'emmagatzematge llargs, on vam obtenir 30% per temps curts i 17% a $10 \mu\text{s}$. I finalment presento un experiment de PFA amb ona d'espín on vam obtenir una relació senyal-soroll de 28 ± 8 per un nombre mitjà de fotons incidents igual a 1, el valor més alt assolit mai en un experiment d'aquest tipus.

Finalment, en la última part, descriu la primera demostració d'una font de parelles de fotons d'estat sòlid integrada amb una memòria quàntica multimodal. L'objectiu del protocol és combinar en un sol sistema una font de fotons individuals i una MQ, com té lloc en el conegut esquema de Duan-Lukin-Cirac-Zoller (DLCZ), però en aquest cas amb un cristall en lloc d'un sistema d'àtoms freds. El protocol agafa els avantatges del protocol PFA per refasar els ions i obtenir una recuperació eficient. Utilitzant PFA fa que el protocol sigui temporalment multimodal. En l'experiment, després de la preparació de la PFA, enviem un pols d'escriptura en ressonància i detectem un fotó Stokes que anuncia excitacions d'espín individuals. Un temps més tard, un pols de lectura transfereix l'excitació d'espín de tornada cap a l'estat excitat i detectem fotons anti-Stokes. Mostrem fortes correlacions de segon ordre no-clàssiques entre els fotons de Stokes i anti-Stokes i demostrem l'emmagatzematge de 11 modes temporals.

Els resultats presentats en aquesta tesi representen una contribució significativa en el camp de les memòries quàntiques d'estat sòlid i un pas important cap a la realització d'arquitectures de xarxes quàntiques amb sistemes d'estat sòlid.

Acknowledgements

First of all, I would like to express my gratitude to Hugues de Riedmatten, my advisor, for his continuous support, positive attitude and guidance over the period of my PhD study and for his patience especially during my first year. I think we are a lucky group of people who can pass a stressful period of life by suffering the least of it. Also it might be a bit risky to offer me the position in the first place since I had no background in optics and quantum information but I guess it all worked out well in the end.

I would like to thank Margherita for being there whenever I need a guidance on any matter, especially on rare-earth ions. I thank you also for trying to keep the gender balance in the group, and also to keep putting my missing "the"s. I hope I am still your favourite PhD student.

I also thank Patrick from whom I learned a great deal on experimental quantum optics. Thanks for all your *hola k ases* (unfortunately this tradition in the group will fade away after me), for your bestest English, and for watching football (and/or soccer) in the lab. But I don't like the numbers 8 and 0.

I didn't have the opportunity to work with Matteo side-by-side but still I learned a lot from him. Thanks for all *the messages*, the stories and lunch time discussions.

In my first 3 years in Barcelona, Mustafa was my wingman (the worst one ever). I assume that I have never annoyed you with my stupid, basic questions even though you slapped me once xd I was lucky to overlap with you here in QPSA.

I am glad that I have the opportunity to work under the same roof, the QPSA, with former/present/future members of the group. I thank Nicolas, my Parisian boy, for being my lab-mate and for the fancy times inside/outside of the lab. It was a such *plaisir*. I thank Daniel, my office-mate for 4 years. I thank Boris for being Boris all the time. I thank Emanuele for

his help in the lab during the last months. I thank Alessandro for his muy fancy personality. You are really one of a kind with the most ingenuous heart. Keep it that way. I thank Pau for showing how Catalans play football, for his questions to keep us awake in the group meetings and also for translating the abstract of this thesis. I thank Georg for his interests in Turkish food and also for his immmms. And David, Andreas, Auxi, Dario, Chetan, Marco, Bernardo, Julia, Xavi, Marcel.li, Joachim, Chiara thank you guys for making QPSA a warm place!

I would like to thank people in human resources for making non-EU peoples life in ICFO much more easier. I also would like to thank mechanical workshop, electronic workshop, travel, purchasing and front-desk teams. I also thank ICONS people for providing me the opportunity to give photography talks.

I have met many other very nice people during my time in Barcelona. I would like to thank the Turkish community (especially the inner circle: Alican, İnci, Civan, Ceren, Deniz, Gizem, Gülçin, Oğuz, Başak, Pelin, Irmak, Baybars, Büşra, Onur, Zafer, Emre, and not Özlem). I also would like to thank all the models and photographers that I collaborated or exchanged ideas.

Finally, I thank my family for being always there and supportive all these years. Thank you.

List of publications

1. Kutlu Kutluer, María Florencia Pascual-Winter, Julian Dajczgewand, Patrick M. Ledingham, Margherita Mazzera, Thierry Chanelière and Hugues de Riedmatten, *Spectral-hole memory for light at the single-photon level*, Phys. Rev. A **93**, 040302(R) (2016) (Chapter 5).
2. Nicolas Maring, Kutlu Kutluer, Joachim Cohen, Matteo Cristiani, Margherita Mazzera, Patrick M Ledingham and Hugues de Riedmatten, *Storage of up-converted telecom photons in a doped crystal*, New J. Phys. **16**, 113021 (2014) (Chapter 6).
3. Kutlu Kutluer, Margherita Mazzera, and Hugues de Riedmatten, *Solid-State Source of Nonclassical Photon Pairs with Embedded Multimode Quantum Memory*, Phys. Rev. Lett. **118**, 210502 (2017) (Chapter 7).

Publications not included in this thesis:

4. Nicolas Maring, Pau Farrera, Kutlu Kutluer, Georg Heinze, Margherita Mazzera and Hugues de Riedmatten, *Photonic quantum state transfer between a cold atomic gas and a crystal*, accepted to Nature.
5. Mustafa Gündoğan, Patrick M. Ledingham, Kutlu Kutluer, Margherita Mazzera and Hugues de Riedmatten, *Solid State Spin-Wave Quantum Memory for Time-Bin Qubits*, Phys. Rev. Lett. **114**, 230501 (2015).
6. Daniel Rieländer, Kutlu Kutluer, Patrick M. Ledingham, Mustafa Gündoğan, Julia Fekete, Margherita Mazzera and Hugues de Riedmatten, *Quantum Storage of Heralded Single Photons in a Praseodymium-Doped Crystal*, Phys. Rev. Lett. **112**, 040504 (2014).
7. Kutlu Kutluer, Emanuele Distante, Margherita Mazzera and Hugues de Riedmatten, *Energy-time entanglement between a photon and a solid state spin excitation*, In preparation.

Table of Contents

Abstract	vii
Resum	ix
Acknowledgements	xi
List of publications	xiv
Contents	xv
1 Introduction	1
1.1 Quantum information	3
1.1.1 Qubits	3
1.1.2 Entanglement	5
1.2 Quantum communication	6
1.3 Quantum repeaters	9
1.4 Quantum memories	12
1.5 Scope of this thesis	15
1.6 State of the art in the lab	16
2 The rare-earth ion doped system Pr:YSO	19
2.1 Properties of Pr:YSO	20
2.2 Energy levels	22
2.3 Homogeneous and inhomogeneous broadening	25
2.4 Spectral hole burning	27
2.4.1 Class cleaning and memory preparation with holes and antiholes	29

3	Coherent light-matter interaction	33
3.1	Evolution of a resonant two-level system	33
3.2	Two-pulse photon echo	37
4	Experimental setup	41
4.1	606 nm lasers	41
4.1.1	606 nm laser via SFG	42
4.1.2	606nm light via SHG laser	45
4.1.3	Frequency locking	46
4.2	Cryostat	49
4.3	Detectors and other electronics	51
4.3.1	Classical detectors	51
4.3.2	Single photon counters	52
4.3.3	Pulse creation for memory preparation	53
5	Spectral Hole Memory	55
5.1	Introduction	55
5.2	Theoretical background	57
5.3	Experiment	59
5.3.1	Characterization with classical light	59
5.3.2	Performance at the single photon level	65
5.4	Discussion	67
6	Atomic Frequency Comb	69
6.1	Introduction	69
6.2	Theoretical background	73
6.3	Storage of up-converted telecom photons	76
6.3.1	Motivation	76
6.3.2	Experimental Setup	77
6.3.3	Results	80
6.4	Improved performances for excited state storage	83
6.5	Spin-wave AFC storage	84
6.6	Discussion and conclusion	86
7	A solid-state multi-mode emissive quantum memory with DLCZ-AFC	89
7.1	Introduction	90
7.2	Theoretical background	91
7.3	Experiment	95
7.3.1	Characterization of Stokes and Anti-Stokes photons	96

7.3.2	Non-classical correlations	98
7.3.3	Read-out efficiency	102
7.3.4	Controllable delay between the pairs and multi-modality	103
7.4	Towards entanglement between a photon and a spin-wave .	105
7.5	Discussion	109
8	Conclusions and outlook	111
8.1	Summary of the thesis	111
8.2	Outlook	114
8.2.1	Performance improvements	114
8.2.2	Future directions	115
A	9 classes of ions in Pr:YSO	117
	Bibliography	119

Chapter 1

Introduction

Communication is a basic need of all the livings. It is even crucial for survival. We communicate to share information, thoughts, feelings, and ideas as the word *commūnicāre* means “to share” in Latin. This might be the very reason why the word communication shares the same root with the word community. Without communication societies would not exist, so would the modern era [1].

A society would be open to threats if people belonging to it did communicate only with each other but not with the outside world. The more information a society can gather, the longer it can survive. Hence, long distance communication plays an important role in human history. Symbols are the key elements of long distance communication, they are what we share as I do in this very moment. When the first language/speech appeared is a contentious topic but we know that the first symbols started to be developed around 30.000 years ago [2]. Even though there were the times when smoke, drums, horns, and even reflection of the sun from metal mirrors were used to alarm people, since these kinds of techniques do not have large vocabulary, their use stayed very limited. The ability to write on a papyrus on the other hand was a vital step forward in that sense. It appeared in ancient Egypt around 2500BC [3]. From the BC era only

postal system and newspaper are still in use. With the invention of paper in 100AD [4], pigeon post started to be another alternative for long distance communication. Then the next breakthrough came with the invention of electric telegram and the Morse code in the first half of 19th century. The communication speed was then only limited with the response of electrons to an applied voltage. It was followed by the invention of telephone, still one of the most used long distance communication devices today. Using electromagnetic (EM) waves in free space for transmission started another branch of communication. The radio is the first device of this kind invented in the late 19th century. Around 50 years after the first radio broadcast, we were able to launch geosynchronous communication satellites to the Earth's orbit, the first step through GSM operators. Transmitting data over fiber optic cables completes the historical advance until today with the birth of ARPANET, the ancestor of the Internet, and the development of first personal computer (PC). Today in 2017, around 40% of the world population (3 billion) have Internet access [5], and the total number of cell phone subscriptions is around 7 billion [6]. Therefore long distance communication itself is not an issue any more, it is the security of the information flow more likely to be a problem. ¹

The long distance communication methods widely available today are based on classical bits. Data strings are encoded in the bits as either a 0 or 1. This is a simple two-state, binary approach. Any symbol can be encoded in the strings of bits. As it is mentioned above, long distance communication can be realized via electrical (telegraph, telephone etc.) or EM (radio, microwave transmission, fiber optics, satellites etc.) systems. The world wide web mostly depends on fiber optic network due to its low cost and reliability. Even though the data signal attenuates in the fibre optic

¹On the other hand, as a note to history, 10% of the population does not have any access on clean water [7] and one out of nine people on earth do not have enough food to lead a healthy active life [8]. Even though free market economy with the support of capitalism and imperialism accelerates technological advances, it is also the very reason of income inequality and ignorance to it all over the world maintained by the corporate media [9, 10]. However this issue is not in the scope of this thesis.

cable, the issue can be solved by employing fiber amplifiers every few hundred kilometres. One problem is the eavesdroppers who can monitor the information flow without being noticed. Data encryption methods (i.e. triple DES, RSA, blowfish, twofish, AES) offer some degree of security but cannot guarantee that your information is perfectly safe. With the help of quantum mechanical properties of particles, transferring quantum information (QI) offers much higher degree of security.

1.1 Quantum information

Quantum physics is a fascinating world with its counter-intuitive nature and ability to describe the world in sub-atomic regime. It is an immensely successful theory which has solved many mysteries. However we were not able to implement quantum phenomena such as superposition and entanglement in our technological advances until recent times. With new proposals and ideas, there are now possibilities for boosting the computational power [11], solving much complex simulations [12] and having much more secure communication networks [13]. They all depend on operations based on QI. Therefore this section will be on the basic concepts of quantum information science (QIS).

1.1.1 Qubits

Classical bits can take only two values, 0 or 1. However in quantum mechanics the state of a quantum system is described as the superposition of orthogonal states instead of binary states. Therefore the wave function of a quantum bit, or *qubit* [14], is a quantum superposition of 0s and 1s. A qubit can be represented in Dirac notation as,

$$|\psi\rangle = \alpha|0\rangle + \beta|1\rangle, \tag{1.1}$$

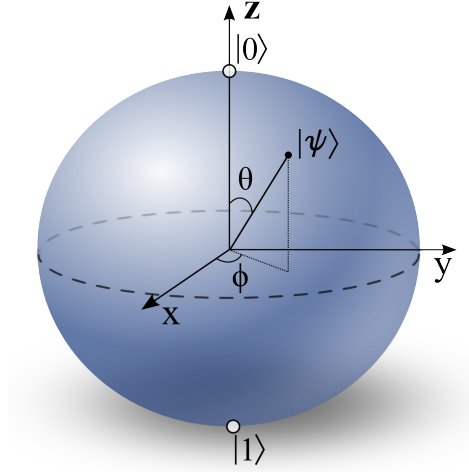


FIGURE 1.1: Bloch sphere representation of a quantum system.

where, α and β are the complex probability amplitudes with $|\alpha|^2 + |\beta|^2 = 1$. Here, $|0\rangle$ and $|1\rangle$ are the two orthogonal basis states.

We can visualize a qubit by using the *Bloch sphere* concept, as in Figure 1.1. A qubit on Bloch sphere can be described as,

$$|\psi\rangle = \cos\left(\frac{\theta}{2}\right) |0\rangle + e^{i\phi} \sin\left(\frac{\theta}{2}\right) |1\rangle, \quad (1.2)$$

where θ and ϕ are azimuthal and longitudinal angles. While a qubit can be represented by any point on the surface of the sphere, a classical bit can only be represented by the north or the south poles of the sphere. When a measurement is made on the qubit, the wavefunction collapses into one of the bases. Hence, the possible outcomes of an experiment could be still only 0 or 1 with the probability of $|\alpha|^2$ or $|\beta|^2$, respectively.

Qubits in general can be categorized into two types: stationary qubits and flying qubits. Stationary qubits are matter qubits, capable of storing and processing the quantum information that they receive or create. Nuclear spin, electronic spin, and electronic charge can be used as qubits. Many approaches have been successfully demonstrated as stationary qubits, such as cold and hot atomic gases, nitrogen-vacancy (NV) centers, rare earth

ion doped solids, Josephson junctions, quantum dots, and trapped ions. Flying qubits on the other hand can travel long distances, as the name suggests, and are used to transfer quantum information from one place to another. Quantum information can be coded into the polarization, time of arrival (time-bin), frequency, path, and/or orbital angular momentum of photons.

1.1.2 Entanglement

Entanglement is probably the most counter-intuitive concept in quantum physics. When a quantum state of two or more particles is inseparable, which means that the states of the particles cannot be described individually but only as a whole, then it is called an entangled state. For example, given two non-interacting Hilbert spaces, A and B, with two basis states $|0\rangle$ and $|1\rangle$, an entangled state can be written as

$$|\Psi_{1,2}^{\pm}\rangle = \frac{1}{\sqrt{2}} (|0_A, 1_B\rangle \pm |1_A, 0_B\rangle), \quad (1.3)$$

As an inevitable fact, when the quantum state of one particle is measured, the state of the other one also collapses instantaneously, in principle no matter how far apart the two systems are. At first sight this result seems to contradict Einstein's special theory of relativity which states that the speed of light is constant and that no message can be delivered faster than light [15]. However since there is no information transfer, there is no violation. But still it is incompatible with the principles of local realism. In 1935 Einstein, Podolsky, and Rosen first draw the attention to this phenomenon in their famous EPR paper [16]. They came to the conclusion that quantum physics is not complete. Shortly after the EPR paper, Schrödinger introduced the term *entanglement* and his famous *Schrödinger's cat* thought experiment [17]. Einstein later called this phenomenon *spooky action at a distance*. Both Einstein and Schrödinger were not satisfied with the indeterministic nature of the entanglement. In 1952 Bohm suggested the

hidden variables concept as a possible resolution of the paradox [18]. It was argued that wavefunctions are governed by hidden variables and any possible outcomes of a measurement are determined beforehand when the particles interact. However in 1964, John Bell showed that certain entangled systems can violate the upper limit of classical correlations which obey local realism [19]. He proposed an inequality, now named after him as *Bell's inequality*, that can be experimentally tested. And it was first Freedman and Clauser who demonstrated experimentally that the inequality can be indeed violated [20]. In 1982, Aspect's experiment showed even stronger violation of Bell's inequality [21]. In 2015, Hanson's group in Delft performed the first loophole free Bell test experiment [22] and shortly after it was followed by other loophole free Bell tests with better statistical violations [23–25].

Although entanglement is a counter-intuitive concept, it can be a useful tool in quantum communication, specifically necessary in the schemes designed to overcome the issue of loss in the fiber cables. Entangled states are also required in quantum teleportation [26] and superdense coding [27].

1.2 Quantum communication

The interaction of quantum systems with the environment leads the systems to decohere. It is very challenging to isolate a quantum system from environment. Therefore it was not until recently that quantum information experiments could go out of the labs [28], be adaptable to technology and become commercial. In 2004, the world's first bank transfer using quantum key distribution (QKD) was carried out in Vienna, Austria. QKD is a method to secure communication between distant parties by creating a secret key based on single photons transmitted between two parties. In classical cryptography, two parties can share a secret key, a sequence of bits, to encrypt and decrypt any messages that they share through public channels. However if the secret key is compromised, their message would

TABLE 1.1: Secret key creation in QKD

Alice's photons	\rightarrow	\uparrow	\uparrow	\rightarrow	\nearrow	\uparrow	\nearrow	\searrow	\searrow
Bob's basis	\oplus	\otimes	\oplus	\otimes	\oplus	\oplus	\otimes	\oplus	\otimes
Bob's measurement	\rightarrow	\nearrow	\uparrow	\searrow	\rightarrow	\uparrow	\nearrow	\rightarrow	\searrow
Secret key	\rightarrow		\uparrow			\uparrow	\nearrow		\searrow

not be secure anymore. When the parties are far apart, creating any secret key in a secure manner becomes the main issue. In 1984, Bennett and Brassard proposed a way to create the secret key by using a quantum channel, now called *BB84 protocol* [29].

The idea is the following: Alice and Bob (the conventional names of the sender and receiver, respectively) have two channels, a quantum channel to transmit the quantum states of single photons and a public channel. The quantum channel is for the creation of a secret key and the public channel is for the transmission of encrypted messages. Alice first prepares a string of photons randomly choosing among four different non-orthogonal quantum states that constitute two maximally conjugate bases, for example, the states $|\uparrow\rangle$ and $|\rightarrow\rangle$ in the basis of \oplus and $|\nearrow\rangle$, and $|\searrow\rangle$ in the basis of \otimes . In each basis, one of the states corresponds to 0 and the other state to 1. Alice sends randomly chosen states through the quantum channel and Bob measures them in one of the two basis chosen randomly, as in Table 1.1. After the transmission is completed they can communicate in a public channel to compare the basis that they use for each photon and discard the bits prepared/measured in different basis. For a photon for which they use the same basis, the state that Alice prepares and the state that Bob measures should be the same which will correspond to a bit in the secret key. At the end statistically half of the times Bob would use the same basis as Alice and they end up with half of the original string that Alice prepared.

After all, in the public channel they share only the basis and Alice/Bob does not reveal the states she/he prepares/measures, and the actual photon sequence, the secret key, stays secure. However there might be someone,

an eavesdropper (usually called Eve), monitoring the quantum channel before Bob receives the photons. One strategy for Eve would be nothing but acting like Bob and measuring the photons in random basis likewise Bob. Eve could guess the right basis 50% of the times, measure the correct state and prepare a photon in that state to send to Bob. In this case no one would notice the interruption. Yet in the case when Eve's basis and Alice's basis do not match, Eve's measurement would be wrong 50% of the time and send a wrong state to Bob. If for that measurement Bob uses the same basis as Alice, they expect to record the correct state. In total, the interruption leads to a 25 % error. Therefore, as a security check, after the public discussion of the basis, Alice and Bob can also reveal some of the states in the remaining string. The mismatch of the bits reveals the existence of Eve so that Alice and Bob can disregard the key and probably try again via a different quantum channel. At the end, without revealing any important message, the existence of an eavesdropper can be noticed.

Later, in 1991 Artur Ekert proposed another QKD protocol which uses entangled photon pairs [30]. However for both protocols there is a critical obstacle in the way of using QKD world-wide: attenuation in optical fibers. The optical loss and decoherence in the fibers scale exponentially with the distance (0.2 dB/km for telecom C-band). The transmitted energy drops down to around 1 % after 100 km [31]. While fiber amplifiers can solve this issue in classical information transfer, when it comes to the quantum state transfer the *no-cloning theorem* [32, 33] prohibits that kind of method. It states that no arbitrary (unknown) quantum state can be perfectly copied. If one wants to copy an unknown quantum state, it has to be measured first, however any measurement would collapse the wave function and alter the state. Therefore employing fiber amplifiers is not possible to extend the quantum communication distance. This limitation led researchers to find other solutions.

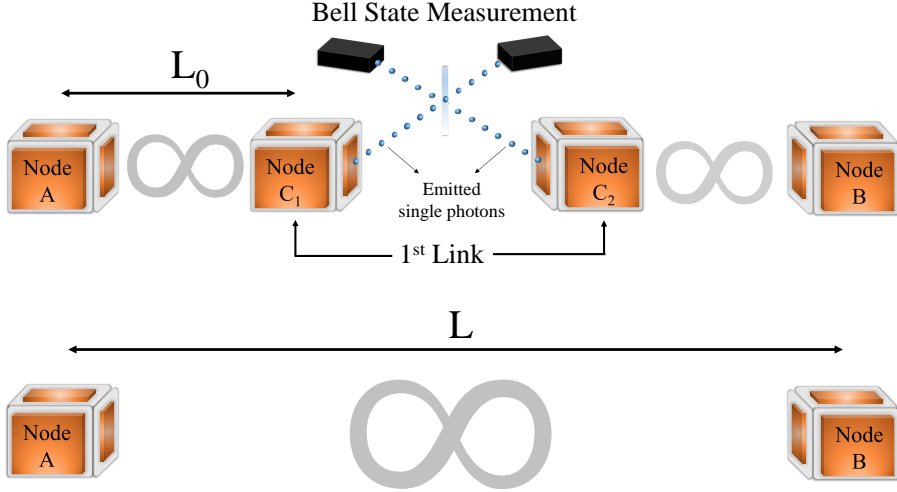


FIGURE 1.2: Entanglement swapping operation

1.3 Quantum repeaters

A possibility to overcome exponential scaling of loss and decoherence with distance is the use of quantum repeaters (QR). The concept, proposed in [34], is based on dividing the long distance into smaller segments and creating long distance entanglement from shorter distance entanglement via entanglement swapping [35].

Entanglement swapping is a way to create entanglement between two quantum systems (nodes) which may have never interacted. Suppose that there are 2 pairs of entangled systems, pair AC_1 and pair C_2B , as in Figure 1.2. While A is entangled with C_1 , C_2 is entangled with B. The task is to perform an operation which will result with the entanglement of A and B, that are separated with the distance L . If one performs a joint measurement between C_1 and C_2 in a basis of entangled states, which is a *Bell state measurement*, it is possible to create entangled states between A and B in a heralded fashion.

In order to establish a quantum channel between two distant systems, i.e. Alice and Bob, the total distance L can be divided into N smaller segments

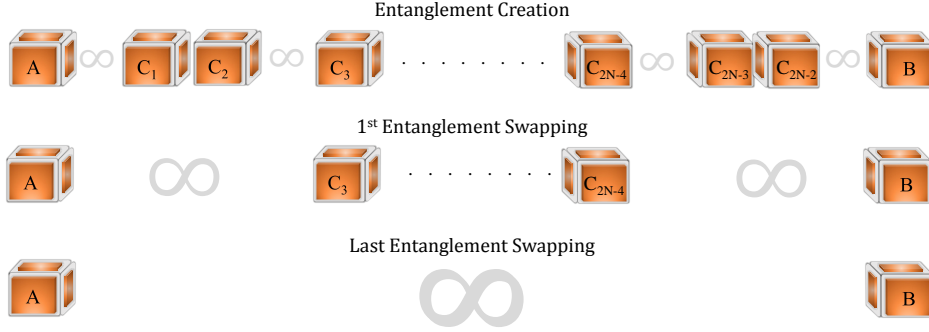


FIGURE 1.3: Quantum repeater architecture

each of which individually covers a distance of L_0 . The whole link has $N = 2^n$ elementary pairs and $2N - 2$ intermediate nodes as $C_1, C_2, \dots, C_{2N-2}$. The first step in the operation would be creating entanglement between the elementary pairs, i.e. between A and C_1 , C_2 and C_3 , ..., C_{2N-2} and B. If the nodes can emit identical photons, the detection of one photon which could have been emitted by either two of the nodes could destroy the *which-way* information and heralds entanglement between the pairs. In the second step, entanglement swapping operations at the odd number links in the order, i.e. 1st link at $C_1 - C_2$, 3rd link at $C_5 - C_6$, 5th link at $C_9 - C_{10}$, ..., are performed again via Bell state measurements. After the first entanglement swapping, the distance between the entangled nodes is already doubled. Entanglement swapping operations continue in the same way until node A and node B become entangled, see Figure 1.3. Once the operation is completed, the quantum state of a qubit can be transferred from one end to the other.

In that configuration, having a *quantum memory* at each node is required for the synchronization of entanglement swapping operations. If the entanglement can be stored in each elementary link, the different links can be essentially independent and are not required to be entangled simultaneously. This leads to a much better scaling when increasing the number of links, and the distance. In 2001, Duan, Lukin, Cirac, and Zoller suggested a scheme, now known as DLCZ scheme, that allows the implementation

of robust quantum communication over long distances with atomic ensembles and linear optics [36]. It is based on the heralded creation of collective atomic spin excitations in atomic ensembles, by the detection of a single photon. After the DLCZ proposal, many other proposals came out with suggestions of improvements, e.g. entanglement swapping based on two photon detection offering suppression of errors due to multi-photon emission [37], entanglement generation via two photon detection offering long-distance phase stability [38], photon-pair sources with multi-mode memories allowing greater wavelength flexibility and higher entanglement distribution rate [39], protocols based on local generation of high fidelity entangled pairs and two-photon entanglement swapping leading to higher quality entangled pairs which significantly improves the overall quantum repeater protocol [40]. Although different approaches may require different ingredients, they all depend on quantum memories. Otherwise all the entanglement creations in the links must be realized simultaneously. In that case the protocol called *quantum relays* cannot overcome the issue of photon loss [41].

The DLCZ proposal triggered intense experimental efforts to realize the basic building blocks of the scheme. The first experimental observation of non-classical correlations between a photon and an atomic ensemble was demonstrated in 2003 [42, 43]. Entanglement storage in two and four quantum memories have been demonstrated in 2005 and 2010 respectively [44, 45]. In 2007 and in 2008, entanglement swapping with storage and retrieval of light demonstrations, basic quantum repeater nodes have been reported [46, 47]. The protocol shows its promise also with the demonstrations of high retrieval efficiencies [48–50], and long storage times [51–54].

The quantum repeater schemes are not only limited to atomic ensembles. Proposals which uses single trapped ions [55], single ions in cavities [56], or Rydberg atoms [57]. It is worth to note that other possible solutions which do not require entangled links and quantum memories have been proposed for long distance quantum communication architectures [58, 59].

However the resources needed are way more challenging than the schemes with quantum memories.

1.4 Quantum memories

A quantum memory (QM) is a system which has the capability of storing quantum state and retrieving it back. It is called *optical* or *photonic* QM if the memory is able to store quantum information carried by photons of visible or telecom wavelength. Photonic QMs are essential not only for quantum repeaters and network architectures, but also for many prospective applications in QIS, such as deterministic single photon sources [60, 61], efficient generation of multi-photon states [62], and linear optics quantum computation [63]. Each application may demand a particular set of requirements in order to reach their best performance, therefore QMs have been implemented in several systems with different protocols. In the context of this thesis, we focus more on the requirements of quantum repeater architectures.

Strategies to create entanglement between light and matter concentrate QMs into two main types, absorptive (read-write) and emissive (read only) quantum memories [64], see Figure 1.4. *Absorptive QMs* are based on resonant interaction between light and matter. The quantum state of a single photon is mapped onto an atomic state of the QM, where it can be retrieved back when necessary. *Emissive QMs* operate via the creation of a single atomic excitation by application of a classical light pulse and the excitation is heralded by a photon. The heralding photon is entangled with the single excitation. The excitation can be read-out resulting in the emission of another photon. An emissive QM is equivalent to a photon pair source with embedded QM. In this thesis, we will investigate both types.

The system to work with is chosen depending on the requirements of the application. Therefore many systems with different properties have

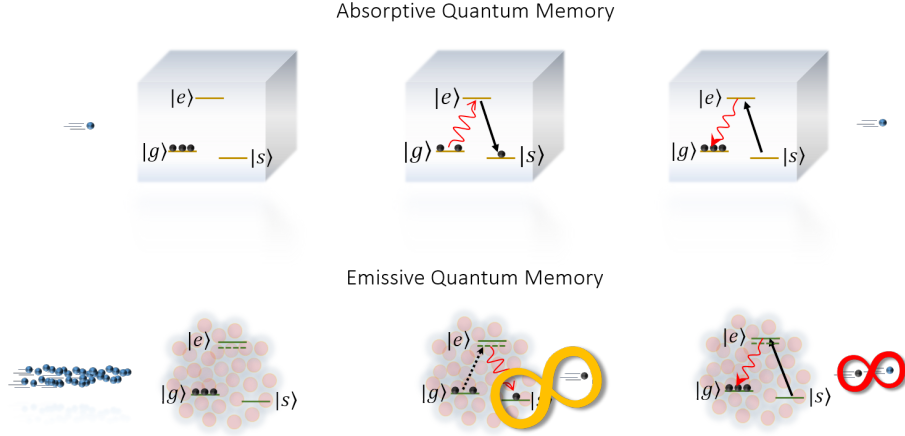


FIGURE 1.4: Absorptive quantum memory: a single photon is first absorbed by the system and retrieved afterwards. Emissive quantum memory: A classical pulse creates a single spin excitation which is then read-out.

been investigated so far. Cold atomic ensembles, hot atomic vapours, single trapped ions, rare earth ion doped crystals (REID), nitrogen-vacancy centers (NVC), and quantum dots are well-adapted platforms for QMs. The experiments performed throughout this thesis have been realized with REID QMs.

The performance of a QM is described by several figures of merit. These will be in use throughout this work therefore it is worth to introduce them here.

- **Efficiency (η)** : The efficiency of a QM can be defined as the ratio of retrieved light pulse energy to input light pulse energy. Therefore it is a good figure of merit for absorptive systems. In emissive QMs, the efficiency term is more related to the read-out of the single atomic excitation which is frequently referred to as *read-out or retrieval* efficiency. For practical QR applications which can outperform direct transmission, the desired efficiency is around 90% [31]. There are experimental results which report storage efficiencies of $96 \pm 1\%$ [65] and $87 \pm 2\%$ [66] both in cold atomic ensembles. However only coherent state of light have been stored in these

experiments. Heralded single photons created by a cold atomic ensemble have been stored in another cold atomic ensemble with a storage efficiency of $49\pm 3\%$ in 2012 [67] and very recently with an efficiency of 65% in 2017 [68]. When dealing with the quantum state storage, the effect of various noise sources begin to be very crucial. Therefore another figure of merit is necessary for this kind of characterization.

• **Fidelity (F)** : In the case of storage of a qubit, what matters is not only the amount of light retrieved but also how well the state of quantum light is preserved. We assess this characteristic with the *Fidelity* of the storage. It can be described as the overlap of the output and input states if the system is used as an absorptive memory. It is called *conditional fidelity* when we only consider the case that the memory gives an output.

$$F^c = \text{Tr}(\rho_{\text{in}}\rho_{\text{out}}). \quad (1.4)$$

It is also possible to compare the output state with a state intended to obtain, $|\psi\rangle$.

$$F_{|\psi\rangle}^c = \langle\psi|\rho_{\text{out}}|\psi\rangle. \quad (1.5)$$

An overall fidelity of around 90% is required for the whole QR for a reasonable application [31]. Hence each QM should have much more than 90% of fidelity.

• **Storage Time** : Another figure of merit is the storage time. QR architectures require QMs in order to synchronize entanglement swapping operations due to the fact that it is very unlikely to complete all the operations at the same instance when the entanglement creations are probabilistic. While the operations at links continue until successful creations, the entangled nodes have to store the quantum information. It means that the storage time has to be much longer than the time required to distribute entangled pairs. At least storage of the orders of seconds is necessary for a QR length of around 600km with storage efficiency and fidelity of 90%

[31]. Coherent classical light storage in the order of one minute [69] and coherence time of six hours have been reported with REID crystals [70].

- **Multi-mode capacity :** It can be taken as another figure of merit even though not all the QMs are able to store multi-mode light. The ability to store qubits separated in time, in frequencies or in space can shorten entanglement creation operation time, with a gain equal to the number of stored modes [39]. Therefore multi-modality can loosen the requirement of very long storage time.

- **Wavelength :** The whole idea of QR architectures is to beat the attenuation of light at telecom wavelengths in direct transmission through the optical fibers. Hence it is certainly necessary to carry on the entanglement swapping operations in the far away nodes with telecom photons. However, this criteria by itself limits the number of systems that can be exploited. Many optical QM systems operate at visible wavelength range. One approach to overcome this limitation is implementing quantum frequency converters with nonlinear crystals [71]. It is possible to efficiently convert visible light to telecom wavelengths by using this technique [72]. Another idea suggested in [73] modifies the regular QR approach by adding photon pair sources which creates two entangled photons, one resonant with QM whatever the operation wavelength is and other one at telecom wavelength, which will be used for entanglement swapping. In our research group, we investigate both approaches [74, 75].

1.5 Scope of this thesis

In this thesis, we investigate several QM protocols in REID crystals. I describe three of them in detail and present the first demonstrations of two new protocols in a $\text{Pr}^{3+}:\text{Y}_2\text{SiO}_5$ crystal. The work presented here was carried out during the period between November 2012 and May 2017.

In Chapter 2, I give an overview of REID systems in general, and for $\text{Pr}^{3+}:\text{Y}_2\text{SiO}_5$ crystal in particular.

Chapter 3 provides the basics of light-matter interactions required to implement QM protocols. I also describe the two-pulse photon echo scheme.

Chapter 4 is devoted to the experimental setup that was used in all the experiments. It includes the laser system, locking of the laser frequency with the Pound-Drever-Hall technique, details of the cryostat and the detection & data acquisition hardware.

Chapter 5 starts with the overview of spectral hole memory (SHoMe) protocol based on spin-wave storage of slow light. Later I present the first demonstration of the protocol which achieves the state of art of spin-wave storage efficiency in solid state medium with weak coherent state of light.

In Chapter 6, I first describe a well-known protocol, the atomic frequency comb (AFC). I present the results of an experiment where we convert telecom photons to 606nm and store them in our QM. Additionally I discuss more recent results of excited states and spin-wave storage obtained by using AFC protocol and present the results of the highest spin-wave AFC efficiency and lowest unconditional noise to date.

In Chapter 7, another well-known protocol, Duan Lukin Cirac Zoller (DLCZ), is discussed. I present the first demonstration of DLCZ-type protocol using photon counting in REID systems. Furthermore, preliminary results of time energy entanglement between the photons of the pair is presented by showing two-photon interference fringes with high visibility.

I conclude the thesis in Chapter 8 by giving a summary and an outlook.

1.6 State of the art in the lab

When I joined the group in November 2012, the group was 2 years old and there were already two experimental demonstrations completed in the solid

state memory part. The group had demonstrated the storage of polarization qubit in the excited state of the crystal and the storage of temporally multimode light in the spin state. Both experiments were realized by using the AFC protocol. The highest excited state AFC echo efficiency was 15% at $2\ \mu\text{s}$ storage time and the highest spin wave AFC efficiency was 5.6% at $4\ \mu\text{s}$ storage time in the spin state. 5 temporal modes had been stored in the spin state. Moreover these values were obtained by the classical light pulses, not in the single photon level. Around one year after I joined the group, we started to build a new experimental setup in an empty lab. In this thesis I present the results that we obtained in the new setup. Now, as of June 2017, we can reach excited state AFC efficiency values of around 17% at $10\ \mu\text{s}$ storage time, more than 30% spin-wave storage efficiency values in the single photon level with the Signal-to-Noise ratio of 33 ± 4 for an average input photon number of 1 by using the spectral hole memory protocol, and can store and retrieve 11 temporal modes of single spin excitation by using DLCZ-AFC protocol.

Chapter 2

The rare-earth ion doped system Pr:YSO

This chapter reviews the electronic and optical properties of the atomic system used throughout my PhD work: $\text{Pr}^{3+}:\text{Y}_2\text{SiO}_5$ (Pr:YSO). The properties discussed here are taken with a specific focus on quantum information processing applications. This chapter is inspired from several books [76–78], and PhD thesis [79, 80].

Rare-Earth ions have been studied extensively since their first discovery. There are seventeen rare earth elements in the periodic table, fifteen lanthanides as well as scandium and yttrium. Rare-earth elements’ atomic numbers range from 57 to 70 and their 4f shells are not completely filled. The 5s and 5p shells have lower energies than the 4f shell therefore electrons fill the 5s and 5p first. On the other hand the 4f shell has lower principle quantum number which keeps its radial distribution closer to the nucleus than the 5s and 5p shells’, as shown in Figure 2.1. Thus electrons at 4f shell are shielded by the filled 5s and 5p electrons. This is called *screening effect*, which limits the interaction of 4f electrons with the environment, and leads to very sharp spectral lines, e.g. optical transition linewidth in the sub-kHz range [81, 82]. By employing dynamical decoupling method,

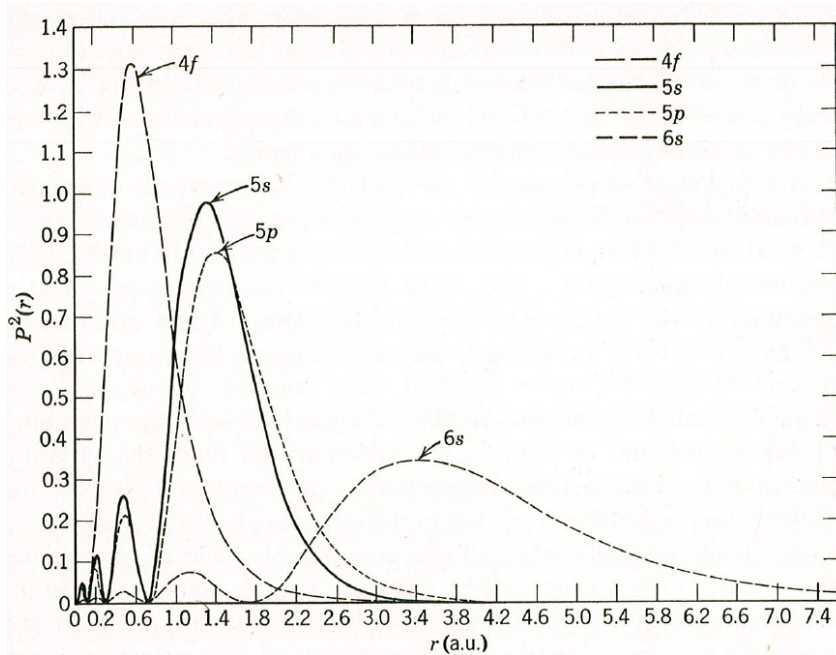


FIGURE 2.1: Radial charge density, $P^2(r)$, as a function of radius, r , for the 4f, 5s, 5p, and 6s orbitals of Gd^+ taken from [86].

the decoherence of hyperfine transitions could be reduced to observe long spin coherence times around 6 hours [70] at cryogenic temperatures. As a result the rare-earth ions exhibit unique characteristics which make them valuable for many optical applications such as solid-state lasers [76], optical amplifiers [83, 84], and optical data storage [85].

2.1 Properties of Pr:YSO

The host materials for rare earth ions depend on the application but are mostly inorganic crystals. The Y_2SiO_5 (YSO) crystal is a low symmetry (C_{2h}^6) insulator host with a bandgap of around 4.2 eV (≈ 295.2 nm or ≈ 1015.5 THz) [87]. When doped with Pr^{+3} ions, they substitute for Y^{+3} ions in the crystal lattice and introduce energy states in the bandgap. In other words the ions which interact with light are naturally trapped by the host

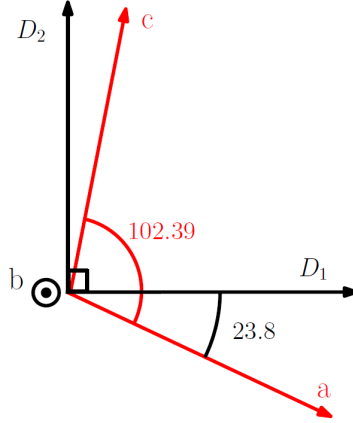


FIGURE 2.2: Orientations of the crystal and polarization axis in Y_2SiO_5 [90].

crystal lattice, hence decoherence caused by atomic motion almost disappears. However lattice phonons can still interact with the ions and cause perturbations. We cool down the crystals to liquid helium temperatures in order to minimize the issues related with phonon interaction.

The YSO crystal structure is monoclinic biaxial with unit cell dimensions $a = 1.4371$ nm, $b = 0.671$ nm, $c = 1.0388$ nm, and $\beta = 122.17^\circ$ [88]. The ionic radii of Pr and Y are 112.6 pm and 101.9 pm, respectively [89]. There are two crystallographic site that Pr ions substitute in, *site 1* and *site 2*. Site 1 is much more likely to be occupied by Pr dopant ions with respect to site 2. Therefore the optical density is higher for absorption transitions of site 1 ions. The optical $^3\text{H}_4(0) \rightarrow ^1\text{D}_2(0)$ transition is at 605.977 nm in site 1 and at 607.934 nm in site 2. We use the site 1 ions in the experiments described in this thesis.

b , D_1 , and D_2 are the three polarization axes of the Pr:YSO crystal. For maximum absorption, the polarization of light is supposed to be parallel to the D_2 axis. Their directions with respect to the crystallographic axis (a , b , c) can be determined by X-ray measurement as shown in Figure 2.2 [90].

The advantage of REID systems is their long lifetimes and coherence times. In our group, an excited state lifetime of 160 μs and an inhomogeneous broadening of around 10 GHz was measured with a 0.05% doped Pr:YSO crystal (absorption coefficient α of around 20 cm^{-1}). We also measure an excited state coherence time of 90 μs (see Chapter 3.2) at $T = 3.5$ K and without magnetic field, corresponding to homogeneous linewidth of $\gamma_h = 3.5$ kHz. The ground state hyperfine level lifetime of around 100 seconds has been reported [91]. In the measurement done in our group, the population decay shows a double-exponential behaviour with 7.5 seconds and 198 seconds decay constants. The coherence time in the ground state hyperfine level is around 500 μs [92] at zero external magnetic field. Introducing external magnetic fields and dynamical decoupling techniques, the coherence time can be pushed towards the lifetime limit [69]. All these unique properties make the Pr:YSO system a very promising candidate for a photonic quantum memory.

2.2 Energy levels

Pr (praseodymium) atoms have the atomic number 59. They lose usually 3 electrons and become Pr^{3+} when bonded to oxygen. The electronic configuration of Pr^{3+} is $[\text{Xe}] 4f^2$, i.e. there are two electrons in the 4f shell. For the understanding of energy levels, there are many interactions which should be taken into account in the Hamiltonian.

$$H = [H_0 + H_C + H_{SO}] + [H_{CF} + H_{HF} + H_Q + H_z + H_Z] \quad (2.1)$$

Here I discuss the Hamiltonian of only the lowest energy ground state. The energy levels are shown in Figure 2.3. Further detailed analysis can be found in [76, 77, 86].

Due to the screening effect, interactions of the ions in a solid matrix can be considered as perturbation of the free ion case, which is represented by the Hamiltonians on the left bracket. Central field approximation is a

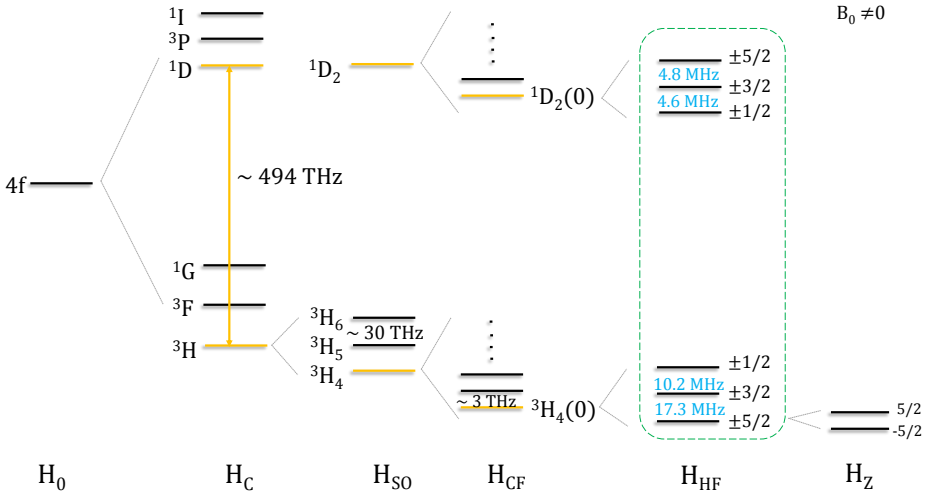


FIGURE 2.3: Energy levels of 4f electrons in Pr³⁺:Y₂SiO₅ inferred from Dieke diagram [93].

conventional approach to solve Schrödinger equation for N-electron atomic system and evaluate energy levels of lanthanide. In that context, the non-spherical electronic interactions are taken as perturbations to the spherically symmetric potentials. The first Hamiltonian (H₀) consists of kinetic and potential energy of the electrons in the field of the nucleus which is purely radial hence does not affect the energy level structure.

The Coulomb interaction (H_C) between the electrons removes the degeneracy of the 4f shell into the ground and excited terms which are represented with ^{2S+1}L . It dominates the Hamiltonian in light atoms whose radius is small hence the electrostatic interaction is strong. The total orbital angular momentum L , total spin angular momentum S , and the net angular momentum J determine the spectral terms of the ground and excited states. For two electrons in the 4f shell, $S = |\sum m_s| = |1/2 + 1/2| = 1$, and $L = |\sum m_\ell| = |3 + 2| = 5$. In order to calculate the L value of the lowest energy, we start to fill the highest m_ℓ levels which gives the smallest interaction and the minimum average repulsion. While J and S are specified numerically, L is conventionally specified with letters in the

following manner; $L = 0, 1, 2, 3, 4, 5, \dots \equiv S, P, D, F, G, H, \dots$. Therefore the spectral term of the lowest energy ground state is 3H .

The motion of electrons in the orbit around the nucleus creates a magnetic field which interacts with the electron spins. It is called spin-orbit interaction (H_{SO}) and splits the term into manifolds, $^{2S+1}L_J$. In the many electron free ion case when the 4f shell is less than half full, the ground state manifold can be built with the Hund rule, where $J = L - S$. In Pr the ground state manifold is 3H_4 .

The spherical symmetry of the dopants is disturbed by the YSO crystal. Therefore the electric field of the crystalline environment splits the ionic energy levels. Nevertheless the interaction of the electrons with the crystal field (H_{CF}) is weaker than the spin-orbit interaction thus the effect is mostly localized as perturbations within the single manifolds. It removes the degeneracy on each J manifold which can be then splitted into a maximum of $2J + 1$ levels, written $^{2S+1}L_J(n)$, $n = 0, \dots, 2J+1$. The number of crystal field levels as well as the magnetic properties of rare-earth ions depend on the number of electrons in the 4f shell. If it is an odd number, the ion, called Kramers ion, has larger magnetic moment due to the unpaired electron [94]. Ions with even number of electrons are called non-Kramers ions, i.e. Pr^{3+} which has 2 electrons in the 4f shell. For those in sites with lower than axial symmetry, it results with a “*quenching*” of the angular momentum.

H_{HF} is the hyperfine interaction between the nuclear spin momentum I and the effective magnetic field induced by the electronic angular momentum J . Pr has nuclear spin of $5/2$, thus each crystal field singlet splits into three levels labeled $\pm 1/2$, $\pm 3/2$, and $\pm 5/2$. In fact, for singlets the first order hyperfine interaction vanishes, and only the second order effect is considered. The second order nuclear hyperfine term is similar to the electric quadrupole Hamiltonian H_Q [95]. The two Hamiltonians can be written together as an effective Hamiltonian and the splittings of level due to the effective Hamiltonian is commonly called the hyperfine splittings.

TABLE 2.1: Relative oscillator strengths of hyperfine transitions in Pr:YSO. [97]

	$\pm 1/2_e$	$\pm 3/2_e$	$\pm 5/2_e$
$\pm 1/2_g$	0.55	0.38	0.07
$\pm 3/2_g$	0.44	0.60	0.01
$\pm 5/2_g$	0.05	0.02	0.93

The last two Hamiltonians, nuclear Zeeman effect H_z and electronic Zeeman effect H_Z , exist only when an external magnetic field is applied. The external field lifts the \pm degeneracy in the hyperfine levels and splits each level into two. The magnitude of the splitting is directly proportional to the amplitude of the applied field (around 100MHz/T in the ground state of Pr:YSO [96]). In the work presented in this thesis, no external magnetic field is applied.

All the 4f intra-configurational transitions are weakly allowed in REID crystals. The relative oscillator strengths of all 9 possible transitions are given in Table 2.1.

2.3 Homogeneous and inhomogeneous broadening

Homogeneous broadening refers to the spectral linewidth of a single ion's absorption and emission. It arises from dynamical processes such as lifetime and dephasing of ions in the electronic levels hence it is the same for all ions. It can be defined as

$$\Gamma_h = \frac{1}{2\pi T_1} + \frac{1}{\pi T_2^*} = \frac{1}{\pi T_2} \quad (2.2)$$

where T_1 is the population lifetime, T_2^* is the dephasing time (so-called pure dephasing) and T_2 is the overall coherence time.

The screening effect minimizes the broadening of the absorption line by diminishing the phonon-ion interaction at liquid helium temperatures. Phonon interaction dominates at higher temperatures and broadens the linewidth.

Besides the phonon interaction, magnetic field fluctuations in neighbouring atoms can increase the homogeneous linewidth. Therefore host material with low nuclear magnetic moment are preferable. An effective technique to reduce the magnetic field fluctuations is applying external magnetic field in a specific direction which results in zero first order Zeeman shift (ZE-FOZ) at a certain magnetic field strength [98]. It is a powerful technique not only for Kramers ions which are more sensitive to field fluctuations but also for non-Kramers ions to obtain long spin coherence times [69].

Interactions between rare-earth ions in the crystal may also contribute to homogeneous broadening by instantaneous spectral diffusion during the light matter interaction [99]. Introducing a low dopant concentration would be the easiest solution which increases the distance between ions and therefore reduces the interaction.

By mitigating the effects due to dephasing mechanisms, homogeneous linewidths as narrow as 122 Hz for $\text{Eu}^{3+}:\text{Y}_2\text{SiO}_5$ [82] and 50 Hz for $\text{Er}^{3+}:\text{Y}_2\text{SiO}_5$ have been reported [100].

When we probe the ensemble, the absorption profile of the crystal suggests a much broader linewidth than the homogeneous one as depicted in Figure 2.4. The reason behind it is the fact that even though each ion has a narrow linewidth, they may experience slightly different crystal field strength. The ionic radii of Pr^{3+} and Y^{3+} do not perfectly match which results in crystal strains. Furthermore lattice defects and chemical impurities are inevitable in most of the growth processes. The consequence of all these imperfections throughout the crystal appears as an inhomogeneous broadening of the absorption linewidth. It is in the order for some GHz for Pr:YSO ensembles with 0.05% doping concentration and can be reduced by decreasing the doping concentration of the crystal.

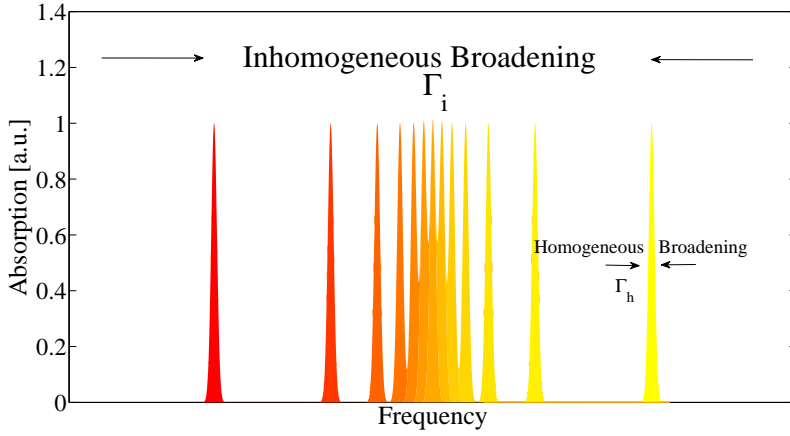


FIGURE 2.4: Representation of homogeneous and inhomogeneous broadenings in a REID crystal. Each peak represents individual single ion.

The inhomogeneous broadening in Pr:YSO crystal is around 3 orders of magnitude larger than the hyperfine splittings. The inhomogeneity in the crystal spreads all the possible transitions in a broad range of frequencies. As a consequence, an optical pulse at a certain frequency can excite many ions in all the transitions. A group of ions which resonate with the light in the same transition is considered as a *class*. With 3 ground and 3 excited state hyperfine levels, 9 possible classes can be excited with the same light pulse in a Pr:YSO ensemble. Population at a certain frequency can be distributed to other frequencies determined by the hyperfine level splitting if a long enough optical pulse from a narrow-band light source is applied. The process is called *spectral hole burning*. More details on spectral hole burning techniques and characterization of Pr:YSO ensemble can be found in Chapter 2.4 and also Nilsson *et. al.* [97].

2.4 Spectral hole burning

Spectral hole burning (SHB) is at the heart of many experiments, not only with REID crystals but also any media which has inhomogeneous

broadening [77, 101]. SHB creates a narrow transmission window within an inhomogeneously broadened absorption profile at a certain frequency which is opaque otherwise.

When we consider a REID system with two ground states and two excited states with splittings of Δa and Δb , respectively, applying a pulse to burn a hole has other consequences, see Figure 2.5. A resonant pulse at frequency ω_0 excites ions to the excited state. However the ions decay from the excited state back to the ground states. If the pulse is long enough in time, it removes ions from one ground states and the decay populates the other one. Here we assume that the lifetime of the ground state is longer than the excited state. Due to the inhomogeneous broadening larger than the hyperfine splittings, there are four classes of ions in the system. In this condition removing ions from one ground state does not create only one hole but three holes. The other consequence is the creation of anti-holes, the result of decaying ions from the excited state to the other ground state. The state becomes more populated than the equilibrium case therefore the absorption in that transitions frequency will be higher. The absorption can be quantified by the optical depth (OD) which is related with the absorption coefficient α and the length of the crystal L , $OD = \alpha L$. OD can be easily measured by a weak probe field transmitted through the crystal. An illustration of a spectral hole burning in the given system is shown in Figure 2.5. The ground state hyperfine population decay of Pr:YSO crystal is measured around 200s [79] with an optical excited state lifetime of 164 μs , making spin polarization and thus spectral hole burning easier. It should also be noted that our Pr:YSO crystal has 9 classes (see Appendix A) which makes the process much more complicated.

All the experiments we present in this thesis are based on spectral hole burning. Creating a single hole by itself can be considered as a memory preparation as we do in Chapter 5. Besides, we will tailor the absorption profile by spectral hole burning to create AFC structures in the next chapters. Therefore the control over the hole burning process to obtain the necessary hole or anti-hole spectral width and optical depth in a limited

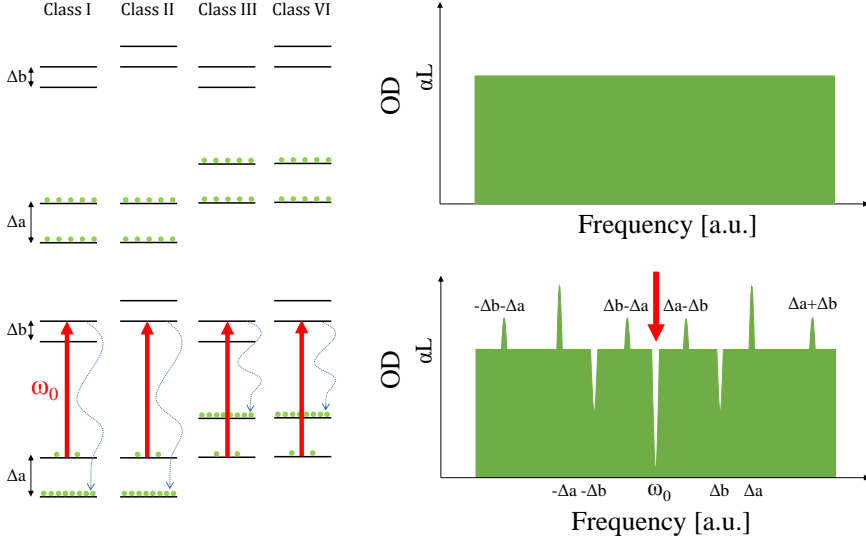


FIGURE 2.5: Illustration of holes and anti-holes in a system with two ground and two excited states. An optical pulse distributes the population at a certain frequency to the other levels. Having different classes leads to various holes and antiholes.

time is crucial. The laser linewidth and the homogeneous linewidth of the atoms limit the narrowest hole width that we can achieve in the first place. Additionally, spectral diffusion takes place in the millisecond range hence the preparation should not be slow. In our experiments, we do not see spectral diffusion. On the other hand applying strong pulses to be fast in time results with power broadening [102]. Therefore the parameters have to be carefully optimized.

2.4.1 Class cleaning and memory preparation with holes and antiholes

Antiholes may appear as unwelcome complications. However we take advantage of them as controllable absorptive features since we are capable of fine adjusting the OD, width, and frequency of not only the holes but also the antiholes.

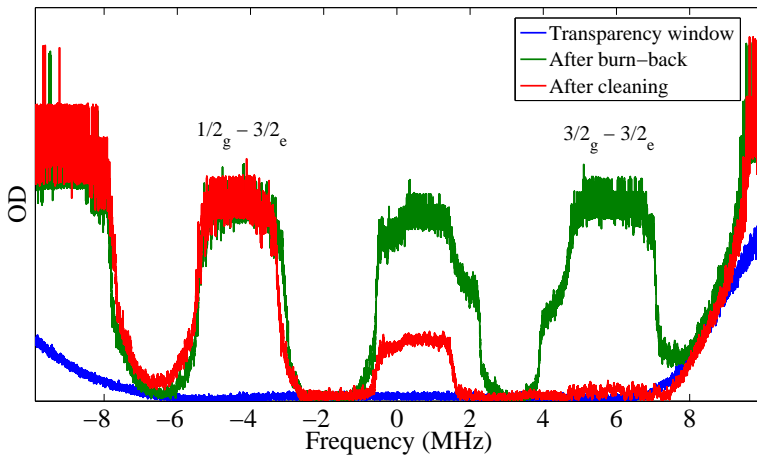


FIGURE 2.6: Memory preparation steps.

Our usual memory preparation process starts by preparing a wide transparency window of 15 MHz by sending strong laser pulses (500 pulses, $100\mu\text{s}$ long) of 20 mW and sweeping them. This has the effect of emptying the $1/2_g$ and $3/2_g$ states of a given class of ions. We then send 2-4 MHz broad burn-back pulses resonant with the transition $5/2_g - 5/2_e$ (+32.3 MHz away from the center of the pit) to repump back atoms in the states $1/2_g$ and $3/2_g$. Afterwards we clean the spin-storage state, the $3/2_g$, using 5 MHz broad pulses resonant to the $3/2_g - 3/2_e$ transition. We want this state to be totally empty, in order to reduce the noise generated by the control pulses during the spin wave storage. Moreover, these cleaning pulses have the additional effect of removing any absorption feature associated to different transitions of other atomic classes from the frequency range of interest. The process until this point takes about 90 ms. At this stage, we have a 2-4 MHz-wide single class absorption feature resonant to the transition $1/2_g - 3/2_e$, where we can prepare the specific structure that the protocol requires, for example a single spectral hole or an atomic frequency comb. Figure 2.6 shows the spectral features of the memory preparation steps.

However there is another common procedure for the spin-wave memory

protocols. When we create the desired feature at $\pm 1/2_g - \pm 3/2_e$ transition, some of the ions decay back to the $\pm 3/2_g$ state. We want to keep this state empty in order to realize spin-wave storage. Therefore we again remove the population by optical pumping the $\pm 3/2_g - \pm 3/2_e$ transition. With this final atomic manipulation, the memory becomes ready to use.

More information about class cleaning and memory preparation can be found in [79, 97, 103].

Chapter 3

Coherent light-matter interaction

This chapter is dedicated to introduce the basic theoretical concepts of light-matter interaction relevant to the experiments presented in the thesis. I have benefited from various resources in the theoretical part of the chapter [104–106]. Additionally, I describe a basic photon echo scheme, namely the two-pulse photon echo.

3.1 Evolution of a resonant two-level system

A two level atomic system is a good candidate for a stationary qubit and also the basic system to describe the physical concepts of the light-matter interaction. Here I follow the semi-classical approach where only the atoms are quantized but not the light field. The wave function of a two level system can be written as:

$$|\psi(\mathbf{r}, t)\rangle = c_1(t)|0\rangle + c_2(t)|1\rangle \quad (3.1)$$

where $c_1(t)$ and $c_2(t)$ are complex probability amplitudes of the excited state $|1\rangle$ and ground state $|0\rangle$, respectively and satisfy $|c_1(t)|^2 + |c_2(t)|^2 = 1$. The energy difference between the two states can be defined as $\omega_0\hbar$.

The density matrix operator of the wave function takes the form of:

$$\hat{\rho} = |\psi\rangle\langle\psi| = \begin{pmatrix} |c_1|^2 & c_1c_2^* \\ c_1^*c_2 & |c_2|^2 \end{pmatrix} \quad (3.2)$$

where the diagonal elements present the populations and the off-diagonal elements present the coherences. The wave function can also be written in a more general way:

$$\Psi(\mathbf{r}, t) = \sum_i c_i(t) \psi_i(r) e^{-iE_it/\hbar} \quad (3.3)$$

where E_i is the energy of the corresponding level. When a monochromatic light field is on or near resonance with the system, the Hamiltonian can be written as:

$$\hat{H} = \hat{H}_0 + \hat{H}_I(t) \quad (3.4)$$

where H_0 is the free evolution Hamiltonian and $H_I(t)$ is the interaction Hamiltonian, the time dependent perturbation term. Assuming that the light field induces dipole oscillations only in the \mathbf{x} axis, the interaction Hamiltonian can be written as:

$$\hat{H}_I(t) = e\mathbf{x}E_0\cos(\omega t) \quad (3.5)$$

where $e\mathbf{x}$ presents the dipole moment, E_0 is the amplitude of the electric field and ω corresponds to the angular frequency of the light wave. The matrix elements of the perturbation are given by:

$$H_{I,ij}(t) = -\frac{E_0}{2}\cos(\omega t)\mu_{ij} \quad (3.6)$$

where μ_{ij} is the dipole matrix element. $\mu_{11} = \mu_{22} = 0$ due to the fact that \mathbf{x} is a odd parity operator and also $\mu_{12} = \mu_{21}$.

We use the time dependent Schrödinger equation to describe the evolution of the system:

$$\hat{H}\Psi(\mathbf{r}, t) = i\hbar \frac{\partial}{\partial t} \Psi(\mathbf{r}, t) \quad (3.7)$$

The free evolution Hamiltonian has two solutions for a two level system:

$$\hat{H}_0\psi_i(\mathbf{r}) = E_i\psi_i(\mathbf{r}) \quad \{i = 1, 2\} \quad (3.8)$$

We insert the Equation 3.3 and 3.4 into the Equation 3.7, multiply with ψ_i^* and integrate over the whole space. Due to the orthogonality between the eigenfunctions we obtain :

$$\begin{aligned} \dot{c}_1(t) &= i \frac{E_0\mu_{12}}{2\hbar} (e^{i(\omega-\omega_0)t} + e^{-i(\omega+\omega_0)t})c_2(t) \\ \dot{c}_2(t) &= i \frac{E_0\mu_{12}}{2\hbar} (e^{-i(\omega-\omega_0)t} + e^{i(\omega+\omega_0)t})c_1(t) \end{aligned} \quad (3.9)$$

Now we define an important parameter, the Rabi frequency as:

$$\Omega_R = \frac{E_0\mu_{12}}{\hbar} \quad (3.10)$$

Under the rotating wave approximation we can assume that the high frequency terms, i.e. $\omega + \omega_0$, rapidly average to zero if the light is on or near resonance with the transition. Hence, we can neglect the terms $e^{\pm i(\omega+\omega_0)t}$. If the light field is resonant and in the initial case all the population is in the ground state, then we obtain a simple solution:

$$\begin{aligned} c_1(t) &= \cos(\Omega_R t/2) \\ c_2(t) &= i \sin(\Omega_R t/2) \end{aligned} \quad (3.11)$$

Therefore the population in the states oscillate with the Rabi frequency.

The average dipole moment of the system can be written with the density matrix elements

$$\langle d \rangle_\psi = \langle \psi | d | \psi \rangle = d_{12}(\rho_{21}e^{-i\omega_0 t} + \rho_{12}e^{i\omega_0 t}) \quad (3.12)$$

The Bloch sphere representation as shown in Figure 1.1 is a helpful way to visualize and understand the evolution of a two level system resonant with the light field. We can define $\tilde{\rho}_{12} = \rho_{12}e^{-i(\omega-\omega_0)t}$ and write the average dipole moment as

$$\langle d \rangle_\psi = d_{12}(\tilde{\rho}_{12}e^{i\omega t} + \tilde{\rho}_{21}e^{-i\omega t}) = d_{12}[R_1 \cos(\omega t) - R_2 \sin(\omega t)] \quad (3.13)$$

where $R_1 = 2\text{Re}(\tilde{\rho}_{12})$ and $R_2 = 2\text{Im}(\tilde{\rho}_{12})$. They are the in-phase and in-quadrature components of the dipole. The R_3 component is the population difference as $\rho_{22} - \rho_{11}$. Then the Bloch vector is defined as

$$\vec{R} = (R_1, R_2, R_3) \quad (3.14)$$

The optical Bloch equations can be written by introducing two relaxation terms, $T_1 = \gamma_{||}$ and $T_2 = \gamma_{\perp}$ for the diagonal and off-diagonal elements where $\gamma_{||}$ and γ_{\perp} are the corresponding decay constants. As stated in Chapter 2, T_1 and T_2 correspond to the excited state life-time and coherence time, respectively. The equations obtained are

$$\begin{aligned} \dot{R}_1 &= \delta R_2 - \frac{R_1}{T_2} \\ \dot{R}_2 &= -\delta R_1 - \frac{R_2}{T_2} + \Omega R_3 \\ \dot{R}_3 &= -\delta R_3 - \frac{R_3 - R_3^{eq}}{T_1} \end{aligned} \quad (3.15)$$

where R_3^{eq} is the population difference in the equilibrium condition.

The optical Bloch equations describe the effect of the light field on the atomic system. However it should be coupled with classical Maxwell equations in order to consider how the atomic system acts back on the field. In the rest frame, the Maxwell equation can be written as

$$\nabla^2 \vec{E}(z, t) - \frac{n^2}{c^2} \frac{\partial^2}{\partial t^2} \vec{E}(z, t) = \frac{1}{\varepsilon_0 c^2} \frac{\partial^2}{\partial t^2} \vec{P}(z, t) \quad (3.16)$$

where P is the macroscopic polarization and defined as

$$P(z, t) = \frac{N\mu}{2\pi} \int_0^\infty [R_1 \cos(\omega_0 t - k_z z) - R_2 \sin(\omega_0 t - k_z z)] g(\omega) d\omega \quad (3.17)$$

where N is the number of atoms, and $g(\omega)$ is the inhomogeneous broadening. After some math, the propagation equations can be written as

$$\begin{aligned} \frac{\partial \Omega_c}{\partial z} &= \frac{\alpha}{4\pi} \int_{-\infty}^{\infty} R_2 g(\Delta) d\Delta \\ \frac{\partial \Omega_s}{\partial z} &= -\frac{\alpha}{4\pi} \int_{-\infty}^{\infty} R_1 g(\Delta) d\Delta \end{aligned} \quad (3.18)$$

where Ω_c and Ω_s are the in-phase and in-quadrature parts of the field, α is the absorption coefficient, and Δ is the detuning from the frequency of the rotating frame.

Additionally the change in the atomic polarization σ can be written as follows

$$\frac{\delta \sigma(z, t)}{\delta t} = -i\delta \sigma(z, t) + i\mu^2 \Omega_R(z, t)/\hbar \quad (3.19)$$

The combination of Equations 3.15 and 3.18 represents the Maxwell-Bloch equations. Together with 3.19 they are useful to describe the memory protocols that I will present in the thesis.

3.2 Two-pulse photon echo

The two-pulse photon echo (2PE) scheme is one of the most common method to observe the evolution of the dipoles. It was first observed by Kurnit and co-workers in 1964 [107] and later explained by the same group [108]. It is a quite useful technique to measure the homogeneous linewidth of an ensemble which has inhomogeneous broadening.

The protocol is based on the Rabi oscillation and free precession. The Bloch sphere representation and the time sequence of the scheme are shown

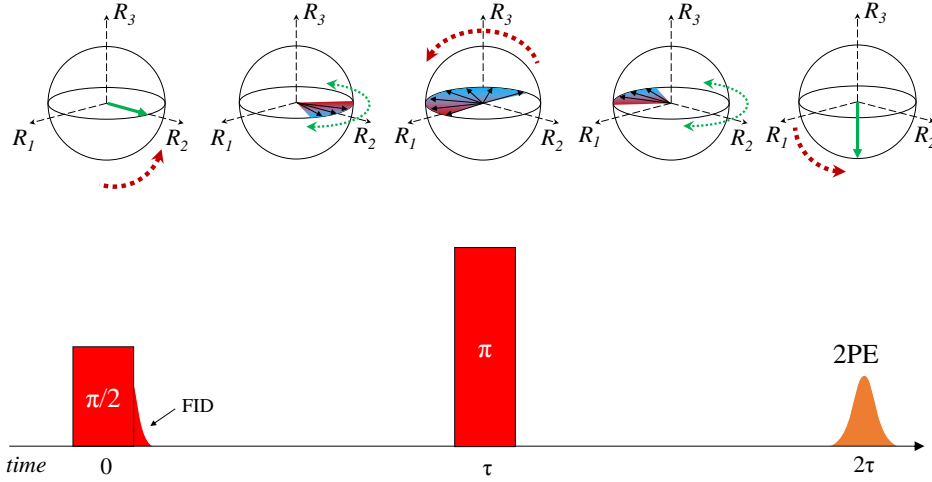


FIGURE 3.1: Evolution of the dipoles in the Bloch sphere and time sequence of the 2PE scheme.

in Figure 3.1. Initially all the atoms are in the ground state. A $\pi/2$ pulse rotates the Bloch vector around the R_1 axis and brings the system to the $R_1(0) = 0, R_2(0) = 1$, and $R_3(0) = 0$ condition right after the pulse at $t = 0^+$. At that moment all the dipoles in phase create a coherent emission called *free induction decay* (FID) [109]. Due to the inhomogeneous broadening, the dipoles evolve in time with slightly different speeds which leads to the dephasing of the system. We can describe the evolution of the dipoles for $t > 0$ as

$$\begin{aligned} R_1(t) &= -\sin(\Delta t) \\ R_2(t) &= \cos(\Delta t) \\ R_3(t) &= 0 \end{aligned} \tag{3.20}$$

We can revert the dephasing and convert it to a *rephasing* by applying a π -pulse at time τ . Each Bloch vector undergoes a 180° rotation around the R_1 axis. Their precession continues in the same direction with the same speeds however the system this time rephases instead of dephasing. A collective coherent emission occurs at time 2τ .

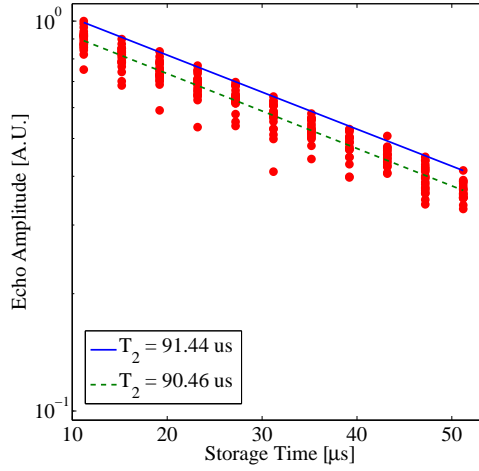


FIGURE 3.2: 2PE measurements to find T_2 value in our Pr:YSO crystal. The blue straight line is the fit to the highest values, the green dashed line is the fit to the mean average of the measurements.

We use the 2PE protocol to measure the excited state coherence time T_2 and extract the homogeneous linewidth. In order to do this we changed the storage time τ from 11.2 to 51.2 μs by steps of 4 μs and measured the emitted echoes. For each storage time the measurements were repeated 20 times as shown by the red dots in Figure 3.2. The fluctuations in the measurements is possibly due to the vibration of the cryostat which will be discussed in the next chapter. We fit the data, both the maximum and the average amplitudes, to an exponential decay containing the coherence time. From both fits, we found T_2 values of around 90 μs which corresponds to the homogeneous linewidth of 3.5 kHz.

Chapter 4

Experimental setup

This chapter presents the equipments and the setup used in the experiments described in this thesis. It is divided in three sections including the 606 nm laser sources, the cryostat, and other devices such as detectors, acousto-optical modulators, and control electronics.

4.1 606 nm lasers

The atomic system used as quantum memory, the Pr:YSO crystal, has a relevant transition at around 605.977 nm as stated in Chapter 2. For the manipulation of the Pr ions and preparation of the memory, we need a laser with a narrow linewidth (ideally sub-kHz range). However there are not many commercially available options due to the lack of the laser diodes which emit light at 606 nm. One directly applicable solution would be the use of dye lasers which can be tuned over a large spectral range. However because of the possible operational complications, e.g. difficulties in frequency stabilization, we preferred using an all solid-state option. In the experiment presented in Chapter 6, we obtain 606 nm light via sum frequency generation (SFG) of two amplified laser diodes (987 nm and 1569 nm) in a non-linear periodically poled potassium titanyl phosphate

(PP-KTP) crystal. In 2014, custom built 606 nm lasers based on second harmonic generation (SHG) process became commercially available and we continued our research with this kind of laser.

4.1.1 606 nm laser via SFG

Sum frequency generation is a non-linear frequency mixing technique to access light at a desired wavelength by exploiting the nonlinear optical properties of materials. It is a second order non-linear ($\chi^{(2)}$) parametric process which satisfies the energy conservation between two input photons, ω_1 and ω_2 , and the converted output photon, ω_3 , as in the following form:

$$\hbar\omega_1 + \hbar\omega_2 = \hbar\omega_3 \quad (4.1)$$

The intensity of the generated output field I_3 can be calculated from [110]

$$I_3 = \frac{8d_{eff}^2\omega_3^2 I_1^2 I_2^2}{n_1 n_2 n_3 \epsilon_0 c^2} L^2 \text{sinc}^2\left(\frac{\Delta k L}{2}\right) \quad (4.2)$$

where $d_{eff}^2 = \chi^{(2)}/2$, I_1 and I_2 are the input light intensities, n_1 , n_2 and n_3 are the refractive indices of the material for the three light fields, ϵ_0 is the electric permeability of free space, c is the speed of light, L is the length of the nonlinear material and finally Δk is the phase mismatch which can be written as $\Delta k = k_1 + k_2 - k_3$ [110].

The phase mismatch rises from the fact that the generated and propagated light fields experience different refractive indices. The output intensity is maximum when there is no phase mismatch, however in practice it is very challenging to reach this condition. When the mismatch becomes more than π , see Figure 4.1, the process reverses and the generated ω_3 photons start to be converted back to ω_1 and ω_2 photons.

One strategy to circumvent the phase matching issue is the quasi-phase matching technique. The idea is to change the sign of the phase periodically at the points where the interaction is about to reverse otherwise.

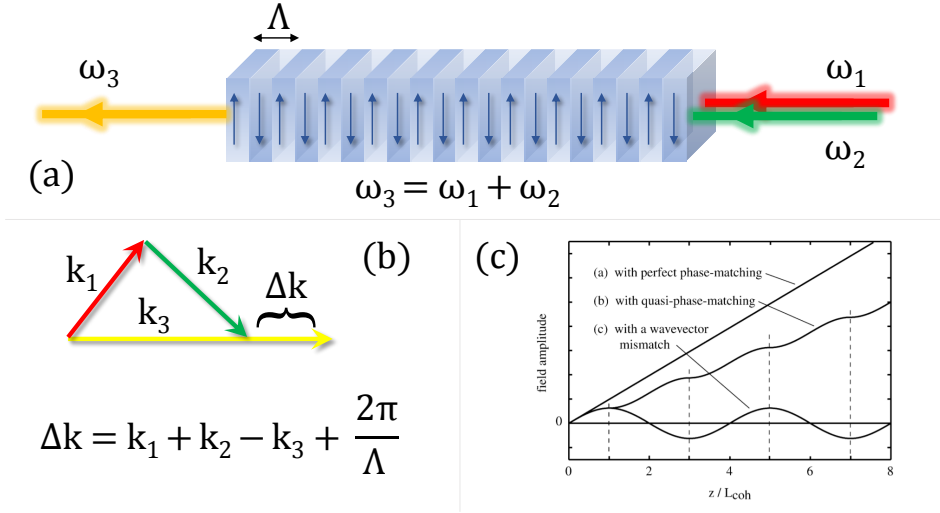


FIGURE 4.1: (a) Sum frequency generation in a periodically poled crystal. (b) Phase matching conditions. (c) Output field amplitude as a function of length of the periodically poled crystal for three different phase matching conditions [110].

Therefore the phase vectors stay in the regime where the interactions always allow to generate a ω_3 photon from ω_1 and ω_2 photons. Periodic poling of electrical polarization of a non-linear material is a method for obtaining quasi-phase matching. Ferro-electric crystals allow this kind of permanent modification in the specific regions of the material. By applying external electric field (in the order of 10 kV/mm) via patterned electrodes on the crystal surface, the direction of the electrical polarization of the crystal can be altered. With respect to the perfect phase matching condition, d_{eff} is reduced by a factor of $2/\pi$. With a poling period, Λ , around tens of micrometers, the mismatch can be compensated and written as $\Delta k = k_1 + k_2 - k_3 + 2\pi/\Lambda$.

The PP-KTP crystal is a widely used nonlinear material. Our crystal is manufactured by the company AdvR and consists of many waveguides. We produce 606 nm light with two amplified laser diodes, one at 1570 nm (Toptica, DL 100) and the other at 987 nm (Toptica, TA pro). The 1570 nm laser output is amplified by a Keopsys Erbium-doped fiber amplifier (EDFA). We have 980 mW of 1570 nm light before the in-coupling

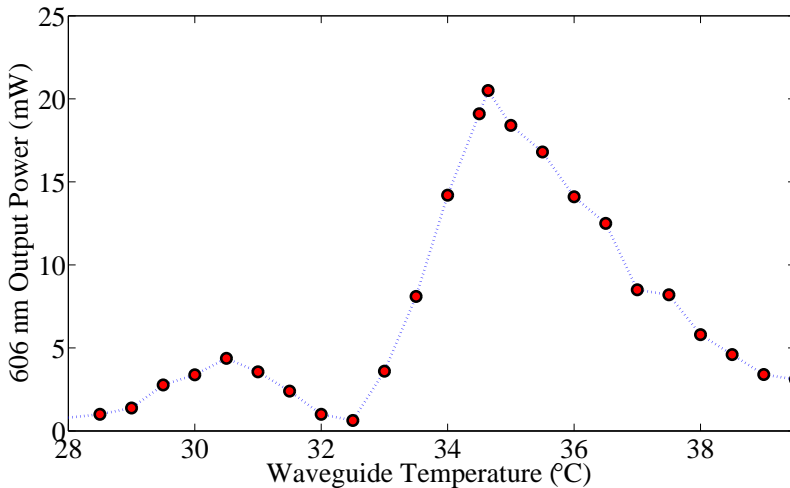


FIGURE 4.2: Output power of the converted 606 nm light via SFG as a function of the temperature of the PPKTP waveguide.

lens while the power of the 987 nm light is 380 mW. We couple the two laser fields on a dichroic mirror which reflects 987 nm and transmits 1570 nm light. The crystal, the in-coupling, and the out-coupling lenses are mounted on three translational stages to ensure the best possible coupling. The crystal has a length of 25 mm and its temperature can be adjusted with a Peltier module. We can produce 20 mW of 606 nm light with a conversion efficiency around of 85%/W. Another dichroic mirror separates the converted 606 nm light and the transmitted input lights. Temperature is one of the important factor. The temperature dependence of the generated 606 nm light is shown in Figure 4.2. We observed the optimum temperature around 34.5°C. Tuning the temperature changes the Λ so the phase matching condition and results in different output powers.

In the AFC experiment presented in the Chapter 6, the 606 nm light was created via the SFG method. Later on we switched to a SHG laser.

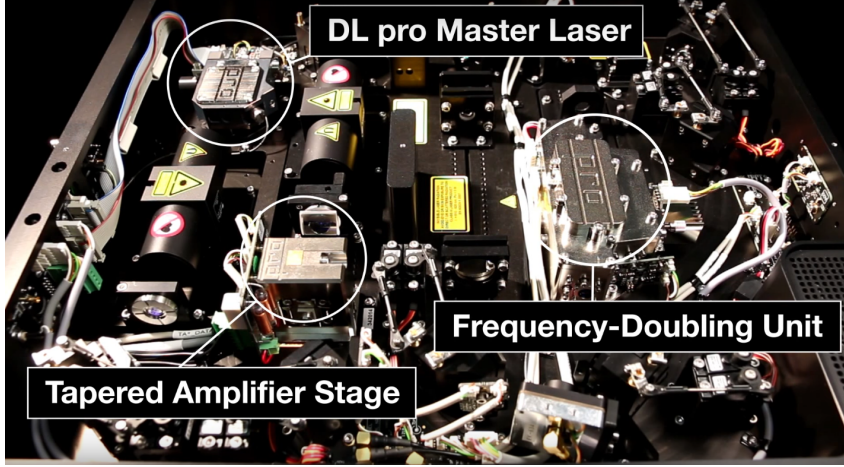


FIGURE 4.3: Main components of Toptica TA-SGH Pro laser.

4.1.2 606nm light via SHG laser

The Toptica tapered amplifier (TA) SHG Pro laser system offers directly 606 nm light at the output thanks to the built-in SHG process. The 1212 nm master diode laser has an output power of around 85 mW which is then amplified to 1.5 W by the TA. A folded ring cavity in bow-tie configuration converts the 1212 nm light to 606 nm via the SHG process. The second harmonic generation is based on the same principle as the SFG while there is only one input wavelength which is converted to its half. Hence the process is also called *frequency doubling*. The bow-tie cavity resonant to 1212 nm light allows the not converted 1212 nm light to pass through the nonlinear crystal multiple times thus boosting the total conversion. The maximum output power is around 900 mW.

We used SHG laser in the experiments presented in Chapter 5 and Chapter 7. The SHG laser provides higher power so that our transfer pulses (control or Raman pulses) are more effective. It provides also less noisy operation due to an increased signal to background ratio, which is crucial to minimize the noise in the single photon counting regime.

4.1.3 Frequency locking

The quantum memory protocols we use require stable frequency and narrow laser linewidth, ideally in the kHz range. Even though the Toptica lasers offer narrow linewidth (lower than 100 kHz in the specs), they do not perfectly match with our requirements. In this respect, we built an optical Fabry-Perot (FP) cavity to lock the frequency of the laser to a mode of the cavity with the Pound-Drever-Hall (PDH) technique. It allows active tuning of the laser frequency to the resonance frequency of the cavity. The cavity made of invar to avoid thermal drift is placed inside of a vacuum chamber under the pressure of around 2×10^{-7} mbar in order to mitigate pressure and temperature fluctuations.

The FP cavity has a length of 15 cm and consists two mirrors with the reflection of around 99.86% at 606 nm. The free spectral range of the cavity is 1 GHz with a linewidth of 1.2 MHz hence the finesse is ~ 830 . In order to realize the PDH technique, we pick up some light at 606 nm and send it through an electro-optical modulator (EOM). It creates sidebands ± 12.5 MHz away from the carrier frequency ω . A Toptica Digilock 110 module creates the local oscillator signal for the EOM. The modulated light then goes to the cavity. The light reflected from the cavity consists of the direct reflection from the first mirror and the light leaked from the same window after traveling back and forth inside the cavity many times. There is a phase shift between the direct reflection and the leaked light which destructively interfere the two components. If the frequency of the laser drifts away from ω , the frequency of the laser and the cavity will not resonate any more hence a complete destructive interference would not take place. Therefore detecting the reflected light components could help us to create an *error signal* to use as feedback into the laser. However the interference without the sidebands does not give us any hint about the direction of the drift. This is the reason why we use an EOM. The interference between the reflected light and the sidebands generate a beating pattern which has the information about the direction of the drift. The detected signal is then

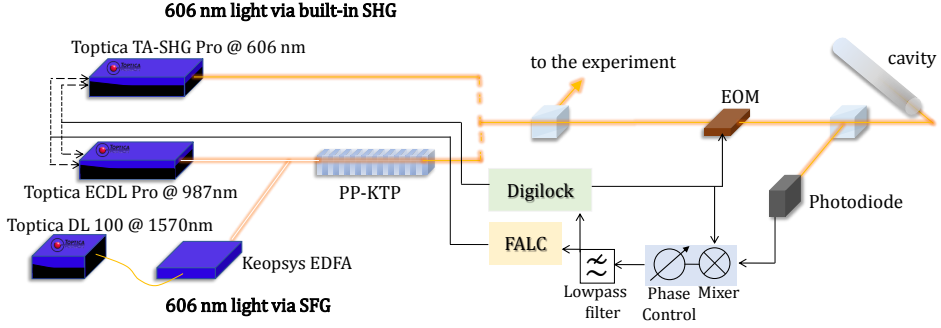


FIGURE 4.4: PDH frequency locking system. We generate 606 nm light with and lock the frequency to either built-in SHG system or the SFG system.

compared with a local oscillator signal at 12.5 MHz via a mixer. After a low-pass filter which we use to eliminate the higher order frequencies, it feeds the Fast Analog Linewidth Control (FALC) module of Topica which creates the fast feedback signal. The current control of the master diode offers the fastest response to the feedback signal therefore we lock the frequency by controlling the current unit. The Digilock unit also receives the signal, however the longer response time of the piezo provides only long term stability of the frequency. The same cavity and electronics were used for both laser sources but in the case of SFG, the feedback signal is sent only to the 987nm laser. The schematic of the system is shown in Figure 4.4.

In order to quantify the stability of the PDH system and find out the effective linewidth of our system, we send 1 ms long pulses to our Pr:YSO crystal and measure the spectral full width half maximum (FWHM) of the holes created. We first prepare a 12 MHz transmission window by optical pumping and then create a 2 MHz single class absorptive feature by back burning process. After applying a 1 ms pulse on the center of the feature, a weak pulse chirped by 3 MHz in 4 ms is sent to read out the absorption profile. The transmitted light is detected by a photo diode with a bandwidth of 300 kHz. With these conditions the resolution of the detection is around 1 kHz. We acquire many traces at different pulse

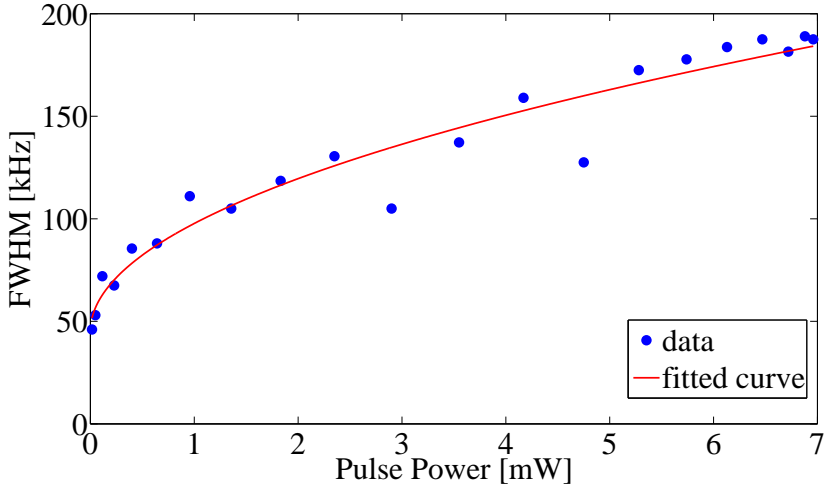


FIGURE 4.5: FWHM characterization of spectral holes created by Topica TA-SHG Pro laser at different pulse powers in 1 ms.

powers of the hole burning beam and we fit the experimental data with the power function of the form $\text{FWHM} = a + b \times \text{Power}^{1/2}$ since the power scales with the square of the electric field amplitude as follows [111]

$$\gamma_{PB} = \gamma_0 \sqrt{1 + (2\Omega/\gamma_0)^2} \quad (4.3)$$

where γ_0 is the natural linewidth, and Ω is the Rabi frequency. We estimate that the linewidth at zero power, where supposedly the power broadening does not affect the the hole width, is around 44 kHz as shown in Figure 4.5. However, assuming that the width of the hole is limited by the laser linewidth, due to the fact that we probe the spectral holes with the same laser, the effective linewidth can be found by calculating the deconvolution of two functions with the same FWHM. We assume that the emission spectrum of the laser is of Lorentzian shape and that there is no low-frequency noise from the electronics coupled to the laser. From the deconvolution of two Lorentzian function we obtain around 22 kHz natural linewidth.

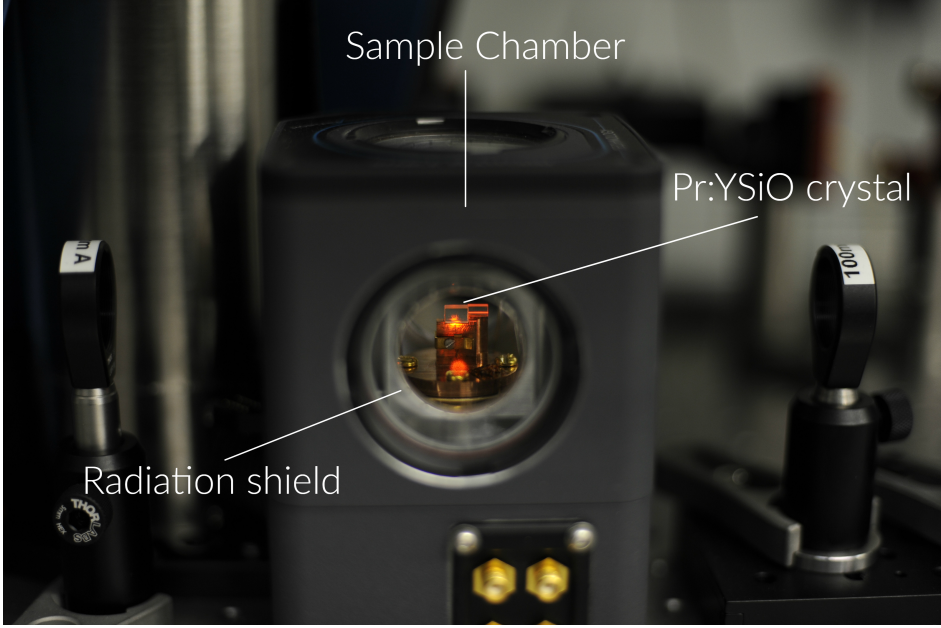


FIGURE 4.6: The cryostation chamber and the samples.

4.2 Cryostat

Our memory crystal reveals its unique characteristics only when it is cooled below 5 K as mentioned earlier in Chapter 2. We use a closed cycle liquid helium cryostat from Montana Instruments, named Cryostation, which offers low vibrations and stable thermal performance (~ 10 mK) at the base temperature. It has 5 optical ports with around 60° angle of view which greatly facilitates optical alignment.

There are two main stages to provide temperature below 5 K. The first stage is cooled down to 40 K and thermally coupled to a radiation shield which surrounds the sample. The vacuum housing below 0.09 mTorr pressure provides the interface from room temperature to the 40 K stage. The second stage consists of the sample platform with the sample mount cooled down below 5 K. The system operates with the cooling power of around 100 mW at 4 Kelvin and 1 kW of power input.

The sample chamber is rigidly fixed to the optical table just like any optical element and isolated from the cryo-cooler vibrations using a very specialized thermal link. Nevertheless the measurements are still affected by the vibrations caused by the helium compression and expansion. We synchronize our measurements with the 1 Hz compressor cycle thanks to the built-in Hall probe sensor placed at the top of the cold head. A small magnet on the top of the displacer triggers a Hall probe signal which is later converted to a TTL signal for the synchronization.

Figure 4.7 shows how our signal is affected by the vibrations. The signal amplitude values, blue dots, correspond to the measurements of the AFC echo signals (See Chapter 6). We prepare the memory in the first 150 ms and delay the input pulse for each data point. The decay time of the first part until 500 ms is 1.1 s which is limited not only by the T_1 of the ground state but also related with the deterioration of the AFC in time. In one cycle, there are two vibrational regions at around 50 ms and 600 ms where the signal is extremely affected and diminished. The first part lasts 100 ms while the second one takes 200 ms. Therefore we adjust the preparation of the memory accordingly. Usually memory preparations start with creating a transparency window and then creating a single class absorptive feature. These processes are not too much affected by the vibration. We realize these processes in the first vibrational window. However tailoring the absorptive feature and sending/detecting pulses are much more delicate operations. We squeeze the whole process before the second vibrational region. If we want to send more pulses, it is possible to pause the process during the second part and continue 200 ms later. Yet, after such a long time, the amplitude of the signal is already 60% of its maximum.

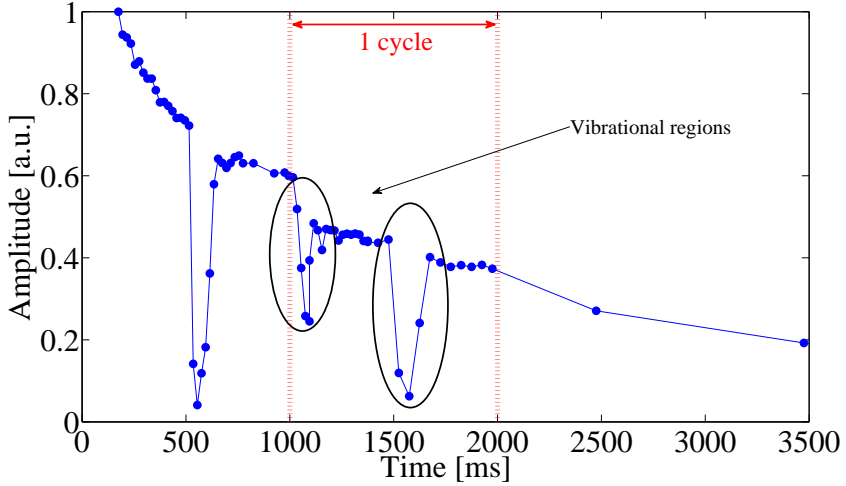


FIGURE 4.7: Effect of the vibration of the cryostat on the AFC echo signal. We can also see the exponential decay of the signal.

4.3 Detectors and other electronics

4.3.1 Classical detectors

Our experiments require different detectors and detection techniques. Classical light detection is more straightforward than the photon counting. Our main detector for the classical light is a ThorLabs 450A photo detector with switchable gain. The responsivity of the detector is $17 \text{ mV}/\mu\text{W}$ with 4 MHz bandwidth at the gain of 10^5 and $180 \text{ mV}/\mu\text{W}$ with 300 kHz bandwidth at the gain of 10^6 . The gain of 10^5 is sufficient to detect retrieved classical echo signals from the memory. High responsivity becomes important when it is required to send pulses at low intensity for reading the spectral features such as holes and AFC without destroying the feature. We can compensate the low detection bandwidth by increasing the time duration of the frequency sweep. All data measured in the classical regime, i.e. pulses, echoes, spectral hole and AFC traces, presented in this thesis were acquired with this detector. We also use other photo diodes, such as ThorLabs PDA36A-EC and PDA10A-EC, as reference detectors and for characterization purposes.

The oscilloscope we use to analyze the signals of the detectors is a Tektronix DPO5034. It has 350 MHz bandwidth and 5 GS/s sample rate. We take advantage of fast frame data acquisition mode when we do repetitive measurements while changing a parameter at a time.

4.3.2 Single photon counters

The equipments become more sophisticated when we want to detect single photons. The single photon detectors (SPDs) that we use are based on semiconductor avalanche photodiodes (APD). They rely on the generation of large current flow due to the avalanche breakdown of the semiconductor sensor when exposed to high electric field. We use a PicoQuant τ -SPAD module, an Excelitas AQRH-14FC module, and a Laser Component 10C-FC module. All the SPDs have efficiency of around 60% (including the fiber coupling) at 606 nm and the dark count rates are ranging from 10 Hz to 45 Hz. In experiments presented in Chapter 5 and Chapter 6 we used only the PicoQuant τ -SPAD module with 10 Hz dark count. In the experiment discussed in Chapter 7, we use the PicoQuant τ -SPAD module for antiStokes detection, the Excelitas module with 45Hz dark count for Stokes detection. For the auto-correlation measurements the Laser Component module was also used.

The extreme sensitivity of SPDs makes them very vulnerable. We place home-made acoustic mechanical shutters in front of the SPDs to protect them from any incidence of strong pulses and leakages during the preparation time of the memory. However the response time of the mechanical shutters is not fast enough when we have to send a strong pulse, i.e. a read pulse, just a few microsecond before the detection window. In that case acousto-optic modulators (AOM) with rise time of a few tens of nanoseconds are convenient. We use two AA Opto Electronics MT200 AOMs to gate the read pulses. The reason behind using two AOMs is that the first AOM shifts the frequency of the light and we have to shift it back with the second one for the spectral filtering stage.

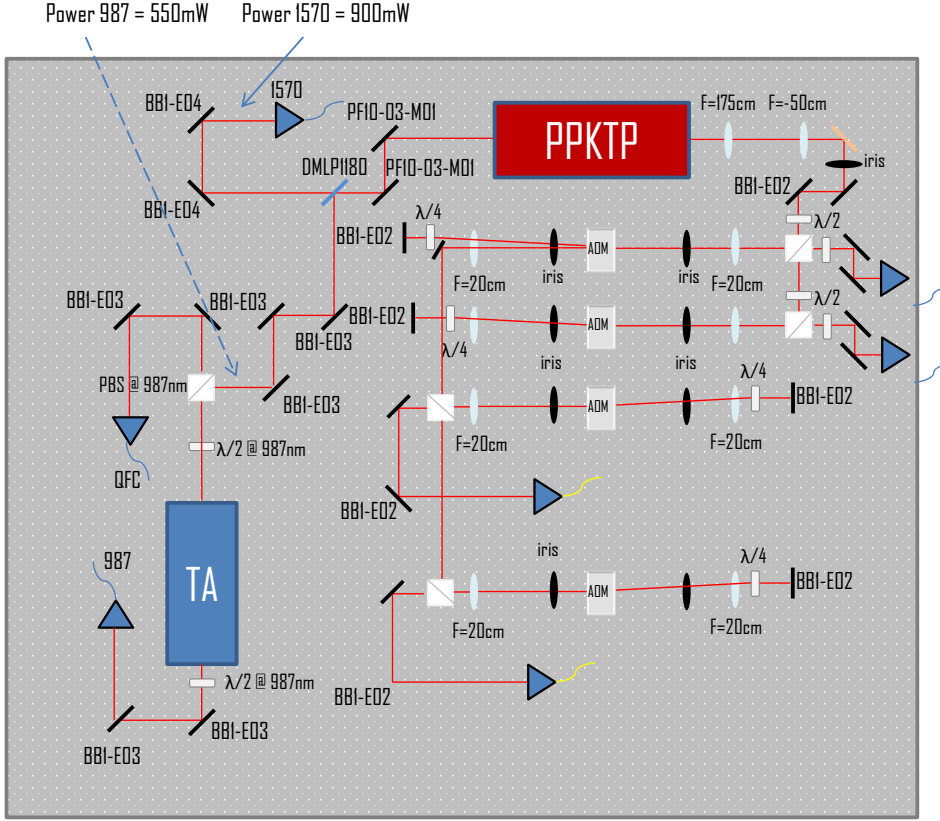


FIGURE 4.8: Schematic of the laser table with various AOM lines.

4.3.3 Pulse creation for memory preparation

AOMs are necessary not only for temporal gating but also for the memory protocols. They are capable of providing a high degree of control over frequency, amplitude, phase, and shape of the pulse. In order to create all the pulses needed for the preparation and the probing of our quantum memory, we have 4 AOM lines in double pass configuration, a strategy to cancel the deflection of the beam during frequency sweeps. They are driven by Signadyne electronics and the required power is provided by AA Opto Electronic AMPA-B-34 RF amplifiers.

The Signadyne hardwares and the software ensure total control over the

pulse sequences, the synchronizations, and the data acquisition. Two analog modules, a SD-PXE-AOU with 500 M/s sampling rate and 200 MHz output and a SD-PXE-AUO AWG with 1 G/s sampling rate and 400 MHz output, drive the AOMs and control the pulse sequences. The ability of generating arbitrary waveform (AWG) is a key resource to create the most effective AFC and pulse shapes. The timings of the shutters and the data acquisition are controlled with a SD-PXE-DIO digital module. The synchronization between cryostat trigger, pulse generation, shutters, gating AOMs, and data acquisition is managed by PROCESSflow software, based on LabVIEW. A SD-PXE-TDC Time-to-digital module with 320 ps resolution provides the data acquisition from SPDs. The data acquisition is controlled with another software called VIRTUALknob. All the four modules are mounted into a National Instrument chassis PXIe-1073.

Chapter 5

Spectral Hole Memory

The first quantum memory protocol that I present is the spectral hole memory (SHoMe). The idea and the theoretical work were proposed by Lauro and coworkers [112] in 2009 from the group of Thierry Chanelière and Jean-Louis le Gouët. The first demonstration was realized by a collaboration between our group, Chanelière’s group, and M. Florencia Pascual-Winter in 2016. In this chapter I will first introduce the idea and the theoretical background. I will then describe the experimental details. Finally I will present the results, including a memory protocol demonstration in the classical and single photon regime. The experiments presented in this chapter was conducted at ICFO while the numerical simulations were done by T. Chanelière. These results were published in Physical Review A as a rapid communication [113]. Some parts of this chapter are taken directly from the paper.

5.1 Introduction

SHoMe is a simple and a robust alternative protocol to the electromagnetically induced transparency (EIT), a well-known technique for quantum

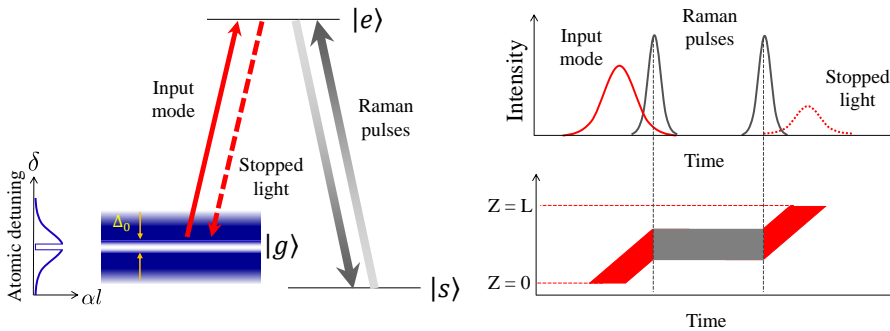


FIGURE 5.1: Schematic description of SHoMe protocol. Left panel: spectral hole and the hyperfine levels. Right panel: pulse sequence and the position of the light pulse along the crystal.

storage of light [67, 114–116]. EIT relies on the creation of a narrow transparency window in an otherwise opaque medium, thanks to the application of a control field. Stopped light based on EIT has also been demonstrated in rare-earth-doped crystals (Pr:YSO) [117], leading (together with dynamical decoupling techniques) to ultra long storage time for bright pulses [118], up to the regime of 1 minute [69], the longest light storage time demonstrated so far. However, the efficiency values in these experiments were around few percent at most. Only recently has a multi-pass configuration been implemented in a Pr:YSO crystal to increase the effective optical depth of the medium and to store classical pulses for a few μs with an internal efficiency of about 76% [119]. Nonetheless, EIT has not yet been demonstrated at the single-photon level in doped crystals. This may prove challenging, because of the noise induced by the control field during the readout.

The SHoMe protocol proposed by Lauro et al. [112] uses a permanent transparency window created in a doped crystal by spectral hole burning. While the protocol is similar to EIT because it is based on slow light, there are two important differences. First, the transparency window is not created dynamically with a control pulse, but by optical pumping way before the photons to be stored enter the medium. Second, the photons

excite optical coherence with off-resonance atoms. There is therefore no dark-state as in EIT. This becomes crucial in the single photon regime. Slow light experiments based on spectral holes have been performed before with bright pulses [120–122], but without the possibility for storage. This protocol enables us to reach high efficiencies and single-photon level operation.

The storage mechanism depicted in Figure 5.1 is based on the sequential conversion of the optical coherence into a spin coherence, using short Raman π pulses. This is important in practice because the Raman pulses can be much shorter than the retrieved single photon, which enables temporal filtering. This greatly facilitates the operation at the single-photon level. Thanks to the robust memory preparation, we demonstrate storage and retrieval efficiencies around 40% for bright pulses. In addition, we store and retrieve weak coherent pulses at the sub-photon level with an efficiency of 31%, the highest achieved so far for a single-photon-level solid-state spin-wave optical memory [123, 124]. We reach an unconditional noise floor of $(2.25 \pm 0.25) \times 10^{-3}$ photons/ μ s. For a detection window of 4μ s, this leads to a signal-to-noise ratio of 33 ± 4 for an average input photon number of 1 (together with a slightly reduced efficiency of 23%), the highest demonstrated so far in a crystal.

5.2 Theoretical background

The pulse propagation and storage is modeled by the Schrödinger-Maxwell equations in one dimension (along z). For three-level atoms, the rotating-wave probability amplitudes C_g , C_e and C_s for the ground ($1/2_g$), excited ($3/2_e$) and spin ($3/2_s$) states, respectively, are governed by the time-dependent Schrödinger equation:

$$i\partial_t \begin{bmatrix} C_g \\ C_e \\ C_s \end{bmatrix} = \begin{bmatrix} 0 & \mathcal{E}/2 & 0 \\ \mathcal{E}/2 & -\Delta & \Omega/2 \\ 0 & \Omega/2 & 0 \end{bmatrix} \begin{bmatrix} C_g \\ C_e \\ C_s \end{bmatrix} \quad (5.1)$$

where $\mathcal{E}(z, t)$ is the envelope of the input signal. As a consequence, C_g , C_e and C_s depend on z and t for a given detuning Δ within the inhomogeneous broadening. Raman pulses applied on the $3/2_e \rightarrow 3/2_g$ are described by the envelope $\Omega(t)$ which does not depend on z because the state $3/2_g$ is initially empty (no absorption). The Raman beam satisfies the two-photon resonance condition. We neglect the decoherence in this first approach since we are mostly interested in modeling the efficiency for storage times shorter than the coherence time.

The propagation of the signal $\mathcal{E}(z, t)$ is described by the Maxwell equation that can be simplified in the slowly varying envelope approximation:

$$\partial_z \mathcal{E}(z, t) + \frac{1}{c} \partial_t \mathcal{E}(z, t) = -\frac{i\alpha}{2\pi} \int_{\Delta} g(\Delta) C_g C_e^* d\Delta \quad (5.2)$$

The term $C_g C_e^*$ is the atomic coherence on the $1/2_g \rightarrow 3/2_e$ transition, proportional to the atomic polarization. The light coupling constant is directly included in the absorption coefficient α . The Schrödinger-Maxwell equations (5.1, 5.2) can be further simplified because the signal is weak. In the perturbative regime $C_g \simeq 1$, so the atomic evolution is only described by C_e and C_s .

Slow-light propagation (without Raman pulses) can be described analytically because in that case $C_s = 0$ thus reducing eq. (5.1) to the evolution of C_e only [125]. For the storage step (with Raman pulses), the Schrödinger-Maxwell equations are integrated numerically. For a given inhomogeneous detuning Δ , we calculate the atomic evolution (5.1) by using a fourth-order Runge-Kutta method. After integrating over the inhomogeneous broadening using the *hyperlorentzian* function (5.3) for $g(\Delta)$, the propagation equation (5.2) is integrated along z using the Euler method.

5.3 Experiment

In the SHoMe experiment the source of coherent light at 606 nm is the Toptica TA-SHG-pro laser described in Chapter 4.1.2. The input pulse has a power of $150\text{ }\mu\text{W}$ and waist of $35\text{ }\mu\text{m}$ at the memory crystal. The power of the Raman pulse is 20 mW and the waist is $150\text{ }\mu\text{m}$. We use the Raman mode also for the memory preparation. Two beams overlap on the memory crystal, a 0.05 % doped Pr:YSO sample of length $L = 5\text{ mm}$, located in our cryostat operating at 3.5 K. After the storage, depending on the intensity of the input pulse, there are two methods of detection (see Figure 5.2). In the case of a classical input pulse, the retrieved signal is coupled in a polarization maintaining single-mode fiber and collected with a photo detector. In the weak coherent state case, there are several filtering stages which will be described in the following section.

5.3.1 Characterization with classical light

The beginning of the memory preparation procedure is describe in Chapter 2.4.1. In this experiment, the absorptive feature created is 2.1 MHz wide. The spectral hole is created by burning a narrow hole in the center of this feature at the frequency of the $\pm 1/2_g \rightarrow \pm 3/2_e$ transition. Compared to a bare hole burning procedure, this technique has three advantages. It permits to address only a single class of ions (thus allowing the Raman pulses to address only one transition), to empty the spin storage state ($3/2_g$), and also to control the optical depth of the spectral hole, by varying the burn back power used to create the single class absorption feature.

An example of absorption trace with a spectral hole, about $\Delta_0 = 230\text{ kHz}$ wide and of optical depth $\alpha L = 8.7$, is provided in Figure 5.3. Due to the limited dynamical range of the photodetector, we cannot directly measure the optical depth of the spectral hole at the $1/2_g \rightarrow 3/2_e$ transition. We extrapolate the value by fitting the hole on the $1/2_g \rightarrow 5/2_e$ transition

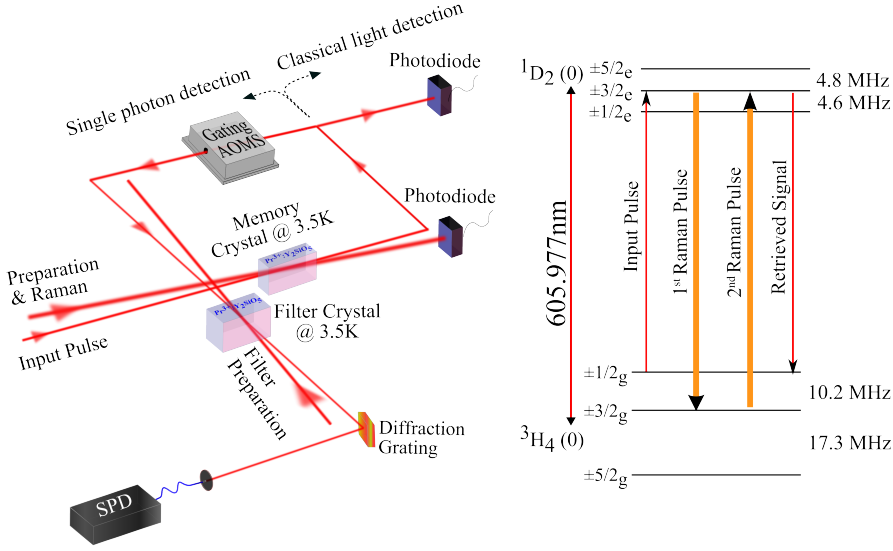


FIGURE 5.2: Left panel: experimental setup. The detection method depends on the input pulse intensity. Right panel: hyperfine splitting of the first sub-levels (0) of the ground 3H_4 and the excited 1D_2 manifold of Pr^{3+} in YSO crystal.

(shown in the inset of Figure 5.3), which is not affected by the detector non-linearity, and applying a scaling factor according to the relative oscillator strength of the two optical transitions [97]. The validity of our approach is tested by preparing weakly absorbing features and comparing the directly measured optical depth with the one extrapolated.

The shape of the hole is mostly due to frequency jitter of the laser. To account for it, we fit the absorption profile to a *hyperlorentzian* function given by the equation

$$g(\Delta) = 1 - \frac{1}{1 + |2\Delta/\Delta_0|^n} \quad (5.3)$$

($n = 2$ for a lorentzian), where Δ is the frequency detuning. From the fit, we obtain the previously mentioned values $\Delta_0 = 230$ kHz with $n = 3.0$ and $\alpha L = 8.7$.

The light storage sequence is depicted in Figure 5.4. An input pulse is sent resonantly to the spectral hole prepared in the $1/2_g \rightarrow 3/2_e$ transition.

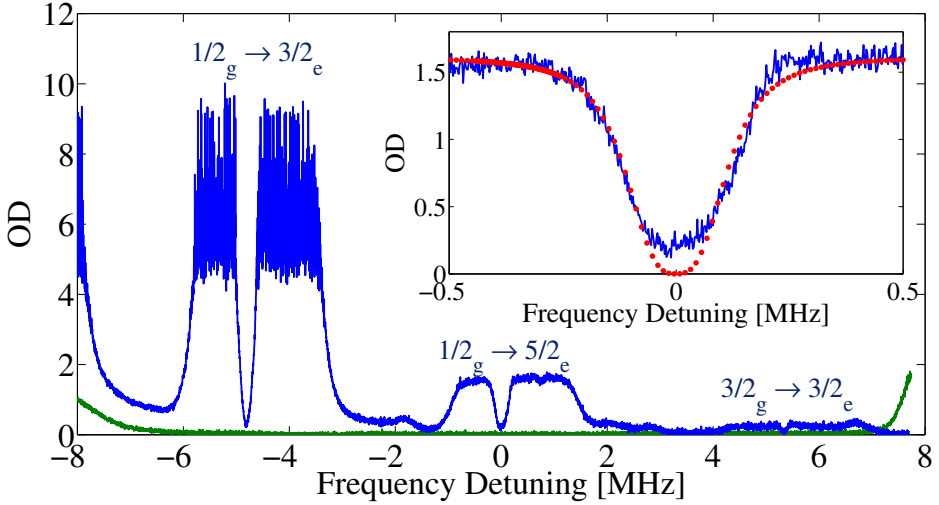


FIGURE 5.3: Spectral holes burnt in 2.1 MHz-wide single class absorption features. Inset: magnification of the spectral hole resonant with the $1/2_g - 5/2_e$ transition. The fit of the hole shape (see text for the details) is also shown.

The Gaussian pulse has a duration of $3\ \mu\text{s}$ (full width at half maximum, FWHM). The black dot trace in Figure 5.4 represents the input pulse, linearly polarized perpendicular to the D_2 axis to minimize the absorption, travelling through the transparency window. We assume that it is not delayed hence we take it as a reference. When the pulse penetrates through the spectral hole presented in Figure 5.3, it is slowed down by approximately $5\ \mu\text{s}$ (green solid circles in Figure 5.4). The delayed pulse is stretched and slightly attenuated with respect to the input pulse because its bandwidth $\sim 150\ \text{kHz}$ FWHM is comparable to the more squarish hole width $\Delta_0 = 230\ \text{kHz}$. A longer pulse would be less stretched but not sufficiently separated from the input for the spin storage step [112].

We then transfer the optical collective excitation to a spin-wave using a short Raman pulse (grey square trace in Figure 5.4) on the $3/2_e \rightarrow 3/2_g$ transition. After a controllable time T_s , a second Raman pulse triggers the pulse emission by reconvertng the spin-wave into an optical excitation that will slowly propagate through the crystal. This is shown with the blue solid trace in Figure 5.4. Since the delay of the slow light is not

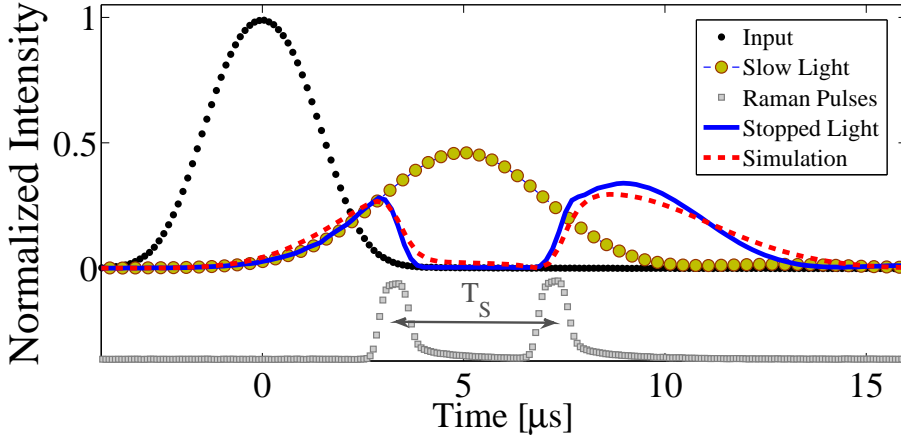


FIGURE 5.4: The spectral hole memory scheme. Black dotted trace: input pulse; green solid circles: slowed pulse; blue solid trace: stopped light; grey square trace: Raman pulses (arbitrary units); red dashed trace: the numerical simulation of stopped light.

sufficient to completely compress the initial pulse into the crystal, some light escapes before we send the first Raman pulse. For this measurement, the storage and retrieval efficiency η_S , calculated as the ratio between the areas of the retrieved pulse (after the second Raman pulse) and the input pulse, is 39 %.

The overall transfer efficiency is calculated as the ratio of the retrieved light to the transferred part of the slow light and found to be 64 %. It includes the transfer efficiency of the Raman pulses and the decoherence in the spin-state, around 8 % for 4 μ s storage 25 kHz linewidth. Hence the individual Raman pulse efficiency is around 83 %.

The stopped light temporal profile can be well reproduced by our numerical simulation described in Chapter 5.2. The result is given in Figure 5.4 with the red dashed trace. To account for a possible imperfection of the Raman transfer to the spin state, we have adjusted the Raman pulse area to 0.85π instead of π . This artificially incorporates the decoherence mechanism that is not included in our model.

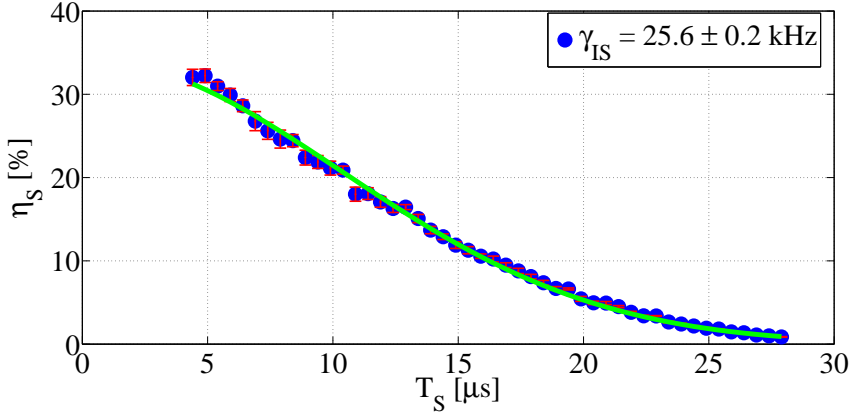


FIGURE 5.5: Storage efficiencies as a function of the delay T_s between the two Raman pulses. The decay is fitted with a Gaussian profile and the inhomogeneous spin broadening of $\gamma_{IS} = (25.6 \pm 0.2)$ kHz is extracted.

In order to characterize the storage, we investigate the efficiency of the stopped light as a function of the delay between the two Raman pulses, T_s , and of the hole optical depth. We show in Figure 5.5 that the decay of the signal is compatible with the inhomogeneous broadening of the spin transition ($\gamma_{IS} = (25.6 \pm 0.2)$ kHz) measured in an independent experiment with the same crystal, confirming that the pulse energy is stored as a spin wave [123, 126, 127].

In Figure 5.6 we compare the experimental values of storage efficiencies (red circles) and the results of the numerical simulations (blue squares) as functions of the optical depth αL . For these measurements, the position of the first Raman pulse is always optimized in order to maximize the efficiency since the group delay decreases at lower optical depths. We observe that the efficiency grows steadily as a function of optical depth. The maximum storage and retrieval efficiency observed is around 39 %, for a group delay of 5 μs and $T_s = 4$ μs. The experimental measurements are well reproduced by the numerical simulations, thus supporting our analysis.

We show the relation between the storage efficiency, time delay and the

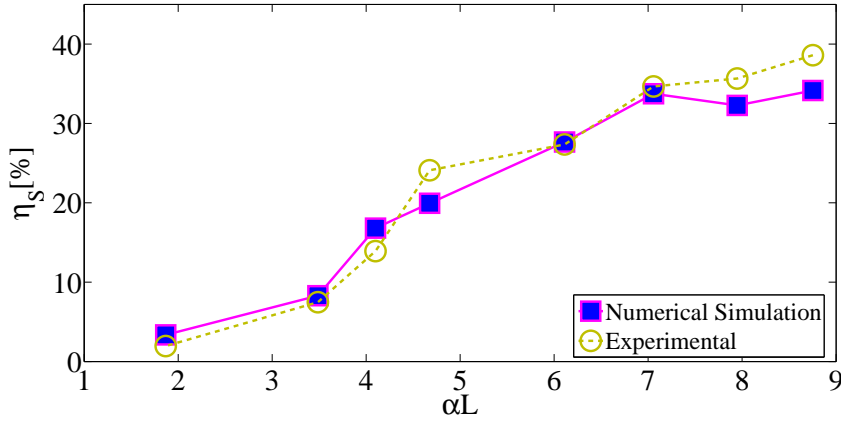


FIGURE 5.6: Storage efficiencies (experimental: red circles; numerical simulation: blue squares) as a function of the hole optical depth.

width of the spectral hole in Figure 5.7. The FWHM of the input pulse is kept $3 \mu\text{s}$ while we sweep the frequency of the hole burning pulse in order to change the hole widths and observe the effect of different widths on the efficiency of the stopped light and on the time delay of the slow light. On the upper panel we plot four spectral holes with different widths. We follow the same strategy as in Figure 5.3 to calculate the optical depth of the $1/2_g - 3/2_g$ transition. On the lower panel we see that the time delay decreases (the group velocity increases) as the spectral holes become larger. On the other hand, the storage efficiency does not scale directly with the width of the spectral hole. There is an optimum hole width to obtain the highest storage efficiency. When the spectral hole is narrower than the optimum width, the pulse is partly absorbed by the ions and cannot be converted back. If the hole width is wider, then the pulse cannot sufficiently interact with the medium hence the storage become again less efficient. The optimum hole width varies with the OD and also with the FWHM of the pulse.

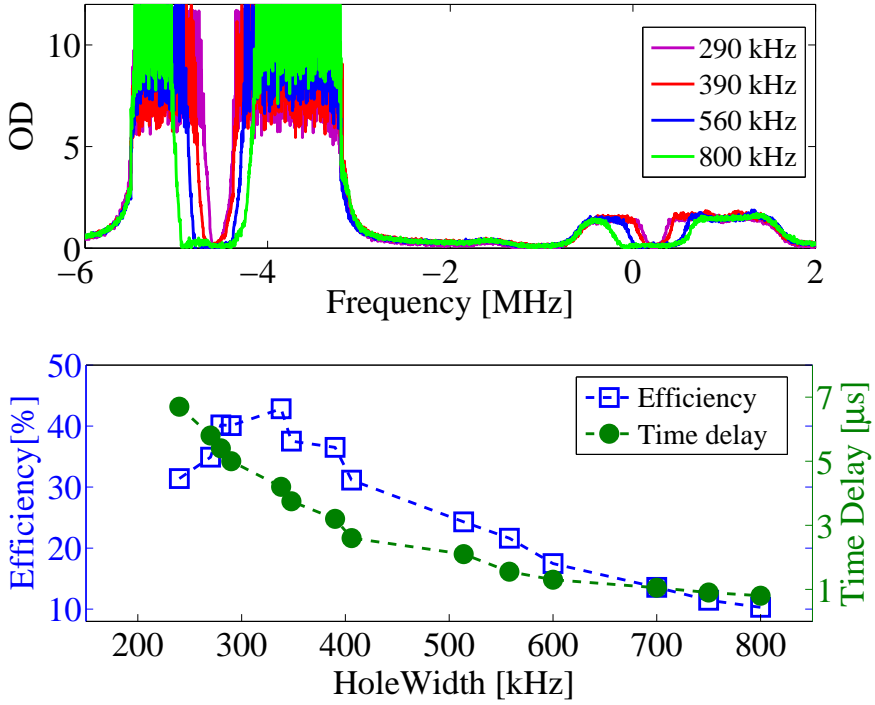


FIGURE 5.7: Above: spectral holes with different linewidth. Below: storage efficiency and time delay of the slow light as a function of spectral hole linewidth.

5.3.2 Performance at the single photon level

In order to test the suitability of our optical memory to work in the quantum regime, we insert neutral density filters in the input mode to decrease the intensity of the input pulses down to the single-photon level. For these measurements, we perform 1000 storage and retrieval trials for each memory preparation, at a rate of 5 kHz. In order to discriminate the retrieved single-photon-level signals from the noise originated by the Raman pulses, we apply several filtering strategies (see Figure 5.2) [123]. First of all, the input and the preparation/Raman modes are spatially separated with an angle of about 4° . After the memory, the retrieved signal is first steered to two single pass AOMs acting as temporal gates. Then it is sent to a second Pr:YSO crystal where a 1 MHz transparency window is created at

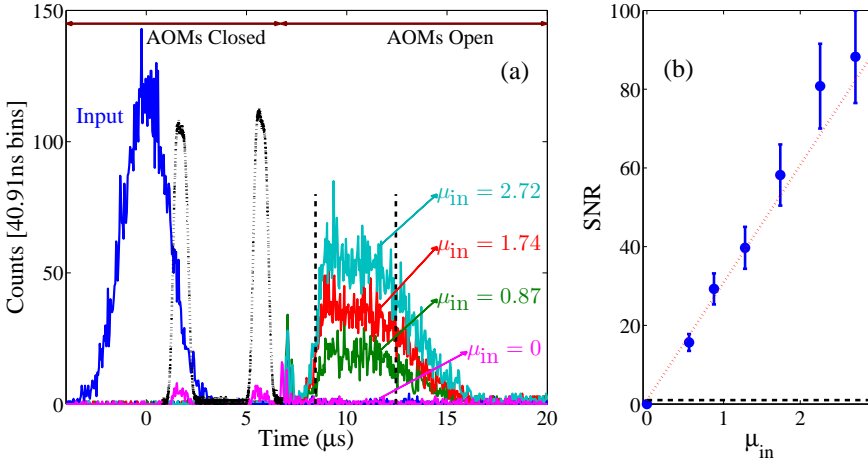


FIGURE 5.8: (a) Time histograms of the retrieved photons for different input photon numbers μ_{in} for a spectral hole with $\Delta_0 = 275$ kHz in the memory crystal. The input with $\mu_{in} = 0.87$ (blue solid trace) and the Raman pulses (black dotted trace), as measured in photon counting and from a reference photodiode, respectively, are also displayed. The detection window $\Delta t_d = 4 \mu\text{s}$ is indicated by the dashed lines about the retrieved signal. (b) SNR as a function of μ_{in} . The error bars are evaluated with Poissonian statistics. The black dashed line indicates the limit of detection $SNR = 1$. The dotted line is a linear fit of the data, from which we obtain μ_1 value of 0.030 ± 0.004 can be obtained.

the input pulse frequency [128, 129]. The fluorescence not resonant with the $\text{Pr}^{3+} \ ^3\text{H}_4(0) \rightarrow ^1\text{D}_2(0)$ transition is then suppressed with a diffraction grating. Finally, the stored and retrieved light is detected with a single-photon detector (SPD). The total transmission of the input light from the cryostat window until the SPD is around 15 %.

We record the arrival times of the photons and reconstruct the time histogram for different input photon numbers μ_{in} , as shown in Figure 5.8. From the trace with $\mu_{in} = 0$, we measure an unconditional noise floor of $(9 \pm 1) \times 10^{-3}$ photons per pulse in a detection window $\Delta t_d = 4 \mu\text{s}$. η_S is around 23 % for $\Delta t_d = 4 \mu\text{s}$ and 31 % for $\Delta t_d = 7 \mu\text{s}$. These are the highest efficiencies obtained so far for solid state spin-wave optical memories at the single-photon level. Figure 5.8(b) shows the behavior of the signal-to-noise ratio (SNR) of the retrieved photons as a function of μ_{in} .

We measure a SNR of 33 ± 4 (23 ± 3) for $\mu_{in} = 1$ when $\Delta t_d = 4 \mu s$ ($\Delta t_d = 7 \mu s$), the highest values measured so far for a single photon level solid state spin-wave memory [123, 124].

An important figure of merit for a single-photon-level optical memory is the parameter $\mu_1 = \mu_{in}/SNR$, which gives the minimum μ_{in} to reach a $SNR = 1$ for the retrieved photon. It has been shown that, in order to achieve quantum storage with an external single-photon source, a necessary condition is to have $p > \mu_1$, where p is the probability to find a single photon before the memory [123, 124]. From the slope in Figure 5.8 (b), we find $\mu_1 = 0.030 \pm 0.004$. Our system is therefore very promising for quantum light storage, provided that μs -long single photons are available. Such long photons could be created from atomic ensembles [130, 131] or single ions [132] and frequency shifted to the resonance frequency of the Pr^{3+} doped crystal by quantum frequency conversion techniques [51, 72, 133]. Shorter photons could also be stored if larger holes are prepared. However, in order to keep a sufficient separation between the second Raman pulse and the emitted photon, shorter Raman pulses should be used, which in turn will require a larger Rabi frequency. This could be achieved by increasing the Raman pulse power, or more efficiently by confining the interaction, e.g. in a waveguide configuration [134].

5.4 Discussion

The efficiency obtained in this work is mostly limited by the available optical depth and by the limited transfer efficiency. Higher optical depths will lead to higher efficiencies. Numerical simulations show that with a two-times larger optical depth $\alpha L = 17.5$, we would reach an efficiency of 55 % (assuming 100 % transfer efficiency), for a properly adjusted input pulse duration around $5 \mu s$. This shows that our protocol has a favourable scaling for an increasing optical depth. It should be also noted that further improvements could be reached by optimizing the temporal shape of the

input and control pulses and the spectral shape of the spectral hole. Further modelling is ongoing. The recent simulations show that it is possible to reach stopped light efficiency more than 50% by changing the temporal shape of the input pulse.

In our experiment, we store and retrieve single mode weak pulses. When extended to the storage of true single photons, the protocol could be exploited to demonstrate entanglement between remote crystals using the scheme proposed in [39]. Nonetheless, many applications require the storage and retrieval of photonics qubits. While our protocol is not a good candidate to store light in multiple temporal modes [135], it could be readily extended to the storage of polarization qubits [136–139] or to frequency-bin qubits [140, 141].

In this chapter, I presented the first demonstration of a light storage protocol based on stopped light in a spectral hole in a doped crystal. We achieved a storage and retrieval efficiency of around 40% in the classical regime. Thanks to a low unconditional noise floor, we stored and retrieved single-photon-level pulses with high signal-to-noise ratio. This demonstrates that the memory can work in the quantum regime, with the highest efficiency so far obtained for spin-wave solid state optical memories. These results are promising for the realization of robust, highly efficient and long-lived spin-wave solid state quantum memories.

Chapter 6

Atomic Frequency Comb

In this chapter, I discuss a well-known quantum memory technique, the atomic frequency comb (AFC) protocol. I present the results of an experiment where we stored up-converted telecom photons with the AFC protocol in the excited state of a Pr:YSO crystal. This work was published in New Journal of Physics [72]. Besides I will present the improvement on the AFC preparation which leads to higher storage efficiency and longer excited state storage time. I will also show the performance of spin-wave storage of classical pulses and weak coherent state at the single photon level. These results show the highest signal-to-noise ratio demonstrated with spin-wave AFC protocol at the single photon level.

6.1 Introduction

Storing a train of pulses, i.e. implementing the so called temporally multi-mode storage, is one of the key features which can improve the speed of quantum repeater schemes [39]. The capability of storing multiple temporal modes with a given efficiency depends on the optical depth d of the medium in many quantum memory protocols. For example, for a

fixed efficiency, the number of modes scales with d in the controlled reversible inhomogeneous broadening (CRIB) scheme and with \sqrt{d} in EIT and Raman-type memories [135]. This scaling strongly limits the number of modes that can be stored. This was the driving force for the proposal of the AFC protocol in which the temporal multi-modality does not depend on the optical depth [142].

The AFC technique proposed by Afzelius and coworkers [142] takes the inhomogeneous broadening in the solid state systems as an advantage. It is based on tailoring the profile of an optical transition as a spectral comb with periodic and highly absorptive peaks which can be created by spectral hole burning techniques described as in Chapter 2.4. The separation of the peaks, Δ , determines the storage time in the excited state, $\tau_{AFC} = 1/\Delta$ [142]. The input light is absorbed by the AFC structure and the collective atomic excitation starts to dephase. However due to the periodic frequencies the ions are then rephased which leads to a collective re-emission at $1/\Delta$ as shown in Figure 6.1. This built-in rephasing mechanism which is not dictated by any strong optical field, i.e. an optical pi-pulse in the two pulse photon echo, makes the technique suitable for single photon storage, practically noise-free. The first demonstration of the AFC protocol was also the first storage and retrieval of light fields at the single photon level in a solid state device [143]. The storage efficiency at the time was 0.5% after 250 ns storage time. In 2010, 9% efficiency at 1.5 μ s storage time [144], 35% efficiency at 800 ns storage time [145], and 25% efficiency at the single photon level at 800 ns storage time [146] have been reported. In 2013 and 2014 AFC experiments assisted with impedance matched cavity in order to increase the absorption of the input light have been demonstrated with efficiencies of 56% at 1.1 μ s, 53% at 2 μ s and 28% at 10 μ s storage times [147, 148]. In the experiment conducted in 2014, spin-wave storage efficiency of 12% was also reported [148] for spin state storage time of 5.4 μ s.

In the two-level AFC scheme, we determine the AFC storage time before

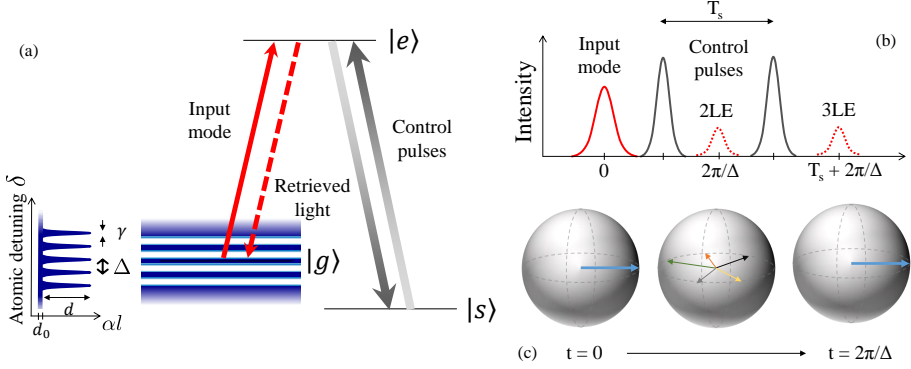


FIGURE 6.1: (a) A schematic representation of the AFC protocol where the inhomogeneous broadening is tailored with periodic peaks. An input pulse creates a coherence between $|g\rangle$ and $|e\rangle$. A control pulse transfers the coherence to the spin-state $|s\rangle$. The second control pulse applied on-demand converts the spin coherence into optical coherence back. See panel (b) for the timing. (c) Bloch sphere representation of dephasing and rephasing process.

the arrival of input photon to the crystal. We therefore speak of a pre-determined storage time. The ability of extending the storage to the spin state by applying two transfer pulses offers on-demand read-out and longer storage times thanks to the slower decoherence in the spin state. If a π -pulse resonant with the transition between the excited state and an empty spin state is applied before $1/\Delta$, the coherence can be transferred to the spin-state. A second π pulse can be applied on-demand and transfers the spin-wave back to the excited state. Then the dephasing resumes and the rephasing leads the emission of the spin-wave echo. The dephasing in the spin state can be minimized by using spin echo dynamical decoupling (DD) technique and storage times in the order of millisecond range have been reached at the single photon level [124, 149]. The three level spin-wave AFC protocol requires 3 ground states, one empty state for the storage, one for the AFC structure and an auxiliary state for the population tailored out during the AFC preparation. Among the known REID materials, Eu and Pr doped crystals can satisfy this requirement. The first spin-wave AFC experiment has been reported in 2010 with Pr:YSO crystal [126]. 2

years later the first spin-wave AFC experiment with Eu^{+3} has been published [150]. The first demonstrations of spin-wave AFC experiments at the single photon level have been reported in 2015 by our group and the Geneva group [123, 124].

The temporal multi-mode capacity of the protocol is limited by the number of AFC peaks. The first demonstration was realized with $\text{Nd}^{3+}:\text{YVO}_4$ crystal in the first demonstration of the AFC protocol [151]. Later, thanks to large splitting between the ground states, a 100 MHz wide AFC could be tailored to store a train of 64 single photon level input pulses in the excited state [152]. The storage of 1060 temporal mode has been demonstrated in the excited state of a $\text{Tm}^{3+}:\text{YAG}$ crystal in the classical regime [153]. However the preparation procedure limits the achievable efficiency. The storage in the spin state demands more complex techniques due to the fact that the maximal width of the comb is limited by the spacing between hyperfine states. However storage and retrieval of 50 modes has been realized with $\text{Eu}^{3+}:\text{Y}_2\text{SiO}_5$ crystal [154]. Besides these demonstrations of highly multi-mode storage, our group demonstrated the first quantum memory for time-bin qubits, with on-demand read-out of the stored quantum information [123]. In the experiment, two single photon level input pulses were sent to the $\text{Pr}:\text{YSO}$ memory where the coherence was transferred to the spin state by two partial write pulses whose separation in time is same as the separation of the inputs. We varied the relative phases of both the inputs and the write pulses in order to compute the fidelity of the storage.

The AFC storage was also extended to the polarization degree of freedom. Three groups, including ours, have reported the storage and retrieval of arbitrary polarization states of light from solid-state quantum memories [136–138]. While neither the materials ($\text{Pr}^{3+}:\text{Y}_2\text{SiO}_5$, $\text{Nd}^{3+}:\text{Y}_2\text{SiO}_5$, $\text{Nd}^{3+}:\text{YVO}_4$) nor the strategies are the same, the fidelities obtained are around 95% exceeding the maximum value achievable by a classical memory. The experiment also extended to the spin-wave storage of polarization qubits in 2016 [139].

The storage of correlated photons is an important step toward the implementation of quantum information networks. In our group we first demonstrated a quantum storage of heralded single photons from an ultra narrow-band source in the excited state of a Pr:YSO crystal [74]. The heralding photon emitted from the source is at telecom wavelength while the signal photon is resonant with our crystal. This experiment has been recently extended to the spin-wave storage where correlations between single telecom photons and single spin excitation in the crystal have been demonstrated [155].

One of the fundamental requirement of quantum memories in quantum repeater schemes is the entanglement storage. The storage of a single photon emitted by a entangled photon pair source has been demonstrated by two groups in 2011 [156, 157]. These experiments were followed by the demonstration of heralded quantum entanglement between two crystals [158]. Quantum storage of three-dimensional orbital-angular-momentum entanglement has also been demonstrated by using the AFC protocol [159].

Another important experiment using the AFC protocol is the quantum teleportation of the polarization state of a telecom wavelength photon onto the state of a solid-state quantum memory [160]. In the experiment the combined distance traveled by both telecom wavelength photons was 25 km in standard optical fiber which demonstrates the long-distance capability of the approach. The same group also reported an experimental observation of heralded quantum entanglement between two separate crystals [158].

6.2 Theoretical background

In this part I benefited from the original proposal [142], from a book chapter [161] and also from M. Gündoğan's PhD thesis [162].

A single photon field can be completely absorbed by an AFC if its bandwidth is larger than periodicity Δ . The atomic state which consists of N

atoms can be described by $\sum_j c_j |g_1 \cdots e_j \cdots g_N\rangle$ as a collective Dicke state where the amplitudes c_n depend on the detuning and spatial position of the j^{th} atom. After the excitation, each atom acquires a particular phase $e^{i\delta_j t}$, where δ_j is the detuning of the j^{th} excited atom, hence the state dephases into a non-collective one

$$\sum_{n=1}^N c_n e^{i\delta_j t} e^{ikz_j} |g_1 \cdots e_j \cdots g_N\rangle \quad (6.1)$$

where z_j is the position of the j^{th} atom and k is the wave number of the light field. We can assume $\delta_j = m_j \Delta$ due to the periodicity of the AFC peaks. Therefore the non-collective state returns into the collective state again after a time $1/\Delta$ and this results in a collective re-emission.

The AFC can be characterized by Δ , the Gaussian peak width $\tilde{\gamma}$ and the overall comb with Γ . By using these parameters, the spectral distribution of the atoms in the AFC can be described as

$$e^{-\delta^2/(2\Gamma^2)} \sum_{j=-\infty}^{\infty} e^{-(\delta-j\Delta)^2/(2\tilde{\gamma}^2)} \quad (6.2)$$

In order to find a mathematical expression of the re-emitted field, we can plug the atomic distribution into the Maxwell-Bloch equations and solve it analytically. The ratio of intensity of the output field to the input field gives the efficiency of the storage and reads as

$$\eta_{AFC} \approx \tilde{d}^2 e^{-7/F^2} e^{-\tilde{d}e^{-d_0}} \quad (6.3)$$

where $F = \Delta/\gamma$ is the finesse of the comb and $\gamma = \sqrt{8 \ln 2} \tilde{\gamma}$ is the FWHM of the comb peak, $\tilde{d} = d/F$ is the effective optical depth that the input pulse experiences where d is the optical depth (OD) of the AFC, and d_0 is the background OD. The equation 6.3 is for the 2 level storage and for the emission in the forward direction. The emission in the forward direction is limited to 54% due to the reabsorption of the emitted light in the medium. However it is possible to reach unity efficiency by applying

counter-propagating control pulses which transfer the coherence back and forth between the excited and a spin state and force the backward emission due to the phase matching condition. The storage in the spin level is called spin-wave (also called 3-level) AFC storage and provides on-demand read-out, independent of the direction of the emission. In the backward emission, even though the re-absorption still exists, a constructive interference effect between all possible emission paths results in a possible unity storage efficiency for the optimum F value at high OD values. If we assume that control pulses are π pulses infinitely short in time and there is no decoherence in the spin state, then the backward AFC efficiency can be written as

$$\eta_{BW-AFC} \approx (1 - e^{-d/F})^2 e^{-7/F^2} \quad (6.4)$$

In the spin-wave AFC experiments, we have to consider the transfer efficiency of each control pulse η_T and also the decoherence in the spin state of the ensemble η_{Dec} . Therefore the total efficiency is given by

$$\eta_{SW} = \eta_{AFC} \times \eta_T^2 \times \eta_{Dec} \quad (6.5)$$

It is worth to note that the square peaks instead of Gaussian peaks provide higher efficiency at low and intermediate ODs for the optimum F values which is in this case $F = \pi/\arctan(2\pi/d)$ [148, 163]. The AFC efficiency is now described by

$$\eta_{AFC} = \tilde{d}^2 e^{-\tilde{d}} \text{sinc}^2(\pi/F) \quad (6.6)$$

However the maximum η_{AFC} in the forward direction is still limited to 54%.

6.3 Storage of up-converted telecom photons

6.3.1 Motivation

Photons at telecommunication wavelengths are to be the flying qubits in long distance quantum communication hence quantum memories operating in this frequency range are of great interest. However most of the atomic systems perform at visible range. One of the exception is erbium (Er) doped systems. Unfortunately this material suffers from low efficiency for memories based on spectral tailoring of the inhomogeneous profile due to the poor optical pumping dynamics [164]. Other protocols such as Revival of Silenced Echo (ROSE) derived from two-pulse echo technique can offer promising efficiencies because they do not rely on optical pumping. Memory efficiency of 40% was observed with strong input pulses by using the ROSE protocol [165]. However the experiments with the ROSE protocol have stayed limited to input weak coherent states of 14 photons per pulse, due to the noise created by the strong control pulses. Spectral filtering is not possible in two level systems like Er doped solids.

2 years after our experiment, long coherence times and efficient optical pumping in $^{167}\text{Er}:\text{YSO}$ have been demonstrated in strong magnetic field [166], making this material very promising for quantum memory applications.

An alternative approach would be quantum frequency conversion via non-linear processes as an interface between a memory and telecom wavelengths. Back in the days of our experiment, only two experiments had been reported following this strategy [51, 133]. Both were realized with emissive quantum memories by using the DLCZ scheme and showed the preservation of non-classical nature of the pairs after the conversion.

In this experiment, we convert single photon level telecom photons from 1570 nm to 606 nm in a nonlinear waveguide via frequency up conversion in order to interface with our $\text{Pr}:\text{YSO}$ memory. We store the up-converted

light for up to $\tau_{AFC} = 10 \mu s$ in the excited state with the two level AFC scheme. The maximum overall efficiency that we reach is $1.9 \pm 0.2\%$ at $\tau_{AFC} = 1.6 \mu s$, the highest reported efficiency among the absorptive telecom optical memories at the single photon level at the time [72].

6.3.2 Experimental Setup

We have two main parts in this experiment: the quantum frequency converter (QFC) and our Pr:YSO memory. The experiment was realized together with another PhD student, Nicolas Maring. While he was in charge of the QFC setup, I was responsible from the quantum memory part. We used the AFC protocol for the storage and here I focus mostly on the memory part of the experiment for the sake of the compactness of the chapter. More details on the QFC part can be found in the paper [72].

We use two Toptica external cavity diode lasers (ECDL) to create the light at 606 nm as describe in Chapter 4.1.1. We split the output of the lasers into two and feed two waveguides, one for creating the preparation light and the other is for the QFC. The maximum pump power at the input of the QFC waveguide is 600 mW. We have an additional Keopsys erbium-doped fiber amplifier to have around 1W of 1570 nm. A 95:5 fiber beam splitter divides 1570 nm light where 95% is used to create 606nm preparation light. We obtain 2 mW of preparation light power.

In the QFC part, the 1570 nm light is attenuated to the single photon level by optical density filters and then coupled with the 987 nm pump light into a 2.6 cm long PPKTP nonlinear waveguide. We employ a single pass AOM in the pump mode during the detection of the AFC echo for temporal filtering from the noise induced by the strong pump light. Turning the AOM on reduces the light passing through the 0^{th} mode of the AOM and with the distorted mode shape we reach around one order of

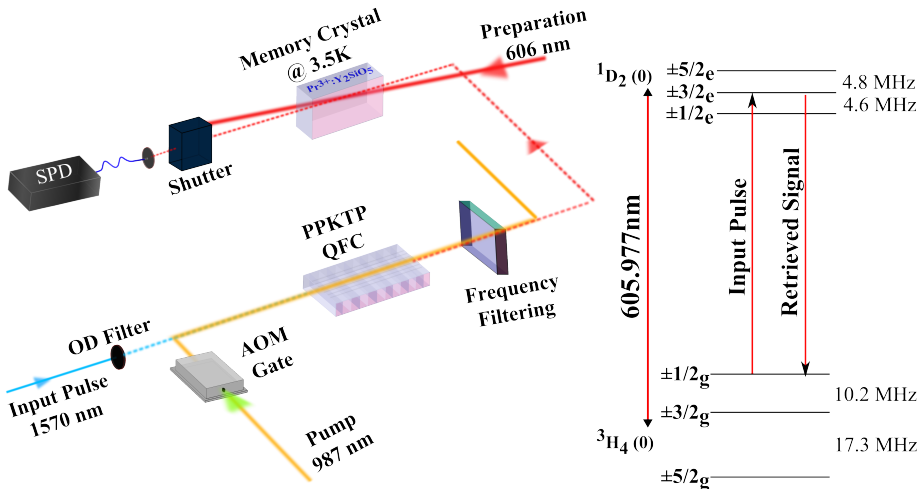


FIGURE 6.2: Left: The experimental setup. Input telecom light at 1570 nm is reduced to single photon level using optical density filters. Both input photons and pump light at 987 nm are coupled into the periodically-poled potassium titanyl phosphate (PPKTP) nonlinear QFC waveguide. We prepare the AFC in the crystal with the preparation mode. The AFC echo is emitted in the forward mode and collected with a fiber coupled single photon detector (SPD). We also employ a shutter to protect the SPD from the scattered light of the strong preparation pulses. Right: the relevant level scheme of Pr:YSO crystal.

magnitude reduction in the up-converted light. There is also a spectral filtering stage which consists of a diffraction grating (Thorlabs, GR13-1205) and an etalon with finesse 6 and linewidth 10 GHz.

The Pr:YSO memory crystal has a length of 5 mm and a doping concentration of 0.05%. We place it inside the Montana cryostation that is already introduced in Chapter 4. The PDH frequency locking system is also already introduced in the same chapter.

We start to prepare the AFC structure as described in Chapter 2.4.1. Later by spectral hole burning technique, discussed in Chapter 2.4, we create periodic, comb like absorptive features, as shown in Figure 6.3, by moving the frequency of the laser by a fixed amount Δ on the single class

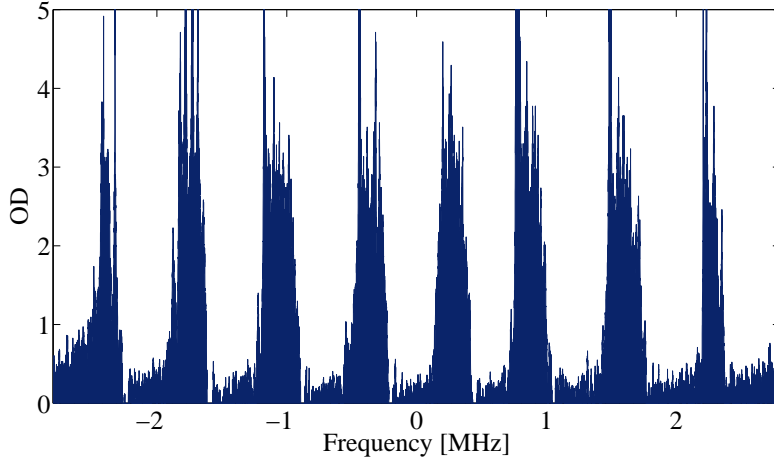


FIGURE 6.3: An example of the atomic frequency comb for $\Delta = 700$ kHz. The OD values are limited due to the dynamic range of the detector.

absorptive feature. In total, the preparation procedure takes around 200 ms.

Besides the temporal filtering with the single pass AOM in the pump mode, we also apply spatial and spectral filtering strategies. The preparation mode has an angle of around 4° with the single photon level input mode to provide spatial filtering of the strong preparation light. For the spectral filtering, we employ a diffraction grating to remove the the pump light from the converted photons and also an etalon with finesse of 6 and linewidth of 10 GHz to reduce the effect of Raman scattering and spurious SPDC noise.

We detect the single photon level signal with a PicoQuant (Tau SPAD-20) SPD. It has a measured 10 Hz dark count rate and 60% detection efficiency at 606 nm. A shutter protects the SPD from scattered light of the preparation pulses and a band pass filter of 14 nm centered at 600 nm filters out the spurious light.

We perform start-stop measurement with the Signadyne TDC module, described in Chapter 4. For each AFC preparation, we send 6000 input telecom pulses.

6.3.3 Results

Here I will first summarize the performance of the QFC device without the memory. Then I will present the results of the storage. More details on the QFC performance can be found in the paper [72].

We characterize the QFC with a mean input photon (at 1570 nm) number of 1, $\mu_{in} = 1$, and with the pulse FWHM of 140 ns. The maximum measured QFC device efficiency η_{dev} is 21 ± 1 % at 252 mW pump power. However the signal-to-noise ratio (SNR) at this pump power is 2.07 ± 0.02 due to the noise created by the high pump power.

We realize the AFC storage characterization at 141 mW pump power which provides 15.2 ± 0.8 % device efficiency and SNR of 3.85 ± 0.04 for $\mu_{in} = 1$ after the QFC. While keeping the pump power constant we measure SNR as a function of mean input telecom photon number. In Figure 6.4 I present a histogram of a $\tau_{AFC} = 1.6$ μ s storage where $\mu_{in} = 0.1$. The orange plot shows the input photons which pass through the transparency window prepared in the memory crystal, taken as the input of the AFC. The high noise level is due to the QFC pump. By turning the gate AOM on at 1 μ s, we can dramatically decrease the noise and can observe the AFC echo. The gate AOM is on for 5 μ s. We characterize the SNR value for three cases: only QFC, AFC input and AFC echo. The characteristic value we choose to compare for the three cases is the minimum input photon number required to achieve a signal to noise ratio of 1, the so-called μ_1 . We fit the data with a linear function which is forced to pass through zero. The fit of the QFC measurement data gives SNR of 1 at μ_{in} of 0.37 ± 0.02 . A noise window of 2.36 μ s is chosen to be centered at 7.48 μ s, then it is normalized to the 400 ns integration window of the input. By taking the same noise and signal windows, we measure $\mu_1 = 0.23 \pm 0.004$ for the AFC input. The improvement in the μ_1 is attributed to the absorption of the noise by the 6-12 GHz inhomogeneous profile of the memory crystal. In the storage case, we measure $\mu_1 = 1.38 \pm 0.03 \times 10^{-3}$. Our strategy of gating the pump light with an AOM after the input light but before the

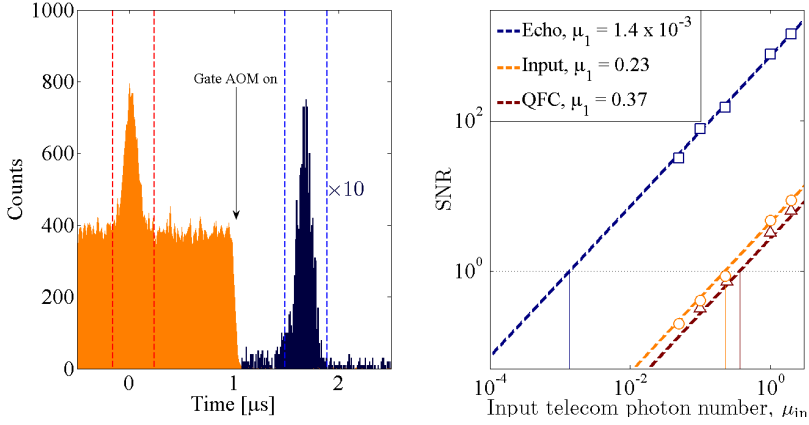


FIGURE 6.4: On the left panel, a histogram plot of an input (orange) pulse and the corresponding AFC echo (dark blue) at $\tau_{AFC} = 1.6 \mu\text{s}$ are shown. The AFC echo histogram is 10 times magnified. We turn the gate AOM on at $1 \mu\text{s}$. The dashed lines are the integration windows which are 400 ns wide. The bin size of the histogram is 10.24 ns. Right panel: SNR values of AFC echo (blue squares), AFC input (orange circles) and QFC output (red triangles) as a function of input telecom photon number for the pump power of 144 mW.

echo results in a 270-fold improvement compared to the QFC only case, even though the AFC echo efficiency, η_{AFC} , is measured to be $19.8 \pm 0.1 \%$ at $\tau_{AFC} = 1.6 \mu\text{s}$. The 4 MHz AFC memory is narrow band compared to the noise hence the storage of the noise photons in the AFC become negligible. The total device efficiency before the QFC until detection after storage is measured to be $\eta_{total} = 1.55 \pm 0.02 \%$.

Another characterization of the storage process is measuring the SNR and efficiency values at different storage times while keeping the pump power of 144 mW and μ_{in} of 1 constant. We increased the input photon duration to 560 ns and the integration window to 1200 ns. I present the results in Figure 6.5. At the time of the experiment, we could keep the AFC efficiency around 10% until around $5 \mu\text{s}$. Achieving high storage efficiencies at long AFC storage times requires precise control over the AFC peak width γ and separation Δ , i.e. on the finesse of the AFC. The line-width of the laser is a dominant factor in this case. Alternative AFC preparation methods mentioned in the following sections can be used to circumvent this

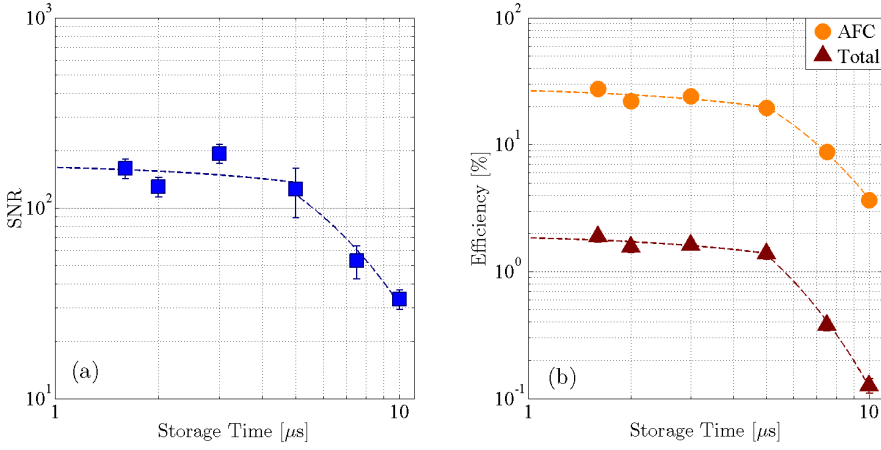


FIGURE 6.5: (a) Signal to noise ratio and (b) echo and total efficiency versus storage time for $\mu_{in} = 1$ telecom photons per 560 ns pulse (excluding the data point at 10 μs where $\mu_{in} = 0.4$ is used with the SNR normalized accordingly). The SNR and efficiencies stay relatively flat for storage times up to and including 5 μs . For these storage times, the total efficiency is always above 1% and the SNR is always above 100 which would correspond to a μ_1 lower than 10^{-2} . The efficiency drops below 10% at storage times longer than 7.5 μs , limited by the tailoring of the AFC. Dashed lines in both figures are used to guide the eye. Error-bars (often smaller than the symbol) represent one standard deviation.

limitation [154]. Here, we reach η_{AFC} of 27.4% at $\tau_{AFC} = 1.6 \mu\text{s}$ while the total efficiency including the QFC and the optical losses is 1.9 ± 0.2 %. The increase in the efficiency is due to the fact that the longer input pulse matches better with the bandwidth of the AFC structure. However we loose in SNR (now 162 ± 19) partly because of the larger integration window thus including more noise and partly due to the less effective gate AOM for this set of measurement. The SNR and efficiency values start to decay after 5 μs τ_{AFC} due to the poor AFC finesse.

6.4 Improved performances for excited state storage

The efficiency of a two level AFC echo is limited to 54% for the optimum finesse. Therefore it is crucial to have the best control over the finesse in order to reach high efficiency at different storage times. Long storage times require narrow Δ values which can be hard to obtain even with narrow linewidth lasers. For example 10 μs excited state storage time means creating Δ of 100 kHz. Different AFC preparation strategies have been explored over the years to reach high efficiency values at long storage times. In the heralded single photon storage paper we published in 2014 [74], we prepared the AFC structure by directly burning spectral holes outside of the transparency window which means that the AFC consisted of many antiholes burned back individually. The η_{AFC} values we had were around 7% at 2 μs and 1% at 4 μs storage time. Later we switched to another approach which has already been described in this chapter. By creating a wide absorptive feature and then tailoring the AFC by creating spectral holes provide us better control over the finesse and η_{AFC} values around 10% until 5 μs storage time. However any direct comparison of the η_{AFC} values between two approaches may not be fair because the first experiment was realized in a different setup with a Oxford Inst. cryostat which suffers more from vibrations and provides less stable results. Later we switched to the 606 nm SHG laser, increased the waist of the preparation mode from 120 μm to 300 μm and also followed another strategy to prepare the AFC memory. The idea, first proposed by Bonarota *et. al.* [163], and later optimized by Jobez *et. al.* [154], is to create a waveform whose Fourier transform gives the desired AFC structure with the optimum finesse. As discussed in [163] and in Chapter 6, the optimum AFC peak shape to maximize the efficiency is square. We prepare a waveform of a square AFC structure by considering the OD of the crystal and the excited state storage time. The Fourier transform of the desired AFC gives the temporal waveform of the pulse train that we use to shape the single

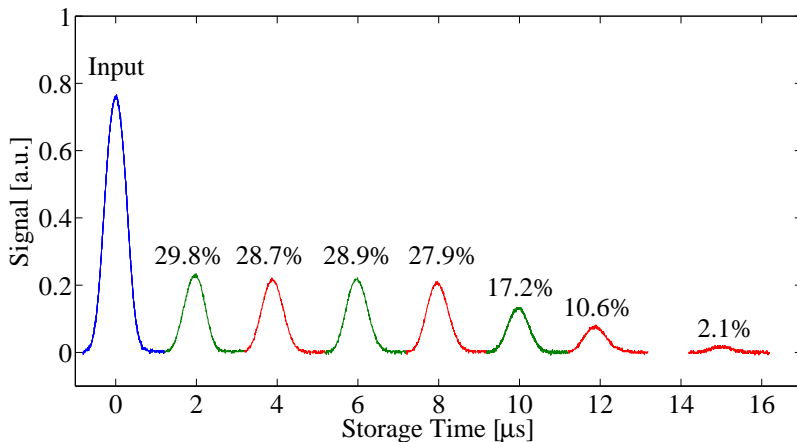


FIGURE 6.6: Two level AFC storage traces and efficiency values at different storage times.

class absorption feature [154]. While we burn the AFC at the $1/2_g - 3/2_e$ transition frequency, some ions are also coherently driven back to the $3/2_g$ state. Thus, we proceed by sending cleaning pulses at the frequency of the $3/2_g - 3/2_e$ transition. The advantage of this approach is that the finesse becomes less dependent on the laser linewidth since we do not burn the teeth of the comb one by one. More details about this strategy can be found in Jobez *et. al.* [154] and Seri *et. al.* [155]. In Figure 6.6 we show almost constant η_{AFC} values of around 28% up to 8 μs storage time, and still more than 10% of η_{AFC} at 12 μs storage time. These data were taken in March 2016 and present our progress on the control of the AFC during my PhD studies.

6.5 Spin-wave AFC storage

On-demand retrieval of stored light is of great importance for the tasks where quantum memories are employed for the synchronization of the system. The two level AFC scheme can provide only a pre-programmed delay limited by the excited state coherence time of the memory. On the other

hand, if we can transfer the population to a spin state where the coherence time is much longer, we can read-out the spin coherence at the desired time. The full AFC scheme (also called spin-wave or three level AFC) is capable of this kind of storage as already described in the beginning of the chapter. In this section, I will briefly discuss spin-wave AFC results which are not reported elsewhere. To our knowledge they represent the highest spin-wave AFC efficiencies both with classical light and single-photon level weak coherent state. These data were taken in January 2015.

The experimental setup and the relevant level structure are the same as in Figure 5.2. The beginning of the memory preparation is described in Chapter 2.4.1 and the AFC preparation is the same as in the previous section 6.3 such that we create the AFC by hole burning in single class absorptive feature. In this experiment we prepare a 3 MHz absorptive feature in the $1/2_e - 3/2_g$ transition. More detailed description about the AFC preparation can be found in Gündoğan *et al.* [123].

In this experiment, we prepare the AFC structure for 5 μs excited state storage time. Figure 6.7 shows the temporal pulse sequence both in classical regime and with weak coherent states. The input pulse has a FWHM of 1 μs while the control pulses are 1.2 μs . The first control pulse is applied just 500 ns after the input pulse. The spin-wave storage time T_s is 6 μs therefore the total storage time is 11 μs . The spin-wave echo appears around 4.5 μs after the second control pulse, which becomes important in the photon counting regime where the main noise source is the strong second control pulse. In the classical regime, we reach η_{AFC} of 24.5% and spin-wave efficiency η_{SW} of 14% which is the highest demonstrated η_{SW} with the AFC protocol to our knowledge. In a recent cavity enhanced experiment, Jobez *et. al.*, reached an spin-wave efficiency of 12 % [148]. The control pulse transfer efficiency is around 81% and we calculate the coherence in the spin state η_C for 6 μs storage as 87%. In the measurement of weak coherent state, we send 1000 pulses for each AFC preparation and we repeat the process 200 times. We observe η_{AFC} of around 14%. We

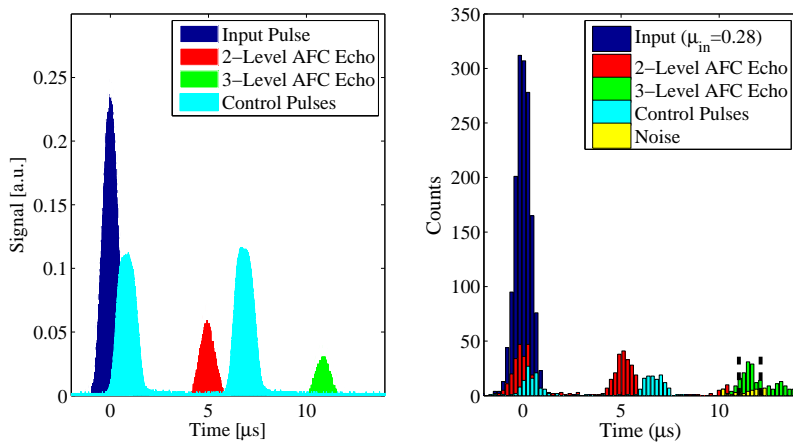


FIGURE 6.7: The spin-wave AFC memory schemes with classical input pulse on the left panel and with weak coherent input pulses ($\mu_{in}=0.280$) on the right panel. τ_{AFC} is $5 \mu s$ and $T_s = 6 \mu s$ in both cases. The input pulses, whose polarization is orthogonal to the optical D_2 axis of the crystal, are sent through a 15 MHz transparency window. The control pulses in the classical measurement are detected by another photo diode. However in the weak coherent state measurement we could observe their leakage into the detection mode.

attribute the decrease to the deterioration of the AFC in time while sending 1000 pulses and it is also possible that some of the pulses might be sent in the noisy part of the cryo-cycle, discussed in Chapter 4. We reach η_{SW} of around 8.5% which leads to μ_1 of 0.058 ± 0.014 for the integration window of $1.1 \mu s$ with the unconditional noise level of 7.5×10^{-4} per μs . If we narrow the window to 700 ns, we loose in the η_{SW} which decreases to 7% although the μ_1 value improved to 0.035 ± 0.011 , which is the best single photon level performance to our knowledge for AFC spin-wave memories, and comparable to the results with the SHoMe protocol presented in Chapter 5.

6.6 Discussion and conclusion

The experimental results that I presented in the section 6.3 show how efficient AFC memories can be used to store single photon level light. As

a “telecom” memory, these results outperformed previous realizations of absorptive telecom memories at the single-photon-level at the time [167, 168]. In this particular experiment, with the strategy that we used to detect converted and stored photons, we showed that the AFC can be used as a narrowband filter which could improve the SNR around 2 orders of magnitude compared to the only QFC output.

I also presented the improvement in 2-level AFC storage efficiency due to optimized comb preparation, where we could reach efficiencies up to 30%, close to the theoretical prediction of around 40%. Finally, I described our capability of on-demand storage with the 3 level AFC protocol. These results show the highest spin-wave AFC efficiencies and the best on-demand performance both in single photon level and in the classical regime. The ability to store single photon level light on-demand with the AFC protocol will be crucial in the next chapter.

In order to increase the η_{AFC} , hence the η_{SW} , we may follow a few approaches in the future. The first and the straight forward one might be employing a longer crystal. This increases the optical depth without introducing more ion-ion interaction which decreases the coherence time as increasing the doping concentration would do. Another strategy would be tailoring the AFC structure better in order to obtain the optimum finesse value to realize the highest possible η_{AFC} for the given optical depth.

Another possibility is to include the crystal in an impedance matched cavity [169, 170] as was shown in [147, 148].

Chapter 7

A solid-state multi-mode emissive quantum memory with DLCZ-AFC

In this chapter, I present an emissive quantum memory protocol. It combines two different schemes, namely the AFC scheme and the DLCZ scheme to take the advantage of both schemes, i.e. creation of single spin excitation in the DLCZ and the multimodality of the AFC. The protocol can also be understood as a temporal multi-mode photon pair source with an embedded quantum memory. The idea was proposed by Sekatski and his coworkers in 2011 [171]. Here I present the background, the experimental details and the results of this first demonstration which was published in Physical Review Letters as an Editor suggestion [172] and also featured in Physics as a ViewPoint by J. Nunn [173]. A similar experiment from the Geneva group was published back to back [174]. Many parts in this chapter have been taken from our publication.

7.1 Introduction

Most of the experiments to date in REIDS have demonstrated absorptive (read-write) quantum memories, where external quantum states of light are mapped on the QM [74, 156, 157, 175]. This process requires the generation of single or entangled photons by an external source with demanding spectral properties to achieve strong interactions between the quantum light and the QM [74, 176]. In 2001, Duan, Lukin, Cirac, and Zoller (DLCZ) proposed an alternative scheme combining a correlated photon-pair source and a quantum memory in atomic gases [36], which has enabled fast progress towards elementary quantum networks [44–47, 114, 115]. It is based on the creation of a single collective spin excitation (spin-wave) via off-resonant spontaneous Raman scattering, heralded by the detection of a Stokes photon. After a programmable storage time, the spin-wave can be transferred with high efficiency into a single anti-Stokes photon using a resonant read pulse. Since the first demonstration [42], impressive progress has been realized, including the demonstration of elementary quantum networks [44, 46, 47, 114–116], entanglement between four atomic ensembles [45], and long-lived quantum memories [51, 177]. These demonstrations have made cold atomic ensembles one of the most advanced systems to date for quantum networks applications. The DLCZ scheme has also been implemented with phonons in diamond [178] and in a mechanical resonator [179].

Schemes to combine QMs and photon pair sources in rare-earth doped solid-state ensembles have also been proposed [171, 180]. REIDS have much weaker optical transitions than atomic gases (their dipole moments is 2-3 orders of magnitude lower than alkali atoms), making off-resonant excitation challenging [181]. A solution is to excite atoms on resonance to achieve stronger interaction. However, this leads to fast dephasing due to inhomogeneous broadening of the optical transition in the crystal, making a rephasing mechanism mandatory to recover the collective emission of the second photon [171, 180]. Early demonstration of time-separated

correlations between crystal and light field have been reported [129, 182] using the scheme of Ref. [180], including entanglement between a light field and a solid-state spin-wave QM [183]. In these experiments, quantum correlations were demonstrated in the continuous variable regime using heterodyne detection techniques.

The last couple of years of my PhD have been devoted to demonstrate a temporally multi-mode DLCZ-like scheme [171] in the photon counting regime in a rare-earth doped quantum memory. The work described in last sections of Chapter 6 on the improvement of the rephasing protocol can also be included in this effort.

In this chapter, I present the first demonstration of another quantum memory protocol which is used to generate pairs of correlated photons with a controllable delay. We demonstrate quantum correlation between the photons for delays up to 20 μs . The photon pairs are created through spin-wave storage, effectively generating quantum correlations between single photons and single collective spin-waves in the crystal. Combining the DLCZ scheme with rephasing techniques allows us to demonstrate the creation of spin-waves into multiple temporal modes. The use of photon counting detection enabling discrete variable encoding, combined with the high quantum correlation demonstrated, makes our source of photon pairs with embedded quantum memory directly usable for quantum repeater schemes.

7.2 Theoretical background

In this part I benefited from the DLCZ and the DLCZ-AFC proposals [36, 171] and also from B. Albrecht's PhD thesis [162].

The DLCZ scheme [36] requires a three level λ -type energy level configuration, as shown in Figure 7.1. The spin states $|g\rangle$ and $|s\rangle$ should be long lived state and $|e\rangle$ is the excited state. Initially, all atoms are in the state

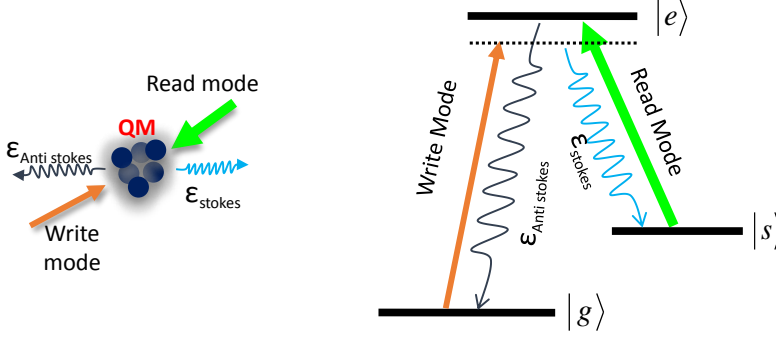


FIGURE 7.1: A three level λ -type energy level configuration in DLCZ scheme.

$|g\rangle$, in a collective state $|G\rangle = |g_1, \dots, g_N\rangle$. A short write pulse is applied off-resonantly to the $|g\rangle - |e\rangle$ transition and it can result with a transfer of a single atom to the $|s\rangle$ state and an emission of a Stokes photon via Raman scattering. The emitted photons and the excitations are correlated such that

$$S = \frac{1}{\sqrt{N}} \sum_{j=1}^N e^{-i(\mathbf{k}_W - \mathbf{k}_S) \cdot \mathbf{r}_j} |g\rangle_j \langle s| \quad (7.1)$$

where \mathbf{r}_j is the position of the j^{th} atom, \mathbf{k}_W is the wave vector of the write pulse and \mathbf{k}_S is the wave vector of the Stokes photon. Even though the Stokes photon emission is isotropic, we are only interested in a single spatial mode where we collect and detect them. After detecting a single Stokes photon which heralds a single spin excitation (a spin-wave), the state of the ensemble can be written as

$$|\psi(0)\rangle = S^\dagger |G\rangle = \frac{1}{\sqrt{N}} \sum_{j=1}^N e^{-i(\mathbf{k}_W - \mathbf{k}_S) \cdot \mathbf{r}_j} |g_1 \dots s_j \dots g_N\rangle \quad (7.2)$$

In the experiments, we introduce a small angle between the write mode and the Stokes mode in order to spatially filter out the write and read

modes from the Stokes and anti-Stokes photons detection modes.

The joint state of the light and the matter system is a two-mode squeezed state and can be described by

$$|\phi\rangle = \sqrt{1-p} \sum_{n=1}^{\infty} p^{n/2} \frac{(a^\dagger S^\dagger)^n}{n!} |0\rangle_s |G\rangle \quad (7.3)$$

where p is the probability to create one Stokes photon, a^\dagger is the Stokes photon creation operator, and $|0\rangle_s$ is the vacuum state. After a storage time t_s we can map the single spin-wave into an anti-Stokes photon by applying a read pulse with a wavevector k_R . The spatial emission mode of the anti-Stokes photon is determined the phase-matching condition $k_{as} = k_W + k_R - k_S$. After the emission of the anti-Stokes photon, the state of the pair can be written as

$$|\varphi\rangle = \sqrt{1-p}(|0_s 0_{as}\rangle) + \sqrt{p}(|1_s 1_{as}\rangle) + p|2_s 2_{as}\rangle + O(p^{3/2}) \quad (7.4)$$

At high p values, it becomes possible to create multiple spin-waves which would decrease the photon pair correlation. Therefore in the experiments, we adjust the write pulse power in order to have p values lower than 1%.

In the DLCZ-AFC protocol, the origin of the Stokes photon is spontaneous emission instead the Raman scattering because the excitation of the $|g\rangle - |e\rangle$ transition is resonant as shown in Figure 7.2. T_s (T_{as}) is the time separation between a Stokes (anti-Stokes) photon and the write (read) pulse. T is the width of the Stokes detection window. The write pulse is resonant with the AFC with a storage time of τ_{AFC} and the Stokes photos are detected 1.4 μs after the write pulse. The Stokes are emitted in the whole solid angle, but we only collect the Stokes field backward at an angle of $\sim 4^\circ$ with respect to the write mode. Then we unconditionally send strong read pulses. The write and read pulses are counter-propagating, therefore, due to the phase matching condition ($\vec{k}_{as} = \vec{k}_w + \vec{k}_r - \vec{k}_s$) and collective interference, the anti-Stokes photons are emitted counter-propagating with respect to the detected Stokes photon.

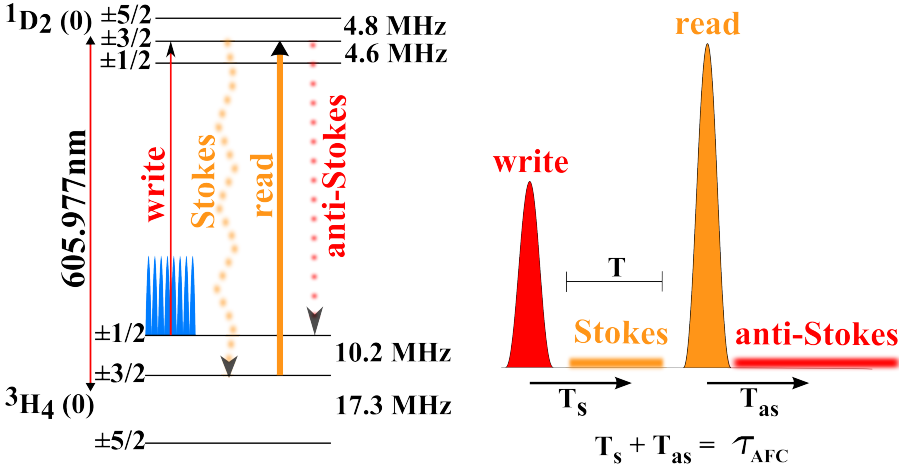


FIGURE 7.2: Left panel: hyperfine splitting of the first sub-levels (0) of the ground $^3\text{H}_4$ and the excited $^1\text{D}_2$ manifolds of Pr^{3+} in YSO. The AFC structure (blue comb) is prepared with the read mode. Right panel: temporal pulse sequence.

The Stokes photon that heralds a single-spin excitation is emitted from the ions which have already spent a time T_S in the excited state. After a storage time t_s in the spin state, the read pulse then transfers the spin excitation from the spin-state back to the excited state. At that moment, the phase evolution in the excited state resumes, and the correlated anti-Stokes photon will be emitted at time T_{aS} after the read pulse, such that $T_S + T_{aS} = \tau_{\text{AFC}}$.

If we assume that $|g\rangle - |e\rangle$ and $|s\rangle - |e\rangle$ transitions have the same dipole moment and the optical depth of the ensemble is large enough to obtain high read-out efficiency, p can be reduced to [171]

$$p \approx \theta_0^2 \quad (7.5)$$

where θ_0 , the area of the write pulse at the entrance of the ensemble, is equal to $1/2 \int ds \Omega_W(s)$. In the same conditions, the read out efficiency is described by [171]

$$(1 - e^{-(\alpha L/F)\sqrt{\pi/(4\ln 2)}})e^{-\pi^2/(2\ln(2)F^2)} \quad (7.6)$$

where αL is the optical depth of the ensemble and F is the finesse of the AFC. If we assume that the spontaneous emission during the anti-Stokes detection is the dominant noise contribution in the system, in the same conditions above, the signal-to-noise ratio can be deduced to [171]

$$\mathfrak{R} \geq \frac{2}{p}. \quad (7.7)$$

7.3 Experiment

The memory crystal, a 5 mm long, 0.05% doped, $\text{Pr}^{3+}:\text{YSO}$, is hosted in a Montana Cryostation cooled down to 3.5 K, see Figure 7.3. The write and read pulses are counter-propagating. Their polarization is rotated along the D_2 crystal axis in order to maximize the absorption. Narrow-band filters at 600 nm (width 10 nm) are placed on both Stokes and anti-Stokes modes. The Stokes photons are fiber coupled to the detector with about 75 % transmission. The anti-Stokes photons are first temporally gated by two acousto-optic modulators (AOMs) and later spectrally filtered by a 1 MHz-wide spectral hole burnt at the $1/2_g - 3/2_e$ transition frequency in a second $\text{Pr}^{3+}:\text{YSO}$ crystal, 3-mm long, also at 3.5 K. The total transmission in the anti-Stokes arm, from the cryostat to the detector, is typically 24 %. We use two Silicon single photon detectors (SPD) for the detection of both photons.

We prepare the AFC memory for $\tau_{\text{AFC}} = 8 \mu\text{s}$. The AFC preparation has two main step. The first step is described in Chapter 2.4.1. The second step is the shaping the AFC structure shown in Figure 7.4 on the single class feature. We follow the procedure discussed in Chapter 6.4 on the improved AFC efficiency section. The AFC shaping and spin-state cleaning procedures are repeated 1100 times. All the preparation pulses are sent along the read spatial mode. Then we start a progression of trials, each consisting of the pulse sequence depicted in Figure 7.2.

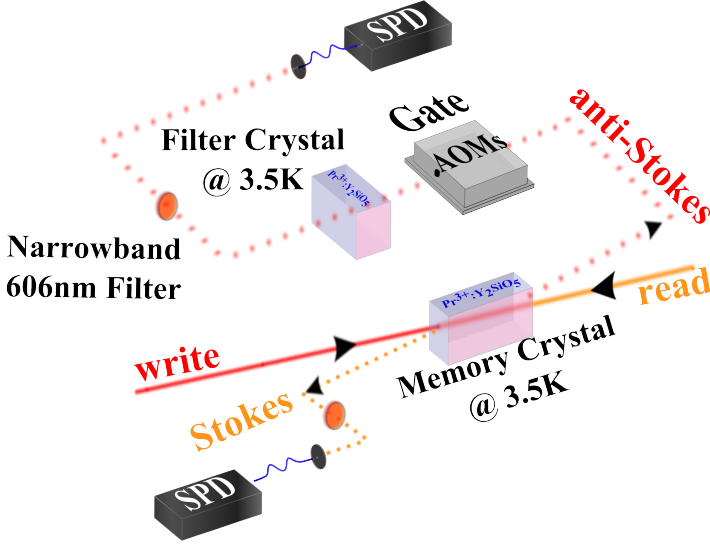


FIGURE 7.3: The experimental setup. Detailed description is given in the text.

The write pulses are $1 \mu\text{s}$ long (FWHM), and have a negative frequency chirp with a hyperbolic tangent waveform of 800 kHz. The read pulses, sent $8 \mu\text{s}$ after the write pulses, have a power of 24 mW, a duration of 900 ns (FWHM) and are +800 kHz frequency chirped with a hyperbolic tangent waveform. For one AFC preparation we send 500 write and read pulse pairs at intervals of $313 \mu\text{s}$ for P_w lower than $128 \mu\text{W}$. For higher P_w we decrease the number of trials in order to prevent deterioration of the AFC.

7.3.1 Characterization of Stokes and Anti-Stokes photons

We start our measurements by characterizing the light emitted in the Stokes mode. Figure 7.5(a) shows the temporal Stokes histogram in a $2 \mu\text{s}$ window, for a write power $P_w = 16 \mu\text{W}$. Figure 7.5(b) shows the time histogram of the anti-Stokes mode, after sending the read pulse. The

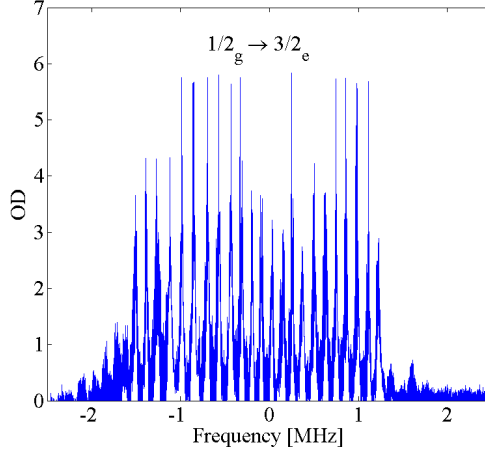


FIGURE 7.4: The AFC structure for $8 \mu\text{s}$ excited state storage time.

dotted vertical bars indicate the temporal mode where the anti-Stokes photons correlated to the Stokes photons of panel (a) should lie to satisfy the condition $T_S + T_{aS} = \tau_{AFC}$. This histogram shows a peak at around $8.5 \mu\text{s}$ originated from the second echo of the write pulse leaked into the anti-Stokes mode. Note that this peak is not in the temporal mode of the correlated anti-Stokes photons therefore it does not affect the correlation calculations.

We measure the probability to generate a Stokes photon P_s as a function of P_w , as shown in Figure 7.6(a). We observe a linear dependence, as predicted in [171] for $P_s \ll 1$. Figure 7.6(b) shows the spectrum of the emitted Stokes field. We characterize the Stokes photons frequency by spectral filtering with the help of the filter crystal that we use in the experiment. We send the write pulse from the read mode therefore we detect the Stokes photons after they pass through the filter crystal. We shift the 1 MHz hole burnt in the filter crystal to different frequencies. We infer that the branching ratio of the Stokes photons, β_{BR} , at the relevant $3/2_g - 3/2_e$ transition frequency is about 60%. It is worth to note that only 3% of the populations decays to the 3H_4 ground state. However the narrow band filter in the Stokes arm suppresses the Stokes photons that

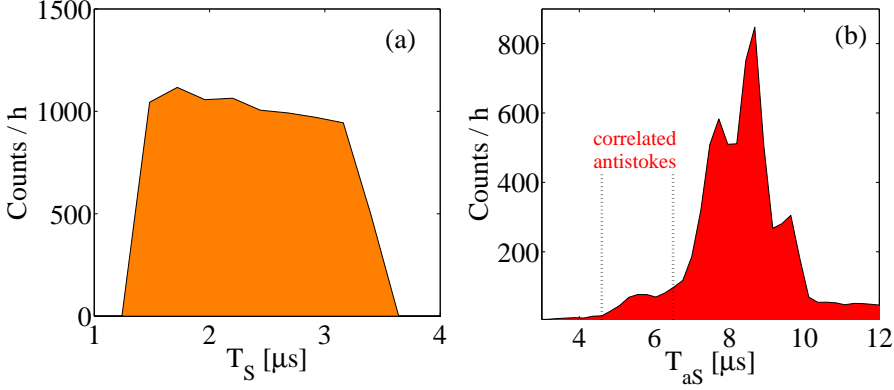


FIGURE 7.5: (a) Stokes count rate in a $2 \mu\text{s}$ detection window, for write pulse power of $16 \mu\text{W}$. We send the write pulse at $T_S = 0$. (b) Anti-Stokes photons histogram. The read pulse is sent at $T_{aS} = 0$.

heralds other spin excitations. These observations suggest that the light emitted in the Stokes mode comes from the direct excitation of the ions by the write pulse.

7.3.2 Non-classical correlations

We now look for coincidence detection between the Stokes and anti-Stokes modes.

We record the detection times of the Stokes (T_S) and anti-Stokes (T_{aS}) photons, and plot an histogram of the coincidences as a function of the sum $T_S + T_{aS}$. For correlated pairs, we expect a coincidence peak at $T_S + T_{aS} = \tau_{AFC}$. Figure 7.7(a) shows such a histogram for $P_w = 16 \mu\text{W}$, where we see a clear correlation peak around $\tau_{AFC} = 8 \mu\text{s}$. The shaded area indicates the time window used to quantify the second order cross-correlation function of the pairs. We also observe a smaller peak at $11 \mu\text{s}$, due to the noise generated by the second AFC echo of the write pulse (see Figure 7.5(b)). However, this peak is also present when Stokes and

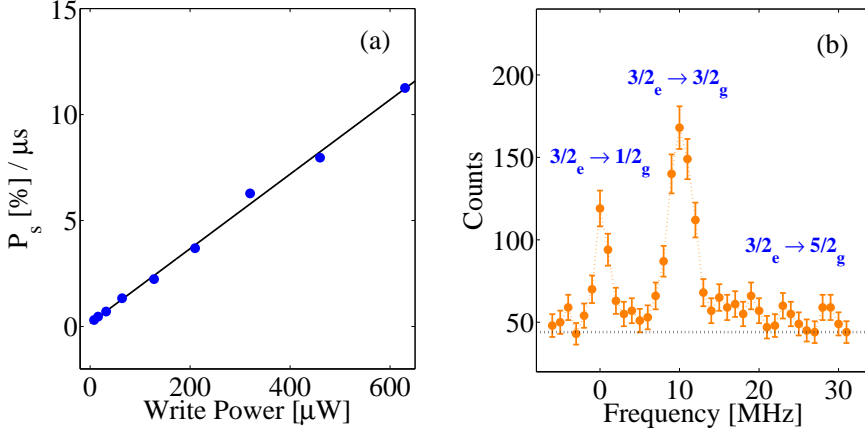


FIGURE 7.6: (a) Probability to create Stokes photons as a function of the write pulse power. The solid curve is a linear fit of the experimental data points. (b) Stokes counts as a function of the position of a 1 MHz-wide spectral hole burnt in the filter crystal. The 0 frequency corresponds to the frequency of the write pulse. The dotted gray horizontal line is the noise given by the detector dark counts.

anti-Stokes photons are detected in different trials and therefore does not correspond to correlated photons.

In order to quantify the correlation between Stokes and anti-Stokes photons, we measure intensity correlation functions. The second order cross-correlation function $g_{S,aS}^{(2)}$ is defined as $g_{S,aS}^{(2)} = p_{S,aS} / (p_S \cdot p_{aS})$, where $p_{S,aS}$ is the probability to detect a coincidence between Stokes and anti-Stokes photons and p_S (p_{aS}) is the probability to detect a Stokes (an anti-Stokes) photon. To infer $g_{S,aS}^{(2)}$, we measure the number of coincidences in a time window $\Delta\tau$ around $T_S + T_{aS} = \tau_{AFC}$ in the same trial, and we compare this number with the accidental coincidences recorded for Stokes and anti-Stokes photon emitted in different independent trials. An example is shown in Figure 7.7(b) for $P_w = 16 \mu W$ and $\Delta\tau = 1 \mu s$, which includes around 76 % of the total peak counts. For this particular example, with average $t_s = 5.6 \mu s$, we find $g_{S,aS}^{(2)}(\Delta\tau = 1 \mu s) = 21 \pm 4$. This is much higher than the threshold of about 6 enabling the violation of a Bell inequality if at least two modes are stored [184]. The inset in Figure 7.7(b)

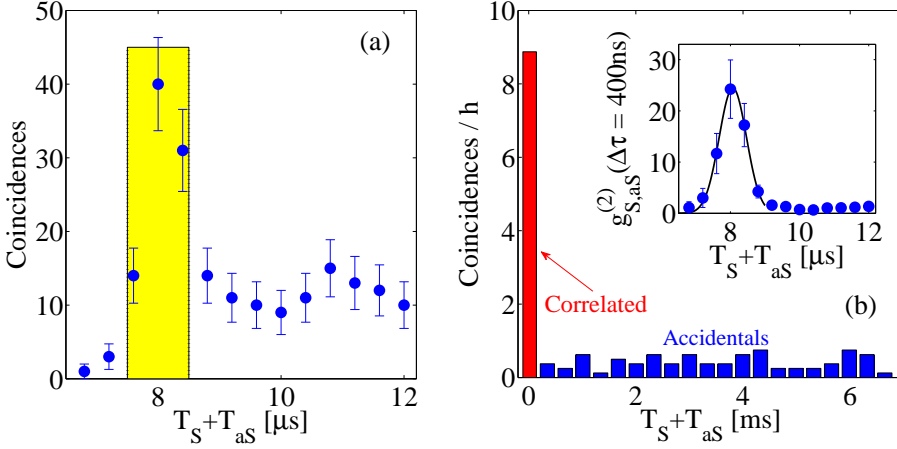


FIGURE 7.7: (a) Coincidence counts between Stokes and anti-Stokes photons as a function of the sum $T_S + T_{aS}$. The bin-size is $\Delta\tau = 400$ ns. (b) Coincidence counts per hour between Stokes and anti-Stokes photons in the $1 \mu\text{s}$ wide temporal mode around $T_S + T_{aS} = \tau_{AFC} = 8 \mu\text{s}$ in the same storage trial (bar at 0) and in different storage trials separated by multiples of $313 \mu\text{s}$. The $g_{S,aS}^{(2)}$ value is calculated as the ratio between the coincidences in the same storage trial and the average of the coincidences in different storage trials. The inset shows the peak in the $g_{S,aS}^{(2)}$ with bin-size of $\Delta\tau = 400$ ns. The fit of the correlation peak to a Gaussian curve, done over a $2 \mu\text{s}$ window around the peak, is also shown.

shows a zoom on the correlation peak for a smaller $\Delta\tau = 400$ ns, leading to $g_{S,aS}^{(2)}(\Delta\tau = 400\text{ns}) = 24 \pm 6$. The shape of the normalized correlation peak is fitted with a Gaussian curve and a temporal FWHM of (940 ± 100) ns is extracted. This is close to the expected width corresponding to the write pulse duration convoluted with the time-bin size.

To further characterize our system, we measure $g_{S,aS}^{(2)}(\Delta\tau = 1\mu\text{s})$ as a function of P_S (Figure 7.8), which can be adjusted by tuning P_w (see Figure 7.6(a)). We observe a reduction of the $g_{S,aS}^{(2)}$ value when P_S is increased, as expected for a DLCZ-like process. At lower P_S , the rate of Stokes photons becomes comparable to the noise and the value of $g_{S,aS}^{(2)}$ decreases.

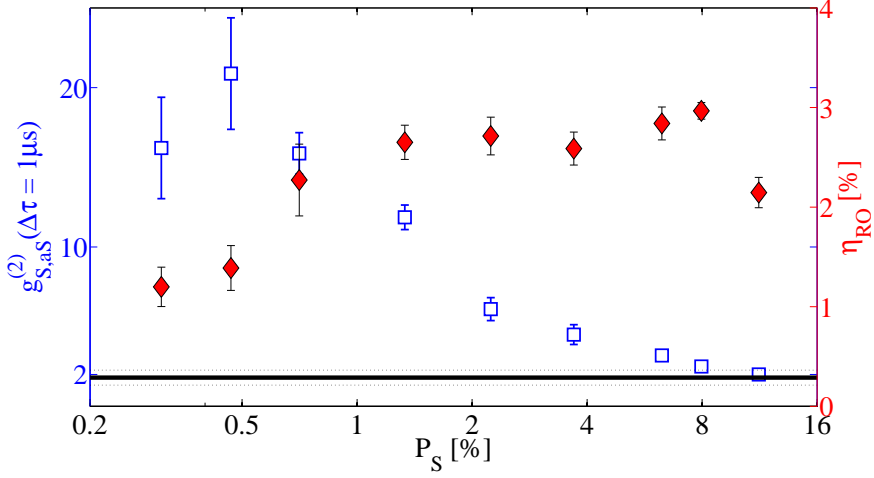


FIGURE 7.8: $g_{s,as}^{(2)}$ value (squares) and read-out efficiency (diamonds) as a function of the Stokes creation probability, P_s , calculated by the raw detection counts back propagated at the crystal using known losses. The black horizontal line sets the classical threshold for the $g_{s,as}^{(2)}$ given by the Cauchy-Schwarz inequality.

In order to prove unambiguously the non-classical correlations between the two photons, we use the Cauchy-Schwarz inequality:

$$R = \frac{(g_{s,as}^{(2)})^2}{g_{s,s}^{(2)} g_{a,s,a,s}^{(2)}} \leq 1,$$

where $g_{s,s}^{(2)}$ and $g_{a,s,a,s}^{(2)}$ are second order auto-correlation functions of Stokes and anti-Stokes photons, respectively. To measure these quantities, we introduce a 50/50 fiber splitter and two SPDs in the Stokes (anti-Stokes) and proceed in a similar way as for the cross-correlation. With $P_w = 64 \mu W$ we find $g_{s,s}^{(2)}(\Delta\tau = 1 \mu s) = 1.85 \pm 0.36$, $g_{a,s,a,s}^{(2)}(\Delta\tau = 1 \mu s) = 1.75 \pm 0.57$, and $g_{s,as}^{(2)}(\Delta\tau = 1 \mu s) = 11.9 \pm 0.9$. Eventually we find $R = 44 \pm 20 \not\leq 1$ which clearly violates the inequality by more than 2 standard deviation.

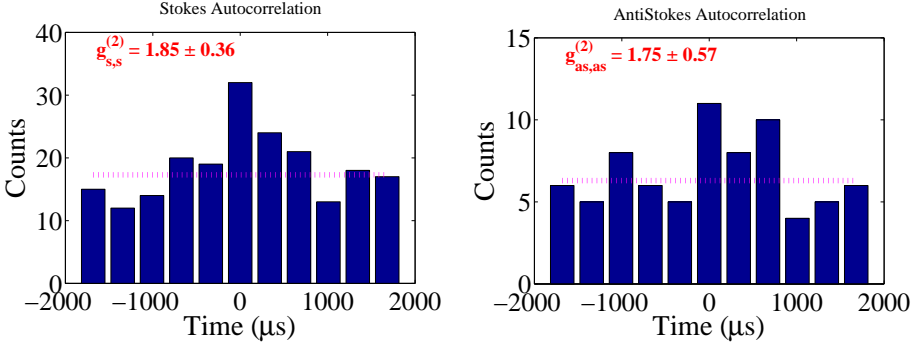


FIGURE 7.9: Autocorrelation measurements of Stokes and anti-Stokes photons. The dotted line represents the average of the side bins.

7.3.3 Read-out efficiency

We also measure the read-out efficiency $\eta_{RO} = (p_{S,aS} - p_{S,aS}^{acc})/p_S$ as a function of P_S , where $p_{S,aS}^{acc}$ is the accidental coincidence probability. The measured value of the read-out efficiency can be compared to the expected one with our experimental parameters. The latter can be estimated as $\eta_{RO}^{exp} = \eta_{RP} \cdot \eta_{reph} \cdot \eta_{coh} \cdot \beta_{BR} \cdot \beta_G$, where η_{RP} is the transfer efficiency of the read pulse, η_{reph} is the rephasing efficiency of the AFC, η_{coh} is the coherence in the spin-state, β_{BR} is the branching ratio of 60%, and β_G is the fraction of the pulse counts in the detection window $\Delta\tau$. We calculate η_{RO}^{exp} by measuring η_{RP} , η_{reph} , η_{coh} , and β_{BR} separately.

In order to find the η_{RP} we conduct *classical* DLCZ-AFC experiment. We prepare the AFC and send a write pulse but, instead of Stokes photons detection, a weak probe pulse resonant with the $3/2_g - 3/2_e$ transition is sent which transfers a small part of the ions from the excited state to the spin state. The weak probe is sent from the anti-Stokes spatial mode in the temporal window of the Stokes detection. The stimulated transfer generates photon emission (gain) during the weak pulse which is proportional to the number of ions transferred to the spin state. The strong read pulse transfers the population back to the excited state and the collective emission occurs. By detecting the gain of the weak probe and the collective emission of the AFC we extract $\eta_{RP} = 40\%$.

We calculate the coherence in the spin state by taking into account the inhomogeneous spin broadening measured in the Figure 7.10(a). For a 2 μ s-wide Stokes window, the average spin state storage time is 5.6 μ s which leads to preservation of 64% of the coherence.

The AFC efficiency can be defined as $\eta_{AFC} = \eta_{write} \cdot \eta_{rephasing} \cdot \eta_{loss}$, where we measure $\eta_{AFC} = 17\%$. The efficiency of the write pulse is defined as $\eta_{write} \approx 1 - e^{-d/F}$ where d is the absorption depth and F is the finesse of the AFC. The loss in the AFC protocol is defined as $\eta_{loss} = e^{-d_0}$ where d_0 is the background absorption. We measure an average d of 5.4, F of 4.4 and $d_0 = 0.4$, and finally find $\eta_{rephasing} = 36\%$.

When measuring the read-out efficiency, we consider $\Delta\tau = 1\mu$ s, which includes a fraction $\beta_G = 76\%$ of the coincidence peak.

Finally the expected readout efficiency is $\eta_{RO}^{exp} = 40\% \cdot 64\% \cdot 36\% \cdot 60\% \cdot 76\% = 4.2\%$. We observe a linear increase up to $P_S=1\%$, due to the noise in the Stokes mode. Afterwards it stays constant around 3%, close to the expected value.

7.3.4 Controllable delay between the pairs and multi-modality

In order to show that the delay between the Stokes and anti-Stokes photons can be controlled, we measure the retrieval efficiency as a function of the storage time in the spin-state t_s , as shown in Figure 7.10(a). The data are fitted with a Gaussian curve, from which we extract a $1/e$ decay constant of $(8.3 \pm 0.8) \mu$ s. This decay is likely due to inhomogeneous broadening of the spin transition. The same measurement in a standard spin-wave AFC experiment in this crystal gives a similar value $(9.9 \pm 1.5) \mu$ s. The decay in η_{RO} also affects $g_{S,aS}^{(2)}$, as shown in Figure 7.10(b). Nevertheless, we observe non-classical correlation for t_s up to 12 μ s, corresponding to a total storage time of $t_s + \tau_{AFC} = 20 \mu$ s.

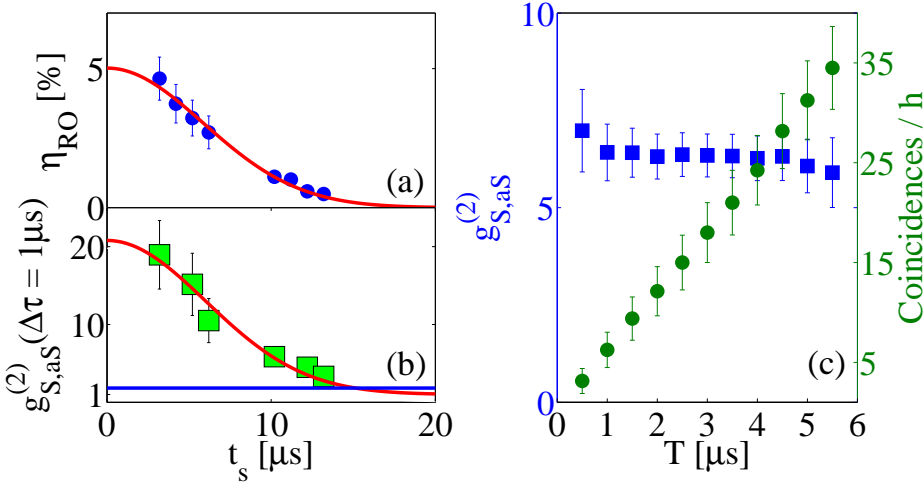


FIGURE 7.10: Read-out efficiency (a) and $g_{S,aS}^{(2)}(\Delta t = 1\mu s)$ cross-correlation values (b) as a function of the storage time in the spin state t_s . The red line is the fit of the experimental data to a Gaussian decay which gives a $1/e$ decay time of $(8.3 \pm 0.8) \mu s$, corresponding to a spin inhomogeneous linewidth of 45 ± 2 kHz (44 ± 4 kHz for $g_{S,aS}^{(2)}$). For this curve, we do not subtract the accidental counts. The blue horizontal line in (b) sets the classical threshold for the $g_{S,aS}^{(2)}$ given by the Cauchy-Schwarz inequality. (c) $g_{S,aS}^{(2)}(\Delta t = 1\mu s)$ cross-correlation (squares) and coincidence counts per hour (circles) between the Stokes and anti-Stokes photons as a function of Stokes window size, T . The total Stokes window size is $5.5 \mu s$.

Finally, we discuss the temporal multimode nature of our source. The detection of a Stokes photon at a different time T'_S creates a spin-wave that will also rephase at a different time T'_{aS} , still preserving $T'_S + T'_{aS} = \tau_{AFC}$. The maximal number of modes is given by $N_m = T/\Delta\tau$, where T is the detection window of the Stokes photons. In the data processing stage we adjust the Stokes window size as multiples of the temporal FWHM of the write pulse. The values are averages of all possible windows for different window sizes, e.g. 11 data for 500 ns window, 9 data for 1500 ns window etc. In this measurement, the write pulses have $P_w = 64 \mu W$ and a duration of 500 ns (FWHM). The read pulse is sent 15 μs after the write pulse. The decrease on $g_{S,aS}^{(2)}$ with respect to the one in Figure 7.10(a) is due to the longer spin-state storage time and less efficient read-out for 500

ns write pulse ($\eta_{RO} = 1\%$). Note that there is a trade-off between the number of modes and the read-out efficiency of each mode. The efficiency is maximized if $\Delta\tau$ is bigger than the correlation peak. In our case, we choose $\Delta\tau$ comparable to the FWHM of the peak. Figure 7.10(c) shows the coincidence count rate and the $g_{S,aS}^{(2)}$ as a function of T . We observe a linear increase in the coincidence count rate as a function of T . At the same time, the $g_{S,aS}^{(2)}$ values stay constant. This shows an important feature of our scheme: adding more temporal modes increases the coincidence rate but does not increase the noise. The maximal number of modes in our current experiment is $N_m = T/\Delta\tau = 11$ modes, a factor of 5 improvement with respect to previous multimode DLCZ-like experiments [183, 185].

7.4 Towards entanglement between a photon and a spin-wave

In the previous section, we demonstrated quantum correlations between the Stokes and anti-Stokes photons. In this section, we report preliminary experiments towards the demonstration of energy-time entanglement between the two photons. Due to the temporal multiplexing capability of the protocol, the photon pairs are emitted in a superposition of several temporal modes, with $T_S + T_{aS} = 1/\Delta$. In order to analyze such an entanglement, we should send the two photons through two unbalanced interferometers, analogous to the Franson configuration [186]. Here, instead of using interferometers, we use an AFC in the filter crystal, as proposed in [187] where the transmitted part of the light plays the role of the short interferometer arm, while the AFC echo represent the long arm. We prepare an AFC structure with a storage time of $2\ \mu\text{s}$ in the filter crystal and send both Stokes and anti-Stokes photons to the Filter AFC, as depicted in the experimental setup in Figure 7.11.

The effect of sending both Stokes and anti-Stokes photons to an AFC is described in the schematic in Figure 7.12. After the filter AFC, each Stokes

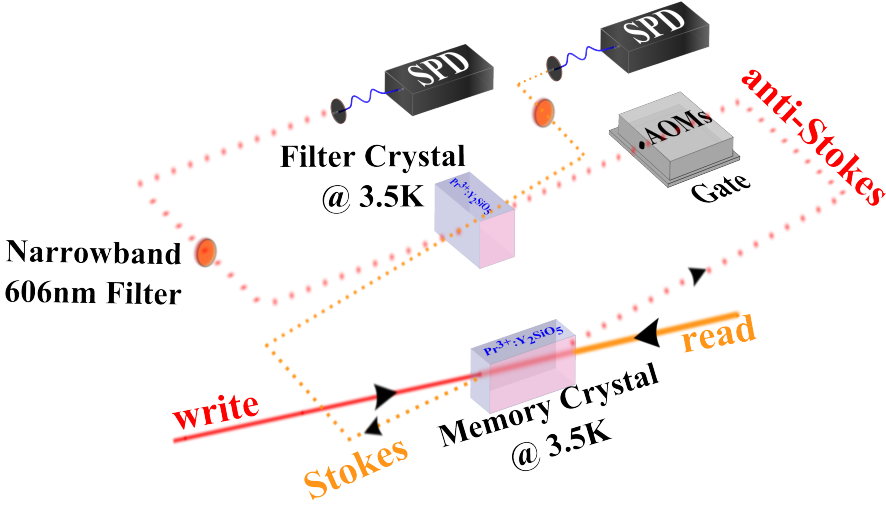


FIGURE 7.11: The modified version of the setup. Both Stokes and anti-Stokes photons are directed to the filter crystal where a $2 \mu\text{s}$ AFC is burnt.

(anti-Stokes) mode is separated into two time-bins, transmitted Stokes (anti-Stokes) $|S_T\rangle$ ($|AS_T\rangle$) and echo Stokes (anti-Stokes) $|S_E\rangle$ ($|AS_E\rangle$). When we look at the $T_s + T_{as}$ coincidence window, there will be three peaks. The first one collects the coincidences of the pairs coming from the transmitted parts of both Stokes and anti-Stokes by the filter AFC without any delay (as if both passed through the short arm of the interferometers) hence the peak appears at the storage time of the memory AFC τ_{Memory} . The last peak is also similar to the first one. It is built by the coincidences between Stokes and anti-Stokes both being stored in the filter AFC and appears at $\tau_{Memory} + 2\tau_{Filter}$. The peak in the middle is the one we are interested in, since two states overlaps at that time-bin indistinguishably. It contains not only the coincidences of transmitted Stokes and echo anti-Stokes but also the echo Stokes and transmitted anti-Stokes, where both give a coincidence peak at $\tau_{Memory} + \tau_{Filter}$. The post-selected time-bin state can be written as

$$\frac{1}{\sqrt{2}}(|S_T AS_E\rangle + e^{i\theta}|S_E AS_T\rangle) \quad (7.8)$$

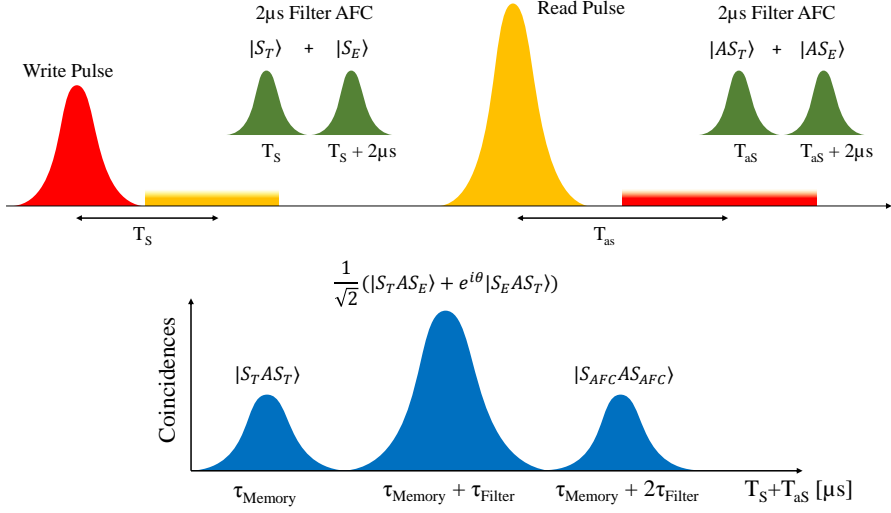


FIGURE 7.12: Schematic of the time-bin states of Stokes and anti-Stokes photons and the expected coincidence histogram with the time-bin overlaps.

where $\theta = \theta_s - \theta_{as}$. The frequency detuning δ between the input field and the AFC leads to a phase factor $e^{i2\pi\delta/\Delta}$ in the output field [142]. Therefore by shifting the frequency of one field, we can observe a two photon interference fringe and show the coherence in the process.

We modified some of the experimental parameters in order to distinctly separate the time-bins. In the memory crystal we prepare the AFC structure with the same strategy described in the experimental part except for the excited state storage time which becomes $9 \mu s$. The FWHM of the write and pulses are now around 800 ns and the Stokes window size is $2.4 \mu s$. We adjust the efficiency and the transmitted parts of the $2\mu s$ filter AFC such that both areas are equal and around 35% of the input pulse. In this configuration, we suffer from the leakage of the read pulse which couples into the Stokes mode, creates echos in the filter crystal and leaks to the anti-Stokes detection mode. In order to observe the least leakage we follow the conditional sequence approach and we send the read pulse only when we detect a Stokes photon.

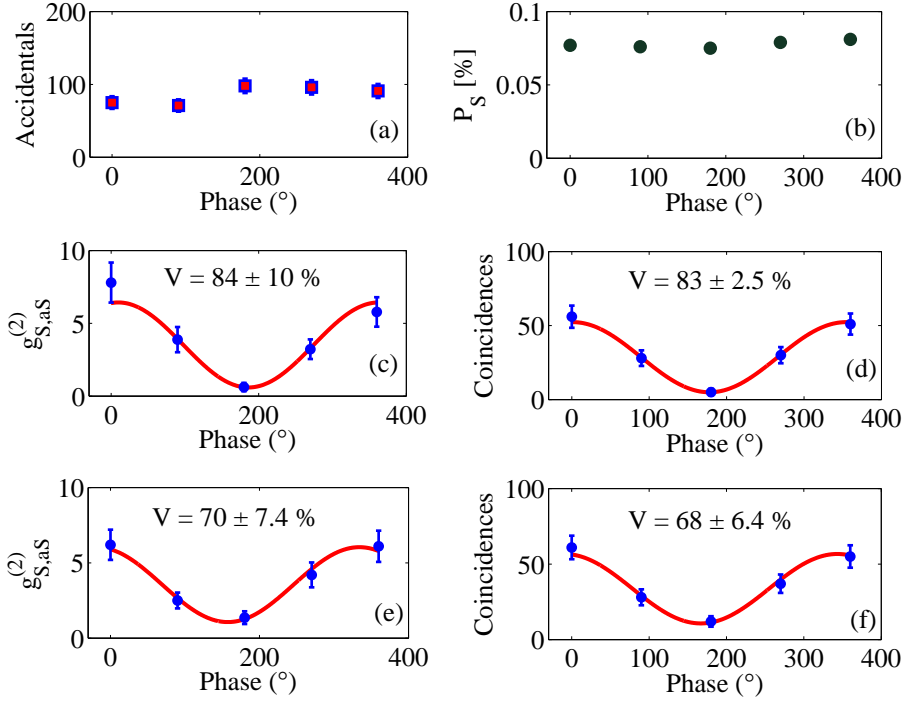


FIGURE 7.13: Plots (a) and (b) show the accidental counts and the probability to generate Stokes photons, respectively, at different phase conditions. (c) and (d) show the $g_{S,aS}^{(2)}$ and the coincidence values, respectively, as a function of the phase θ . In plots (e) and (f), the AFC in the filter crystal is shifted by 250 kHz which affects in the same measure in the echo of both Stokes and anti-Stokes photons.

We adjust the phase of the echo of the anti-Stoke photons by shifting the frequency of the gating AOMs in order to observe the interference fringe. For example, a 250 kHz shift in the anti-Stokes frequency corresponds to a π shift in the echo due to the fact that Δ of the AFC in the filter crystal is 500 kHz for 2 μ s AFC storage. The results of this strategy is given in Figure 7.13. Each data point is the average of 5 measurements of 1 hour, taken without any order. We first look at the plot (a) and (b) for any sign of single photon interference in the accidentals and in the Stokes probability, respectively. No interference fringe is observed in both cases. In the plot (c) and (d) we show the $g_{S,aS}^{(2)}$ and the coincidence values. We fit the data with sinusoidal functions and obtain a two photon interference

visibility of around 83%. In the second part, we shift the frequency of the AFC in the filter crystal by 250 kHz and repeat the experiment. In this case, the phase of both Stokes and anti-Stokes echoes are shifted by the same amount hence we do not see any shift in the fringe. However we are still able to see visibility values around 70 % which lets us to conclude that the coherence is preserved during the storage.

7.5 Discussion

Several improvements to our system are possible. The Stokes probability could be improved, without resorting to higher write pulse powers. For example longer crystals or, to some extent, higher concentrations could be employed to achieve higher OD. The light-atom interaction could also be enhanced with external cavities. The read-out efficiency can be increased by filtering the Stokes photon to suppress wrong heralds, by improving the quality of the AFC, by increasing the optical depth using e.g. longer crystals, and by optimizing the transfer efficiency. The storage time could be greatly improved using spin-echo techniques [124], with prospects of up to tens of seconds in our crystal [69] or hours in Europium doped crystals [70]. Even though the emitted photons are at 606 nm, it is possible to efficiently convert them to telecom C-band wavelength using quantum frequency conversion techniques [72].

It is worth to note that swapping the Stokes and anti-Stokes spatial modes decreases the coincidence rate around 1 order of magnitude even though the phase matching condition should still satisfy. The reason is still under investigation.

Our observation of non-classical correlations between photon pairs emitted from a solid-state ensemble with a controllable delay by using photon counting techniques represents an important achievement towards scalable

quantum repeater architectures. It also paves the way towards heralded entanglement of remote solids with temporal multiplexing, which can greatly enhance the distribution rate of entanglement [39].

In the last part of the chapter, we presented measurements of two photon interference between the Stokes and anti-Stokes photons, with visibilities up to $83 \pm 2.5 \%$. In order to violate Bell inequality and prove entanglement unambiguously, we need to show visibilities higher than 70% in two basis phase shifted by 90° . With the current configuration, we do not have access to the second base. By burning two independent AFCs for Stokes and anti-Stokes photons in the filter crystal, spectrally or spatially separated, it would be possible to realize the experiment in two different basis.

Chapter 8

Conclusions and outlook

8.1 Summary of the thesis

The main goal of this thesis was to investigate new quantum memory protocols for solid state devices. I demonstrated two protocols for the first time which offer certain advantages over the current schemes. I also presented important improvements in a well-known protocol, reporting state-of-art results. In all the experiments, we used a rare-earth doped crystal, specifically $\text{Pr}^{3+}\text{Y}_2\text{SiO}_5$. My PhD studies also included building a new experimental setup and contributing to other important experiments which are not included in this thesis.

The first protocol that we demonstrated is the spectral hole memory (SHoMe) scheme. It was proposed by Lauro and co-workers in 2009 [112]. The protocol is based on creation of a spectral hole in the absorption line of the doped crystal and transferring the coherence back and forth between the spin state and excited state with two π Raman pulses. The SHoMe protocol is similar to the well-known electromagnetically induced transparency (EIT) protocol with the slow and stopped light phenomena. However, the SHoMe protocol relies on a long-lived spectral hole created before the pulse to be stored is sent. This allows the use of Raman control pulses

separated in time from the retrieved signal. This is beneficial in the single photon level light storage which have never been demonstrated with EIT in doped solids. The SHoMe protocol does not rely on complicated preparation processes, it only requires a Λ system, a single class of ions with high OD and Raman pulses with high transfer efficiency. In the experiment, we sent an input pulse with 3 μs FWHM to a 230 kHz spectral hole with OD around 8. We reached stopped light efficiency of around 40% which outperforms other reported single pass 3-level storage efficiency values in solid-state devices. We characterized storage efficiencies as a function of OD and compared the experimental values with the results of numerical simulation. We observed that squarish hole shapes can provide higher storage efficiency. We also characterized the effect of the hole width on the storage efficiency and on the slow light time delay. Later we moved to the single photon level regime. By applying temporal and spectral filtering techniques, we reached a storage efficiency of 31% and also a SNR of 33 ± 4 for an input photon number of 1, the highest reported values for solid state spin-wave optical memories at the single photon level. In the light of these results, we can say that this protocol is very promising for the storage of quantum light.

In the second experimental chapter, we discussed the well-known AFC protocol. It is based on tailoring the absorption profile of the ensemble with periodic features with period Δ , which lead to rephasing and collective re-emission after a predetermined time storage time of $1/\Delta$. In the first experiment, we presented the result of a 2-level AFC storage of 1570nm telecom photons after conversion to 606 nm using a non-linear PP-KTP crystal with a strong 987nm pump light. We used the AFC as a spectral filter which led to a 270-fold improvement in the μ_1 value compared to only QFC case. The measured AFC storage efficiency was 19.8% at 1.6 μs storage time with a total efficiency of 1.55% including the QFC device efficiency and optical losses. These results outperformed the previous storage experiments of telecom light in the single photon level. In this chapter I

also presented measurements of excited state storage with improved storage efficiency and storage times and briefly discussed the experimental modifications. We obtained 2-level AFC efficiencies around 28% until 8 μs storage time and more than 10% at 12 μs . I also showed 3-level AFC results. We reached spin-wave AFC efficiency of 14% and 8.5% with classical pulses and at the single photon level, respectively. These values present the state-of-art of the reported spin-wave AFC efficiencies in both regimes.

The last quantum memory protocol that I presented is a hybrid combination of the DLCZ and AFC protocols. It offers the advantages of both schemes, such as creation of non-classical photon pairs with embedded memory and temporal multi-modality. The protocol starts with the AFC preparation and then continues with sending write and read pulses. The Stokes photons are detected between the write pulse and its first AFC echo. Each Stokes photon heralds a single spin excitation which is then stored for a programmable time and retrieved by a read pulse to create an anti-Stokes photon. The total time spent in the excited state should be equal to the τ_{AFC} hence we expect to see a peak at that time when we sum the time delays between the write pulse and a Stokes detection and between the read pulse and an anti-Stokes detection. In the experiment, the peak was clearly visible and gave a $g_{s,as}^{(2)}$ of 21 ± 4 for 16 μW write pulse power. We characterized the Stokes photons creation probability as a function of write pulse power and also the number of Stokes counts as a function of frequency. We also characterized the $g_{s,as}^{(2)}$ and the read-out efficiency values as a function of the Stokes creation probability and of the spin-state storage time. In order to prove the non-classical nature of the pairs, we measured the $g_{s,s}^{(2)}$ and the $g_{as,as}^{(2)}$ functions and observed a violation of the Cauchy-Schwarz inequality with more than 2 standard deviations. We showed the storage of 11 temporal modes by dividing the Stokes window into smaller parts and calculating the $g_{s,as}^{(2)}$ and coincidence rate. We went one step further by showing preliminary measurements demonstrating energy-time entanglement between Stokes and anti-Stokes photons. To analyse the entanglement they are both sent to an equally

balanced AFC which played the role of an unbalanced interferometer. We observed two-photon interference fringes with visibility values of 83 ± 2.5 % and 68 ± 6.4 % in the time-bin where the coincidences are indistinguishable. All these results present a significant step towards scalable quantum repeater architectures.

8.2 Outlook

8.2.1 Performance improvements

In the thesis I presented state of art results in terms of storage efficiencies in the SHoMe and AFC protocols. However there are still space for improvements. For example higher OD and more efficient control pulses (with more power or longer pulse durations) can lead to larger efficiency values in all the protocols presented here. There are also other improvements that can be realized in specific protocols.

The analytical simulations done by T. Chanelière show that it is possible to reach efficiency values higher than 50 % in the SHoME protocol. There are several improvements that can be done, such as increasing the optical depth, optimizing the duration and the shape of the input and the Raman pulses, and also optimization of the shape of spectral hole. In the near future, we will work on the shape and the duration of the pulses and the spectral hole.

In the 2-level AFC, the maximum theoretical efficiency that we can obtain is around 40 % for an OD value of 7 with square comb shapes [163]. Here we presented efficiency values around 30 % hence we are not far away from the theoretical limit. However we have limited the emission in the forward direction due to the fact that we have always applied co-propagating control pulses in the spin-wave storage. It is possible to overcome this limitation by applying counter propagating control pulses and obtain backward emission. However this scheme requires dividing the optical power into two

modes. Therefore in order to keep the same Rabi frequency, we have to double the power.

The $g_{s,as}^{(2)}$ values in the DLCZ-AFC protocol can be increased by filtering the Stokes photons, however our main concern here would be the coincidence rate since our $g_{s,as}^{(2)}$ values are high enough. Larger Stokes detection windows hence higher degree of temporal multi-modality would lead to an increase in the coincidence rate but it would require longer excited state storage time in order to not overlap with the leakage of the write pulse echo in the Stokes mode. The coincidence rate can be also increased by increasing the repetition rate of the experiment. The readout efficiency is mostly limited by the rephasing and read pulse efficiencies. The rephasing efficiency can be increased by optimization of the AFC preparation.

Another important improvement that we will work on is the storage time. All three protocols store the information in the spin state of the crystal which offers prospects for long-lived storage. However, the current realizations are limited to storage times of the order of a few tens of microseconds by the inhomogeneous spin broadening. It is possible to increase the total storage time to the order of hundreds of micro seconds by using spin-echo techniques. We are currently working on this implementation.

8.2.2 Future directions

Quantum teleportation is a key resource in the quantum repeater architectures. In our group, one of the long run goal is demonstrating teleportation between two ensemble nodes. It first requires to generate heralded entanglement between remote crystals. This can be realized by using two SPDC photon pair sources and two Pr:YSO crystal setups which we already have. The AFC protocol is suitable for this experiment. Another way would be to use the DLCZ-AFC protocol to create photon pairs in the two Pr:YSO crystals. Quantum entanglement does not have to be done in the same

atomic systems, we can also demonstrate it between a cold atomic ensemble and a crystal. It is possible to overcome the frequency mismatch between two systems by using quantum frequency conversion techniques [72, 188].

Another long term goal of the group is the miniaturization of the devices in order to integrate on-chip demonstrations. There are already ongoing research using waveguide structure in our group [134] and other groups [157, 189, 190]. Another way of miniaturization is coupling REID ensembles on photonic nanocavities [191, 192]. REID optical fibers are also candidates for scalable integrated quantum memories [193, 194]. Investigations on the detection of single Pr^{3+} ion have also been conducting in different groups [195–197]. Finally, another research direction deals with the detection and manipulation of single rare-earth ions in optical cavities [198].

Appendix A

9 classes of ions in Pr:YSO

The Pr:YSO crystal has 3 ground and 3 excited states in the $^3H_4(0)$ - $^1D_2(0)$ transition. The effect of the crystal field on the ions varies due to the inhomogeneity in the crystal which leads to 9 different classes of ions, as shown in Figure A.1. Figure A.2 shows all the individual transitions with the relative oscillator strengths (see 2.1) represented with the vertical bars. The last figure was made by Patrick M. Ledingham, one of the former post doc in our group.

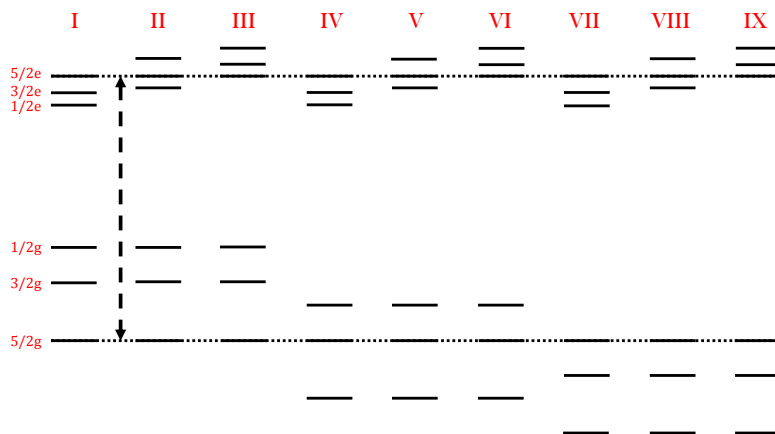


FIGURE A.1: Hyperfine level structures of 9 classes

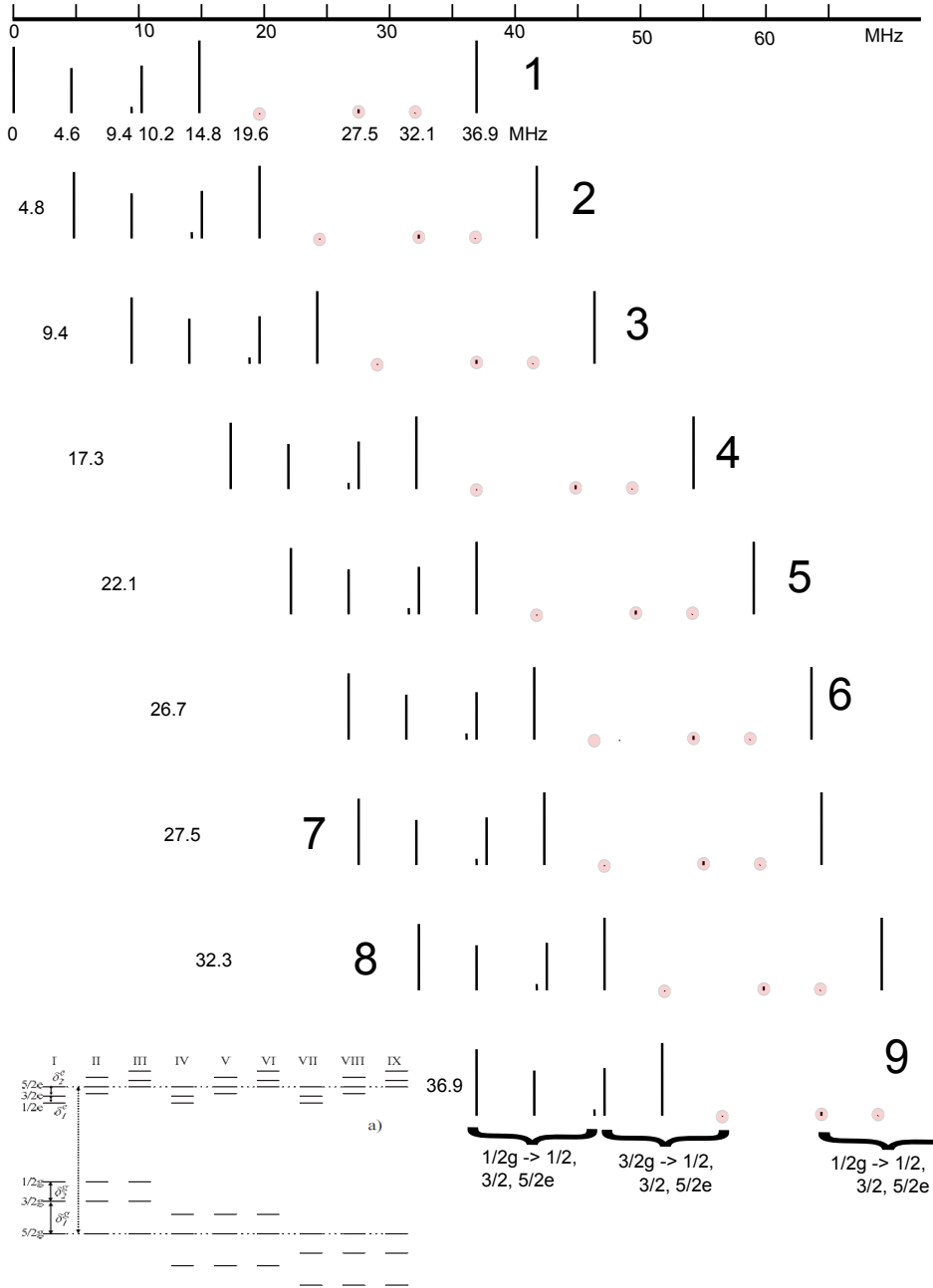


FIGURE A.2: Spectral positions of each individual transition

Bibliography

- [1] J. Dewey: *Democracy and education: an introduction to the philosophy of education*, Free Press (1966).
- [2] P. Lester: *Visual Communication: Images with Messages*, Thomson Wadsworth (2006).
- [3] P. Tallet: *Ayn Sukhna and Wadi el-Jarf: Two newly discovered pharaonic harbours on the Suez Gulf*, British Museum Studies in Ancient Egypt and Sudan **18**, 147 (2012).
- [4] J. Needham and T. Tsuen-Hsuei: *Science and Civilisation in China*, vol. Volume 5. Chemistry and Chemical Technology, Cambridge University Press (September 1985).
- [5] J. Curran, N. Fenton, and D. Freedman: *Misunderstanding the Internet*, Communication and Society, Taylor & Francis (2016).
- [6] P. Salvo and M. Hernandez-Silveira: *Wireless Medical Systems and Algorithms: Design and Applications*, Devices, Circuits, and Systems, CRC Press (2016).
- [7] M. J. Montgomery: *What works in water supply and sanitation projects in developing countries with EWB-USA*, Reviews on Environmental Health **31**, 85 (1969).
- [8] S. Bentley: *Food For All*, Geodate **29**, 3 (2016).

- [9] E. S. Herman and N. Chomsky: *Manufacturing Consent: The Political Economy of the Mass Media*, Current affairs/Mass media, Pantheon Books (2002).
- [10] A. Gramsci and J. Buttigieg: *Prison Notebooks*, no. v. 1 in European Perspectives: A Series in Social Thought and Cultural Criticism, Columbia University Press (1992).
- [11] R. P. Feynman: *Quantum Mechanical Computers*, Optics News **11**, 11 (1985).
- [12] M. Lewenstein, A. Sanpera, and V. Ahufinger: *Ultracold Atoms in Optical Lattices: Simulating quantum many-body systems*, Oxford University Press, Oxford (2012).
- [13] M. A. Nielsen and I. L. Chuang: *Quantum Computation and Quantum Information*, Cambridge (2000).
- [14] B. Schumacher: *Quantum coding*, Phys. Rev. A **51**, 2738 (1995).
- [15] A. Einstein: *Zur Elektrodynamik bewegter Körper*, Annalen der Physik **17**, 891 (1905).
- [16] A. Einstein, B. Podolsky, and N. Rosen: *Can Quantum-Mechanical Description of Physical Reality Be Considered Complete?*, Phys. Rev. **47**, 777 (1935).
- [17] E. Schrödinger: *Discussion of Probability Relations Between Separated Systems*, Proc. Cambridge Philo. Soc. **31**, 555 (1935).
- [18] D. Bohm: *A Suggested Interpretation of the Quantum Theory in Terms of "Hidden" Variables. I*, Phys. Rev. **85**, 166 (1952).
- [19] J. Bell: *On the Einstein-Podolsky-Rosen paradox*, Physics **1**, 195 (1964).
- [20] S. J. Freedman and J. F. Clauser: *Experimental Test of Local Hidden-Variable Theories*, Phys. Rev. Lett. **28**, 938 (1972).

- [21] A. Aspect, P. Grangier, and G. Roger: *Experimental Realization of Einstein-Podolsky-Rosen-Bohm Gedankenexperiment : A New Violation of Bell's Inequalities*, Phys. Rev. Lett. **49**, 91 (1982).
- [22] B. Hensen, H. Bernien, A. E. Dreau, A. Reiserer, et al.: *Loophole-free Bell inequality violation using electron spins separated by 1.3 kilometres*, Nature **526**, 682 (2015), letter.
- [23] M. Giustina, M. A. M. Versteegh, S. Wengerowsky, J. Handsteiner, et al.: *Significant-Loophole-Free Test of Bell's Theorem with Entangled Photons*, Phys. Rev. Lett. **115**, 250401 (2015).
- [24] L. K. Shalm, E. Meyer-Scott, B. G. Christensen, P. Bierhorst, et al.: *Strong Loophole-Free Test of Local Realism**, Phys. Rev. Lett. **115**, 250402 (2015).
- [25] W. Rosenfeld, D. Burchardt, R. Garthoff, K. Redeker, et al.: *Event-Ready Bell Test Using Entangled Atoms Simultaneously Closing Detection and Locality Loopholes*, Phys. Rev. Lett. **119**, 010402 (2017).
- [26] D. Bouwmeester, J.-W. Pan, K. Mattle, M. Eibl, et al.: *Experimental quantum teleportation*, Nature **390**, 575 (1997).
- [27] C. H. Bennett and S. J. Wiesner: *Communication via one- and two-particle operators on Einstein-Podolsky-Rosen states*, Phys. Rev. Lett. **69**, 2881 (1992).
- [28] W. Tittel, J. Brendel, B. Gisin, T. Herzog, et al.: *Experimental demonstration of quantum correlations over more than 10 km*, Phys. Rev. A **57**, 3229 (1998).
- [29] C. H. Bennett and G. Brassard: *IEEE, New York*, in *Proceedings of the IEEE International Conference on Computers, Systems, and Signal Processing, Bangalore, India* (1984).
- [30] A. K. Ekert: *Quantum cryptography based on Bell's theorem*, Phys. Rev. Lett. **67**, 661 (1991).

- [31] N. Sangouard, C. Simon, H. de Riedmatten, and N. Gisin: *Quantum repeaters based on atomic ensembles and linear optics*, Rev. Mod. Phys. **83**, 33 (2011).
- [32] D. Dieks: *Communication by {EPR} devices*, Physics Letters A **92**, 271 (1982).
- [33] W. K. Wootters and W. H. Zurek: *A single quantum cannot be cloned*, Nature **299**, 802 (1982).
- [34] H.-J. Briegel, W. Dür, J. I. Cirac, and P. Zoller: *Quantum Repeater: The Role of Imperfect Local Operations in Quantum Communication*, Phys. Rev. Lett. **81**, 5932 (1998).
- [35] M. Zukowski, A. Zeilinger, M. A. Horne, and A. K. Ekert: *“Event-ready-detectors” Bell experiment via entanglement swapping*, Phys. Rev. Lett. **71**, 4287 (1993).
- [36] L.-M. Duan, M. D. Lukin, J. I. Cirac, and P. Zoller: *Long-distance quantum communication with atomic ensembles and linear optics*, Nature **414**, 413 (2001).
- [37] L. Jiang, J. M. Taylor, and M. D. Lukin: *Fast and robust approach to long-distance quantum communication with atomic ensembles*, Phys. Rev. A **76**, 012301 (2007).
- [38] Z.-B. Chen, B. Zhao, Y.-A. Chen, J. Schmiedmayer, et al.: *Fault-tolerant quantum repeater with atomic ensembles and linear optics*, Phys. Rev. A **76**, 022329 (2007).
- [39] C. Simon, H. de Riedmatten, M. Afzelius, N. Sangouard, et al.: *Quantum Repeaters with Photon Pair Sources and Multimode Memories*, Phys. Rev. Lett. **98**, 190503 (2007).
- [40] N. Sangouard, C. Simon, B. Zhao, Y.-A. Chen, et al.: *Robust and Efficient Quantum Repeaters with Atomic Ensembles and Linear Optics*, Phys.Rev.A **77**, 062301 (2008).

- [41] B. C. Jacobs, T. B. Pittman, and J. D. Franson: *Quantum relays and noise suppression using linear optics*, Phys. Rev. A **66**, 052307 (2002).
- [42] A. Kuzmich, W. P. Bowen, A. D. Boozer, A. Boca, et al.: *Generation of nonclassical photon pairs for scalable quantum communication with atomic ensembles*, Nature **423**, 731 (2003).
- [43] C. H. van der Wal, M. D. Eisaman, A. Andre, R. L. Walsworth, et al.: *Atomic Memory for Correlated Photon States*, Science **301**, 196 (2003).
- [44] C. W. Chou, H. de Riedmatten, D. Felinto, S. V. Polyakov, et al.: *Measurement-induced entanglement for excitation stored in remote atomic ensembles*, Nature **438**, 828 (2005).
- [45] K. S. Choi, A. Goban, S. B. Papp, S. J. van Enk, et al.: *Entanglement of spin waves among four quantum memories*, Nature **468**, 412 (2010).
- [46] C. W. Chou, J. Laurat, H. Deng, K. S. Choi, et al.: *Functional Quantum Nodes for Entanglement Distribution over Scalable Quantum Networks*, Science **316**, 1316 (2007).
- [47] Z.-S. Yuan, Y.-A. Chen, B. Zhao, S. Chen, et al.: *Experimental demonstration of a BDCZ quantum repeater node*, Nature **454**, 1098 (2008).
- [48] J. Laurat, H. de Riedmatten, D. Felinto, C.-W. Chou, et al.: *Efficient retrieval of a single excitation stored in an atomic ensemble*, Opt. Express **14**, 6912 (2006).
- [49] J. Simon, H. Tanji, J. K. Thompson, and V. Vuletic: *Interfacing Collective Atomic Excitations and Single Photons*, Phys. Rev. Lett. **98**, 183601 (2007).

- [50] E. Bimbard, R. Boddeda, N. Vitrant, A. Grankin, et al.: *Homodyne Tomography of a Single Photon Retrieved on Demand from a Cavity-Enhanced Cold Atom Memory*, Phys. Rev. Lett. **112**, 033601 (2014).
- [51] A. G. Radnaev, Y. O. Dudin, R. Zhao, H. H. Jen, et al.: *A quantum memory with telecom-wavelength conversion*, Nat Phys **6**, 894 (2010).
- [52] B. Zhao, Y.-A. Chen, X.-H. Bao, T. Strassel, et al.: *A millisecond quantum memory for scalable quantum networks*, Nat Phys **5**, 95 (2009).
- [53] R. Zhao, Y. O. Dudin, S. D. Jenkins, C. J. Campbell, et al.: *Long-lived quantum memory*, Nat Phys **5**, 100 (2009).
- [54] X.-H. Bao, A. Reingruber, P. Dietrich, J. Rui, et al.: *Efficient and long-lived quantum memory with cold atoms inside a ring cavity*, Nat Phys **8**, 517 (2012).
- [55] N. Sangouard, R. Dubessy, and C. Simon: *Quantum Repeaters based on single trapped ions*, Phys. Rev. A **79**, 042340 (2009).
- [56] J. Borregaard, P. Kómár, E. M. Kessler, M. D. Lukin, et al.: *Long-distance entanglement distribution using individual atoms in optical cavities*, Phys. Rev. A **92**, 012307 (2015).
- [57] Y. Han, B. He, K. Heshami, C.-Z. Li, et al.: *Quantum repeaters based on Rydberg-blockade-coupled atomic ensembles*, Phys. Rev. A **81**, 052311 (2010).
- [58] M. J., S. M., D. J., H. A., et al.: *Quantum communication without the necessity of quantum memories*, Nat Photon **6**, 777 (2012).
- [59] S. Muralidharan, J. Kim, N. Lütkenhaus, M. D. Lukin, et al.: *Ultra-fast and Fault-Tolerant Quantum Communication across Long Distances*, Phys. Rev. Lett. **112**, 250501 (2014).
- [60] S. Chen, Y.-A. Chen, T. Strassel, Z.-S. Yuan, et al.: *Deterministic and Storable Single-Photon Source Based on a Quantum Memory*, Phys. Rev. Lett. **97**, 173004 (2006).

- [61] D. N. Matsukevich, T. Chaneliere, S. D. Jenkins, S.-Y. Lan, et al.: *Deterministic Single Photons via Conditional Quantum Evolution*, Phys. Rev. Lett. **97**, 013601 (2006).
- [62] J. Nunn, N. K. Langford, W. S. Kolthammer, T. F. M. Champion, et al.: *Enhancing Multiphoton Rates with Quantum Memories*, Phys. Rev. Lett. **110**, 133601 (2013).
- [63] P. Kok, W. J. Munro, K. Nemoto, T. C. Ralph, et al.: *Linear optical quantum computing with photonic qubits*, Rev. Mod. Phys. **79**, 135 (2007).
- [64] M. Afzelius, , N. Gisin, and H. de Riedmatten: *Quantum memory for photons*, Physics Today **68** (2015).
- [65] Y.-F. Hsiao, P.-J. Tsai, H.-S. Chen, S.-X. Lin, et al.: *EIT-based photonic memory with near-unity storage efficiency*, arXiv (2016).
- [66] Y.-W. Cho, G. T. Campbell, J. L. Everett, J. Bernu, et al.: *Highly efficient optical quantum memory with long coherence time in cold atoms*, Optica **3**, 100 (2016).
- [67] S. Zhou, S. Zhang, C. Liu, J. F. Chen, et al.: *Optimal storage and retrieval of single-photon waveforms*, Opt. Express **20**, 24124 (2012).
- [68] J. Li, Y. Wang, S. Zhang, J. He, et al.: *High efficiency quantum storage of single photons in cold atoms*, arXiv:1706.01404 (2017).
- [69] G. Heinze, C. Hubrich, and T. Halfmann: *Stopped Light and Image Storage by Electromagnetically Induced Transparency up to the Regime of One Minute*, Phys. Rev. Lett. **111**, 033601 (2013).
- [70] M. Zhong, M. P. Hedges, R. L. Ahlefeldt, J. G. Bartholomew, et al.: *Optically addressable nuclear spins in a solid with a six-hour coherence time*, Nature **517**, 177 (2015).

- [71] X. Fernandez-Gonzalvo, G. Corrielli, B. Albrecht, M. Grimaud, et al.: *Quantum frequency conversion of quantum memory compatible photons to telecommunication wavelengths*, Opt. Express **21**, 19473 (2013).
- [72] N. Maring, K. Kutluer, J. Cohen, M. Cristiani, et al.: *Storage of up-converted telecom Photon in a doped crystal*, New Journal of Physics **16**, 113021 (2014).
- [73] C. Simon, H. de Riedmatten, M. Afzelius, N. Sangouard, et al.: *Quantum Repeaters with Photon Pair Sources and Multimode Memories*, Phys. Rev. Lett. **98**, 190503 (2007).
- [74] D. Rieländer, K. Kutluer, P. M. Ledingham, M. Gündoğan, et al.: *Quantum Storage of Heralded Single Photons in a Praseodymium-Doped Crystal*, Phys. Rev. Lett. **112**, 040504 (2014).
- [75] B. Albrecht, P. Farrera, X. Fernandez-Gonzalvo, M. Cristiani, et al.: *A waveguide frequency converter connecting rubidium-based quantum memories to the telecom C-band*, Nat Commun **5**, (2014).
- [76] G. Liu and B. Jacquier, editors: *Spectroscopic Properties of Rare Earths in Optical Materials*, Springer-Verlag, Berlin Heidelberg (2005).
- [77] A. Kaplyankii and R. Macfarlane: *Coherent Transients And Hole-burning Spectroscopy In Rare Earth Ions In Solids; Spectroscopy Of Crystals Containing Rare Earth Ions*, Elsevier Science Publishers, Amsterdam, Netherlands (1987).
- [78] R. Capelletti: *Rare Earths as a Probe of Environment and Electron-phonon Interaction in Optical Materials*, Nova Science Publishers (2009).
- [79] M. Gündoğan: *Solid-state quantum memory for photonic qubits*, Ph.D. thesis, Universitat Politecnica de Catalunya, ICFO (2015).

- [80] S. E. Beavan: *Photon-echo rephasing of spontaneous emission from an ensemble of rare-earth ions*, Ph.D. thesis, The Australian National University (2012).
- [81] Y. Sun, G. M. Wang, R. L. Cone, R. W. Equall, et al.: *Symmetry considerations regarding light propagation and light polarization for coherent interactions with ions in crystals*, Phys. Rev. B **62**, 15443 (2000).
- [82] R. W. Equall, Y. Sun, R. L. Cone, and R. M. Macfarlane: *Ultraslow optical dephasing in $\text{Eu}^{3+}:\text{Y}_2\text{SiO}_5$* , Phys. Rev. Lett. **72**, 2179 (1994).
- [83] S. Poole, D. Payne, and M. Fermann: *Fabrication of low-loss optical bres containing rare-earth ions*, Electronics Letters **21**, 737 (1985).
- [84] L. H. Slooff, A. van Blaaderen, A. Polman, G. A. Hebbink, et al.: *Rare-earth doped polymers for planar optical amplifiers*, Journal of Applied Physics **91**, 3955 (2002).
- [85] T. W. Mossberg: *Time-domain frequency-selective optical data storage*, Opt. Lett. **7**, 77 (1982).
- [86] B. G. Wybourne: *Spectroscopic properties of rare-earths*, John Wiley (1965).
- [87] W. Y. Ching, L. Ouyang, and Y.-N. Xu: *Electronic and optical properties of Y_2SiO_5 and $\text{Y}_2\text{Si}_2\text{O}_7$ with comparisons to $\alpha\text{-SiO}_2$ and Y_2O_3* , Phys. Rev. B **67**, 245108 (2003).
- [88] B. A. Maksimov, Y. A. Kharitonov, V. V. Ilyukhin, and N. V. Belov: *Crystal Structure of the Y-Orthosilicate $\text{Y}_2(\text{SiO}_4)\text{O}$* , Soviet Physics Doklady **13**, 1188 (1969).
- [89] R. Shannon: *Revised effective ionic radii and systematic studies of interatomic distances in halides and chalcogenides*, Acta Crystallographica Section A: Crystal Physics, Diffraction, Theoretical and General Crystallography **32**, 751 (1976).

- [90] C. W. C. Li and R. Moncorge: *Spectroscopic Properties and Fluorescence Dynamics of Er^{3+} and Yb^{3+} In Y_2SiO_5* , IEEE Journal of Quantum Electronics **28**, 1209 (1992).
- [91] K. Holliday, M. Croci, E. Vauthey, and U. P. Wild: *Spectral hole burning and holography in an $Y_2SiO_5:Pr^{3+}$ crystal*, Phys. Rev. B **47**, 14741 (1993).
- [92] B. S. Ham, M. S. Shahriar, M. K. Kim, and P. R. Hemmer: *Frequency-selective time-domain optical data storage by electromagnetically induced transparency in a rare-earth-doped solid*, Opt. Lett. **22**, 1849 (1997).
- [93] R. H. Dicke: *Coherence in Spontaneous Radiation Processes*, Phys. Rev. **93**, 99 (1954).
- [94] H. Kramers: *Théorie générale de la rotation paramagnétique dans les cristaux*, Proc. Amsterdam Acad, **33**, 959 (1930).
- [95] M. Teplov: *Magnetic resonance on Pr^{141} nuclei in $Pr_2(SO_4)_3 \cdot 8H_2O$ single crystal*, Sov Phys JETP **26(5)**, 872 (1968).
- [96] M. Lovrić: *Hyperfine characterisation and enhanced optical to spin storage in rare earth ion doped crystals*, Ph.D. thesis, Technische Universität Dortmund (2011).
- [97] M. Nilsson, L. Rippe, S. Kröll, R. Klieber, et al.: *Hole-burning techniques for isolation and study of individual hyperfine transitions in inhomogeneously broadened solids demonstrated in $Pr^{3+}:Y_2SiO_5$* , Phys. Rev. B **70**, 214116 (2004).
- [98] E. Fraval, M. J. Sellars, and J. J. Longdell: *Method of Extending Hyperfine Coherence Times in $Pr^{3+}:Y_2SiO_5$* , Phys. Rev. Lett. **92**, 077601 (2004).
- [99] J. Huang, J. M. Zhang, A. Lezama, and T. W. Mossberg: *Excess dephasing in photon-echo experiments arising from excitation-induced electronic level shifts*, Phys. Rev. Lett. **63**, 78 (1989).

- [100] Y. Sun, C. W. Thiel, R. L. Cone, R. W. Equall, et al.: *Recent progress in developing new rare earth materials for hole burning and coherent transient applications*, J. Lumin. **98**, 281 (2002).
- [101] W. E. Moerner: *Persistent Spectral Hole-Burning: Science and Applications*, Springer, Berlin (1998).
- [102] E. S. Maniloff, F. R. Graf, H. Gygax, S. B. Altner, et al.: *Power broadening of the spectral hole width in an optically thick sample*, Chemical Physics **193**, 173 (1995).
- [103] O. Guillot-Noël, P. Goldner, F. Beaudoux, Y. Le Du, et al.: *Hyperfine structure and hyperfine coherent properties of praseodymium in single-crystalline $\text{La}_2(\text{WO}_4)_3$ by hole-burning and photon-echo techniques*, Phys. Rev. B **79**, 155119 (2009).
- [104] G. W. Burr, T. L. Harris, W. Babbitt, and C. Jefferson: *Incorporating excitation-induced dephasing into the Maxwell–Bloch numerical modeling of photon*, Journal of Luminescence **107**, 314 (2004), proceedings of the 8th International Meeting on Hole Burning, Single Molecule, and Related Spectroscopies: Science and Applications.
- [105] R. R. Reibel: *High bandwidth optical coherent transient true-time delay*, Ph.D. thesis, Montana State University, Montana State University (2002).
- [106] N. Piovella: *Notes on Semiclassical Theory of the Interaction of Atoms with Radiation* (2010).
- [107] N. Kurnit, I. Abella, and S. Hartmann: *Observation of a photon echo*, Phys. Rev. Lett. **13**, 567 (1964).
- [108] I. D. Abella, N. A. Kurnit, and S. R. Hartmann: *Photon Echoes*, Phys. Rev. **141**, 391 (1966).
- [109] R. G. Brewer and R. L. Shoemaker: *Optical Free Induction Decay*, Phys. Rev. A **6**, 2001 (1972).

- [110] R. W. Boyd: *Nonlinear Optics*, Academic Press, San Diego, CA (1992).
- [111] M. L. Citron, H. R. Gray, C. W. Gabel, and C. R. Stroud: *Experimental study of power broadening in a two-level atom*, Phys. Rev. A **16**, 1507 (1977).
- [112] R. Lauro, T. Chanelière, and J.-L. Le Gouët: *Spectral hole burning for stopping light*, Phys. Rev. A **79**, 053801 (2009).
- [113] K. Kutluer, M. F. Pascual-Winter, J. Dajczgewand, P. M. Ledingham, et al.: *Spectral-hole memory for light at the single-photon level*, Phys. Rev. A **93**, 040302 (2016).
- [114] T. Chanelière, D. N. Matsukevich, S. D. Jenkins, S.-Y. Lan, et al.: *Storage and retrieval of single photons transmitted between remote quantum memories*, Nature **438**, 833 (2005).
- [115] M. D. Eisaman, A. André, F. Massou, M. Fleischhauer, et al.: *Electromagnetically induced transparency with tunable single-photon pulses*, Nature **438**, 837 (2005).
- [116] K. S. Choi, H. Deng, J. Laurat, and H. J. Kimble: *Mapping photonic entanglement into and out of a quantum memory*, Nature **452**, 67 (2008).
- [117] A. V. Turukhin, V. S. Sudarshanam, M. S. Shahriar, J. A. Musser, et al.: *Observation of Ultraslow and Stored Light Pulses in a Solid*, Phys. Rev. Lett. **88**, 023602 (2001).
- [118] J. J. Longdell, E. Fraval, M. J. Sellars, and N. B. Manson: *Stopped Light with Storage Times Greater than One Second Using Electromagnetically Induced Transparency in a Solid*, Phys. Rev. Lett. **95**, 063601 (2005).
- [119] D. Schraft, M. Hain, N. Lorenz, and T. Halfmann: *Stopped Light at High Storage Efficiency in a $\text{Pr}^{3+} : \text{Y}_2\text{SiO}_5$ Crystal*, Phys. Rev. Lett. **116**, 073602 (2016).

- [120] M. Sellars and N. Manson: *Slow light in a solid without using electromagnetically induced transparency*, Springer US (2003).
- [121] J. Hahn and B. S. Ham: *Observations of self-induced ultraslow light in a persistent spectral hole burning medium*, Opt. Express **16**, 16723 (2008).
- [122] B. S. Ham and J. Hahn: *Transmission enhancement of ultraslow light in an atom shelved model of spectral hole burning solids*, Opt. Express **17**, 9369 (2009).
- [123] M. Gündoğan, P. M. Ledingham, K. Kutluer, M. Mazzera, et al.: *Solid State Spin-Wave Quantum Memory for Time-Bin Qubits*, Phys. Rev. Lett. **114**, 230501 (2015).
- [124] P. Jobez, C. Laplane, N. Timoney, N. Gisin, et al.: *Coherent Spin Control at the Quantum Level in an Ensemble-Based Optical Memory*, Phys. Rev. Lett. **114**, 230502 (2015).
- [125] R. Lauro, T. Chanelière, and J. L. Le Gouët: *Slow light using spectral hole burning in a Tm^{3+} -doped yttrium-aluminum-garnet crystal*, Phys. Rev. A **79**, 063844 (2009).
- [126] M. Afzelius, I. Usmani, B. Amari, A. and Lauritzen, A. Walther, et al.: *Demonstration of Atomic Frequency Comb Memory for Light with Spin-Wave Storage*, Phys. Rev. Lett. **104**, 040503 (2010).
- [127] M. Gündoğan, M. Mazzera, P. M. Ledingham, M. Cristiani, et al.: *Coherent storage of temporally multimode light using a spin-wave atomic frequency comb memory*, New Journal of Physics **15**, 045012 (2013).
- [128] H. Zhang, M. Sabooni, L. Rippe, C. Kim, et al.: *Slow light for deep tissue imaging with ultrasound modulation*, Applied Physics Letters **100**, (2012).

- [129] S. E. Beavan, M. P. Hedges, and M. J. Sellars: *Demonstration of Photon-Echo Rephasing of Spontaneous Emission*, Phys. Rev. Lett. **109**, 093603 (2012).
- [130] P. Farrera, G. Heinze, B. Albrecht, M. Ho, et al.: *Generation of single photons with highly tunable wave shape from a cold atomic quantum memory*, arXiv:1601.07142 (2016).
- [131] L. Zhao, X. Guo, C. Liu, Y. Sun, et al.: *Photon pairs with coherence time exceeding 1 micro second*, Optica **1**, 84 (2014).
- [132] A. Stute, B. Casabone, P. Schindler, T. Monz, et al.: *Tunable ion-photon entanglement in an optical cavity*, Nature **485**, 482 (2012).
- [133] B. Albrecht, P. Farrera, X. Fernandez-Gonzalvo, M. Cristiani, et al.: *A waveguide frequency converter connecting rubidium-based quantum memories to the telecom C-band*, Nat Commun **5**, (2014).
- [134] G. Corrielli, A. Seri, M. Mazzera, R. Osellame, et al.: *Integrated Optical Memory Based on Laser-Written Waveguides*, Phys. Rev. Applied **5**, 054013 (2016).
- [135] J. Nunn, K. Reim, K. C. Lee, V. O. Lorenz, et al.: *Multimode Memories in Atomic Ensembles*, Phys. Rev. Lett. **101**, 260502 (2008).
- [136] M. Gündoğan, P. M. Ledingham, A. Almasi, M. Cristiani, et al.: *Quantum Storage of a Photonic Polarization Qubit in a Solid*, Phys. Rev. Lett. **108**, 190504 (2012).
- [137] C. Clausen, F. Bussi eres, M. Afzelius, and N. Gisin: *Quantum Storage of Heralded Polarization Qubits in Birefringent and Anisotropically Absorbing Materials*, Phys. Rev. Lett. **108**, 190503 (2012).
- [138] Z.-Q. Zhou, W.-B. Lin, M. Yang, C.-F. Li, et al.: *Realization of Reliable Solid-State Quantum Memory for Photonic Polarization Qubit*, Phys. Rev. Lett. **108**, 190505 (2012).

- [139] C. Laplane, P. Jobez, J. Etesse, N. Timoney, et al.: *Multiplexed on-demand storage of polarization qubits in a crystal*, New Journal of Physics **18**, 013006 (2016).
- [140] L. Olislager, J. Cussey, A. T. Nguyen, P. Emplit, et al.: *Frequency-bin entangled photons*, Phys. Rev. A **82**, 013804 (2010).
- [141] N. Sinclair, E. Saglamyurek, H. Mallahzadeh, J. A. Slater, et al.: *Spectral Multiplexing for Scalable Quantum Photonics using an Atomic Frequency Comb Quantum Memory and Feed-Forward Control*, Phys. Rev. Lett. **113**, 053603 (2014).
- [142] M. Afzelius, C. Simon, H. de Riedmatten, and N. Gisin: *Multimode quantum memory based on atomic frequency combs*, Phys. Rev. A **79**, 052329 (2009).
- [143] H. de Riedmatten, M. Afzelius, M. U. Staudt, C. Simon, et al.: *A solid-state light-matter interface at the single-photon level*, Nature **456**, 773 (2008).
- [144] T. Chanelière, J. Ruggiero, M. Bonarota, M. Afzelius, et al.: *Efficient light storage in a crystal using an atomic frequency comb*, New Journal of Physics **12**, 023025 (2010).
- [145] A. Amari, A. Walther, M. Sabooni, M. Huang, et al.: *Towards an efficient atomic frequency comb quantum memory*, Journal of Luminescence **130**, 1579 (2010), special Issue based on the Proceedings of the Tenth International Meeting on Hole Burning, Single Molecule, and Related Spectroscopies: Science and Applications (HBSM 2009) - Issue dedicated to Ivan Lorgere and Oliver Guillot-Noel.
- [146] M. Sabooni, F. Beaudoin, A. Walther, N. Lin, et al.: *Storage and Recall of Weak Coherent Optical Pulses with an Efficiency of 25%*, Phys. Rev. Lett. **105**, 060501 (2010).

- [147] M. Sabooni, Q. Li, S. Kröll, S., and L. Rippe: *Efficient Quantum Memory Using a Weakly Absorbing Sample*, Phys. Rev. Lett. **110**, 133604 (2013).
- [148] P. Jobez, I. Usmani, N. Timoney, C. Laplane, et al.: *Cavity-enhanced storage in an optical spin-wave memory*, New Journal of Physics **16**, 083005 (2014).
- [149] L. Viola and S. Lloyd: *Dynamical suppression of decoherence in two-state quantum systems*, Phys. Rev. A **58**, 2733 (1998).
- [150] N. Timoney, B. Lauritzen, I. Usmani, M. Afzelius, et al.: *Atomic frequency comb memory with spin-wave storage in $153\text{ Eu } 3 + :Y 2\text{ SiO } 5$* , Journal of Physics B: Atomic, Molecular and Optical Physics **45**, 124001 (2012).
- [151] H. de Riedmatten, M. Afzelius, M. U. Staudt, C. Simon, et al.: *A solid-state light-matter interface at the single-photon level*, Nature **456**, 773 (2008).
- [152] I. Usmani, M. Afzelius, H. de Riedmatten, and N. Gisin: *Mapping multiple photonic qubits into and out of one solid-state atomic ensemble*, Nat Commun **1**, 12 (2010).
- [153] M. Bonarota, J.-L. L. Gouët, and T. Chanelière: *Highly multimode storage in a crystal*, New Journal of Physics **13**, 013013 (2011).
- [154] P. Jobez, N. Timoney, C. Laplane, J. Etesse, et al.: *Towards highly multimode optical quantum memory for quantum repeaters*, Phys. Rev. A **93**, 032327 (2016).
- [155] A. Seri, A. Lenhard, D. Rieländer, M. Gündoğan, et al.: *Quantum Correlations between Single Telecom Photons and a Multimode On-Demand Solid-State Quantum Memory*, Phys. Rev. X **7**, 021028 (2017).

- [156] C. Clausen, I. Usmani, F. Bussières, N. Sangouard, et al.: *Quantum storage of photonic entanglement in a crystal*, Nature **469**, 508 (2011).
- [157] E. Saglamyurek, N. Sinclair, J. Jin, J. A. Slater, et al.: *Broadband waveguide quantum memory for entangled photons*, Nature **469**, 512 (2011).
- [158] I. Usmani, C. Clausen, F. Bussières, N. Sangouard, et al.: *Heralded quantum entanglement between two crystals*, Nat Photon **6**, 234 (2012).
- [159] Z.-Q. Zhou, Y.-L. Hua, X. Liu, G. Chen, et al.: *Quantum Storage of Three-Dimensional Orbital-Angular-Momentum Entanglement in a Crystal*, Phys. Rev. Lett. **115**, 070502 (2015).
- [160] F. Bussi eres, C. Clausen, A. Tiranov, B. Korzh, et al.: *Quantum teleportation from a telecom-wavelength photon to a solid-state quantum memory*, Nat Photon **8**, 775 (2014).
- [161] H. de Riedmatten and M. Afzelius: *Quantum Light Storage in Solid State Atomic Ensembles*, 241–273, Springer International Publishing, Cham (2015).
- [162] B. Albrecht: *Quantum control of single spin excitations in cold atomic quantum memories*, Ph.D. thesis, Universitat Polit cnica de Catalunya, ICFO (2015).
- [163] M. Bonarota, J. Ruggiero, J.-L. Le Gou t, and T. Chaneli re: *Efficiency optimization for atomic frequency comb storage*, Phys. Rev. A **81**, 033803 (2010).
- [164] B. Lauritzen, S. R. Hastings-Simon, H. de Riedmatten, M. Afzelius, et al.: *State preparation by optical pumping in erbium-doped solids using stimulated emission and spin mixing*, Phys. Rev. A **78**, 043402 (2008).

- [165] J. Dajczgewand, J.-L. Le Gouët, A. Louchet-Chauvet, and T. Chanelière: *Quantum memory for light: large efficiency at telecom wavelength*, arXiv:1312.0763 .
- [166] M. Rančić, M. P. Hedges, R. L. Ahlefeldt, and M. J. Sellars: *Coherence time of over a second in a telecom-compatible quantum memory storage material*, arXiv:1611.04315 (2016).
- [167] B. Lauritzen, J. Minar, H. de Riedmatten, M. Afzelius, et al.: *Telecommunication-Wavelength Solid-State Memory at the Single Photon Level*, Phys. Rev. Lett. **104**, 080502 (2010).
- [168] B. Lauritzen, J. Minar, H. de Riedmatten, M. Afzelius, et al.: *Approaches for a quantum memory at telecommunication wavelengths*, Phys. Rev. A **83**, 012318 (2011).
- [169] M. Afzelius and C. Simon: *Impedance-matched cavity quantum memory*, Phys. Rev. A **82**, 022310 (2010).
- [170] S. A. Moiseev, S. N. Andrianov, and F. F. Gubaidullin: *Efficient multimode quantum memory based on photon echo in an optimal QED cavity*, Phys. Rev. A **82**, 022311 (2010).
- [171] P. Sekatski, N. Sangouard, N. Gisin, H. de Riedmatten, et al.: *Photon-pair source with controllable delay based on shaped inhomogeneous broadening of rare-earth-metal-doped solids*, Phys. Rev. A **83**, 053840 (2011).
- [172] K. Kutluer, M. Mazzera, and H. de Riedmatten: *Solid-State Source of Nonclassical Photon Pairs with Embedded Multimode Quantum Memory*, Phys. Rev. Lett. **118**, 210502 (2017).
- [173] J. Nunn: *A Solid Footing for a Quantum Repeater*, Physics **10** (2017).
- [174] C. Laplane, P. Jobez, J. Etesse, N. Gisin, et al.: *Multimode and Long-Lived Quantum Correlations Between Photons and Spins in a Crystal*, Phys. Rev. Lett. **118**, 210501 (2017).

- [175] Z.-Q. Zhou, S. F. Huelga, C.-F. Li, and G.-C. Guo: *Experimental Detection of Quantum Coherent Evolution through the Violation of Leggett-Garg-Type Inequalities*, Phys. Rev. Lett. **115**, 113002 (2015).
- [176] J. Fekete, D. Rielander, M. Cristiani, and H. de Riedmatten: *Ultranarrow-Band Photon-Pair Source Compatible with Solid State Quantum Memories and Telecommunication Networks*, Phys. Rev. Lett. **110**, 220502 (2013).
- [177] S.-J. Yang, X.-J. Wang, X.-H. Bao, and J.-W. Pan: *An efficient quantum light-matter interface with sub-second lifetime*, Nat. Photon. **10**, 381 (2016).
- [178] L. K.C., S. B.J., S. M.R., M. P., et al.: *Macroscopic non-classical states and terahertz quantum processing in room-temperature diamond*, Nat Photon **6**, 41 (2012).
- [179] R. Riedinger, S. Hong, R. A. Norte, J. A. Slater, et al.: *Non-classical correlations between single photons and phonons from a mechanical oscillator*, Nature **530**, 313 (2016), letter.
- [180] P. M. Ledingham, W. R. Naylor, J. J. Longdell, S. E. Beavan, et al.: *Nonclassical photon streams using rephased amplified spontaneous emission*, Phys. Rev. A **81**, 012301 (2010).
- [181] E. A. Goldschmidt, S. E. Beavan, S. V. Polyakov, A. L. Migdall, et al.: *Storage and retrieval of collective excitations on a long-lived spin transition in a rare-earth ion-doped crystal*, Opt. Express **21**, 10087 (2013).
- [182] P. M. Ledingham, W. R. Naylor, and J. J. Longdell: *Experimental Realization of Light with Time-Separated Correlations by Rephasing Amplified Spontaneous Emission*, Phys. Rev. Lett. **109**, 093602 (2012).
- [183] K. R. Ferguson, S. E. Beavan, J. J. Longdell, and M. J. Sellars: *Generation of Light with Multimode Time-Delayed Entanglement Using*

- Storage in a Solid-State Spin-Wave Quantum Memory*, Phys. Rev. Lett. **117**, 020501 (2016).
- [184] H. de Riedmatten, J. Laurat, C. W. Chou, E. W. Schomburg, et al.: *Direct Measurement of Decoherence for Entanglement between a Photon and Stored Atomic Excitation*, Phys. Rev. Lett. **97**, 113603 (2006).
- [185] B. Albrecht, P. Farrera, G. Heinze, M. Cristiani, et al.: *Controlled Rephasing of Single Collective Spin Excitations in a Cold Atomic Quantum Memory*, Phys. Rev. Lett. **115**, 160501 (2015).
- [186] J. D. Franson: *Bell inequality for position and time*, Phys. Rev. Lett. **62**, 2205 (1989).
- [187] P. Jobez: *Stockage multimode au niveau quantique pendant une milliseconde*, Ph.D. thesis, Universite de Geneve (2015).
- [188] P. Farrera, N. Maring, B. Albrecht, G. Heinze, et al.: *Nonclassical correlations between a C-band telecom photon and a stored spin-wave*, Optica **3**, 1019 (2016).
- [189] E. Saglamyurek, N. Sinclair, J. Jin, J. A. Slater, et al.: *Conditional Detection of Pure Quantum States of Light after Storage in a Tm-Doped Waveguide*, Phys. Rev. Lett. **108**, 083602 (2012).
- [190] E. Miyazono, I. Craiciu, A. Arbabi, T. Zhong, et al.: *Coupling erbium dopants in yttrium orthosilicate to silicon photonic resonators and waveguides*, Opt. Express **25**, 2863 (2017).
- [191] T. Zhong, J. M. Kindem, E. Miyazono, and A. Faraon: *Nanophotonic coherent light-matter interfaces based on rare-earth-doped crystals*, Nat Commun **6**, (2015).
- [192] T. Zhong, J. M. Kindem, J. Rochman, and A. Faraon: *Interfacing broadband photonic qubits to on-chip cavity-protected rare-earth ensembles* **8**, 14107 EP (2017), article.

- [193] E. Saglamyurek, T. Lutz, L. Veissier, M. P. Hedges, et al.: *Efficient and long-lived Zeeman-sublevel atomic population storage in an erbium-doped glass fiber*, Phys. Rev. B **92**, 241111 (2015).
- [194] J. Jin, E. Saglamyurek, M. I. G. Puigibert, V. Verma, et al.: *Telecom-Wavelength Atomic Quantum Memory in Optical Fiber for Heralded Polarization Qubits*, Phys. Rev. Lett. **115**, 140501 (2015).
- [195] E. Eichhammer, T. Utikal, S. Götzinger, and V. Sandoghdar: *Spectroscopic detection of single Pr ions on the $3H_4\ 1D_2$ transition*, New Journal of Physics **17**, 083018 (2015).
- [196] K. Xia, R. Kolesov, Y. Wang, P. Siyushev, et al.: *Optical and spin properties of a single praseodymium ion in a crystal*, arXiv **arXiv:1706.08736** (2017).
- [197] T. Utikal, E. Eichhammer, L. Petersen, A. Renn, et al.: *Spectroscopic detection and state preparation of a single praseodymium ion in a crystal*, Nat Comm **5** (2014).
- [198] C. O'Brien, T. Zhong, A. Faraon, and C. Simon: *Nondestructive photon detection using a single rare-earth ion coupled to a photonic cavity*, Phys. Rev. A **94**, 043807 (2016).

“Everything that has a beginning has an end.”

to my banne..